UNIVERSITÀ DEGLI STUDI
DI TRENTO

DEPARTMENT OF INFORMATION ENGINEERING AND COMPUTER SCIENCE
ICT International Doctoral School

Development of 3D Silicon radiation detectors for neutrons and high energy charged particles

Roberto Mendicino

Advisor

Prof. Gian-Franco Dalla Betta

Università degli Studi di Trento

March 2017

To My Brother

ABSTRACT

In the past few years, several interesting developments in microstructured solid-state thermal neutron detectors have been pursued. These devices feature high aspect-ratio cavities, filled with neutron converter materials, so as to improve the neutron detection efficiency with respect to coated planar sensors. In the framework of the INFN HYDE (HYbrid Detectors for neutrons) project, we have designed new microstructured sensors aimed at thermal and fast neutron detection. Owing to the different cross section, neutron imaging is complementary to X-ray imaging allowing for a high contrast in soft materials. To this purpose, the possibility to have pixelated neutron detectors compatible with existing read-out chips (e.g., those from the Medipix/Timepix family) is an important goal that was achieved in this thesis. In this thesis the entire workflow will be described in detail, covering the design, simulations, fabrication and characterization of 3D neutron detectors for imaging produced at FBK. As a related topic, new 3D sensors for the "Phase-2" upgrades at High Luminosity LHC have been developed, and some aspects relevant to the device simulation and characterization are also reported in this thesis.

Keywords

[Solid state neutron detector, TCAD simulations, Device characterization]

List of presentations at conferences and workshops

[1] "Investigation of the electrical Characteristics of double-sided silicon 3D sensors after irradiation with different particles", 8th Workshop on Advanced Silicon Radiation Detectors, 3D and P-type Technologies (TREDI), Trento, Italy, 18th-20th February 2013 [Oral Presentation].

[2] "Novel 3D silicon sensors for neutron detection", 15th International Workshop on Radiation Imaging Detectors (iWoRiD13), Paris, France 23th-27th June 2013 [Oral Presentation].

[3] "Characterization of double-sided 3D sensors after proton and neutron irradiation", 9th Workshop on Advanced Silicon Radiation Detectors, 3D and P-type Technologies (TREDI), Genova, Italy, February 2014 [Oral Presentation].

[4] "Characterization of 3D and planar Si diodes with different neutron converter materials", International Conference on Radiation Effects on Semiconductor Materials and Devices (RESMDD14), Florence, Italy 8th-10th October 2014 [Oral Presentation].

[5] "Micromachined silicon radiation sensors – part 1: design and experimental characterization", AISEM, Trento, Italy 3th-5th February 2015 [Oral Presentation].

[6] "Design and TCAD simulation of a new generation of 3D Sensors for HL-LHC within the INFN (ATLAS-CMS) R&D program in collaboration with FBK", 10th orkshop on Advanced Silicon Radiation Detectors, 3D and P-type Technologies (TREDI), Trento, Italy 17th-19th February 2015 [Oral Presentation].

[7] "Semiconductor neutron detectors", 24th International Workshop

on Vertex Detectors, Sante Fe, NM, USA, 1st-5th June 2015 [Oral Presentation as Invited Speaker].

[8] "A New Geometry for Hybrid Detectors of Neutrons Based on Microstructured Silicon Sensors filled with $^{10}B_4C$", IEEE Nuclear Science Symposium and Medical Imaging Conference (NSS-MIC'15), October 31 - November 7, 2015, San Diego, Ca, USA [Poster Presentation]

[9] "Initial results from new 3D neutron detectors", 18th International Workshop on Radiation Imaging Detectors (iWoRiD16), Barcelona, Spain 3th-7th July 2016 [Oral Presentation].

[10] "Web-Shaped Microstructured Silicon hybrid detectors of thermal neutrons", IEEE Nuclear Science Symposium and Medical Imaging Conference (NSS-MIC'16), October 29 - November 6, 2016, Strasbourg, France [Poster Presentation]

[11] "Development of Thin, Narrow-Pitch 3D Pixel Sensors for HL-LHC", 12th Workshop on Advanced Silicon Radiation Detectors, 3D and P-type Technologies (TREDI), Trento, Italy, 20th-22th February 2017 [Oral Presentation].

Scientific Publication

[1] M. Povoli, A. Bagolini, M. Boscardin, G.-F. Dalla Betta, G. Giacomini, F. Mattedi, **R. Mendicino**, N. Zorzi, "Design and testing of an innovative slim-edge termination for silicon radiation detectors", Journal of Instrumentation, JINST 8, C11022, 2013.

[2] M. Dalla Palma, G.-F. Dalla Betta, G. Collazuol, T. Marchi, M. Povoli, **R. Mendicino**, M. Boscardin, S. Ronchin, N. Zorzi, G. Giacomini, A. Quaranta, S. Carturan, M. Cinausero, F. Gramegna, "Hybrid Detectors for Neutrons Combining Phenyl- Polysiloxanes with 3D Silicon Detectors", Proceedings of of the International Conference on Advancements in Nuclear Instrumentation Measurement Methods and their Applications (ANIMMA 2013), Marseille (France), June 23-27 2013, paper 1321.

[3] G.-F. Dalla Betta, M. Boscardin, S. Carturan, M. Cinausero, G. Collazuol, M. Dalla Palma, G. Giacomini, F. Gramegna, C. Granja, T. Marchi, **R. Mendicino**, E. Perillo, M. Povoli, A. Quaranta, S. Ronchin, T. Slavíček, M. Štefánik, J. Vacík, N. Zorzi, "Hybrid Detectors of Neutrons Based on 3D Silicon Sensors with Polysiloxane Converter", Conference Record of the IEEE Workshop on Room Temperature Semiconductor Detectors, Seoul (Corea del Sud), 27th October - 2nd November 2013, paper R05-39.

[4] G.-F. Dalla-Betta, M. Boscardin, G. Giacomini, M. Hoeferkamp, F. Mattedi, S. Mattiazzo, H. McDuff, **R. Mendicino**, M. Povoli, S. Seidel, N. Zorzi, "Characterization of New FBK Double-Sided 3D Sensors with Improved Breakdown Voltage", (Invited paper), Conference Record of the IEEE Nuclear Science Symposium and Medical Imaging Conference, Seoul (Corea del Sud), 27th October - 2nd November 2013, paper N41-1

[5] **R. Mendicino**, M. Boscardin, S. Carturan, M. Cinausero, G. Collazuol, G.-F. Dalla Betta, M. Dalla Palma, F. Gramegna, T. Marchi, E. Perillo, M. Povoli, A. Quaranta, S. Ronchin, N. Zorzi, "Novel 3D silicon sensors for neutron detection", Journal of Instrumentation, JINST 9, C05001, 2014.

[6] M. Bubna, D. Bortoletto, E. Alagoz, A. Krzywda, K. Arndt, I. Shipsey, G. Bolla, N. Hinton, A. Kok, T.-E. Hansen, A. Summanwar, J. M. Brom, M. Boscardin, J. Chramowicz, J. Cumalat, G.-F. Dalla Betta, M. Dinardo, A. Godshalk, M. Jones, M. D. Krohn, A. Kumar, C. M. Lei, **R. Mendicino**, L. Moroni, L. Perera, M. Povoli, A. Prosser, R. Rivera, A. Solano, M. M. Obertino, S. Kwan, L. Uplegger, L. Viganig, S. Wagnerf, "Testbeam and laboratory characterization of CMS 3D pixel sensors", Journal of Instrumentation, JINST 9, C07019, 2014.

[7] A. Krzywda, E. Alagoz, M. Bubna, M. Obertino, A. Solano, K. Arndt, L. Uplegger, G.-F. Dalla Betta, M. Boscardin, J. Ngadiuba, R. Rivera, D. Menasce, L. Moroni, S. Terzo, D. Bortoletto, A. Prosser, J. Adreson, S. Kwan, I. Osipenkov, G. Bolla, C. M. Lei, I. Shipsey, P. Tan, N. Tran, J. Chramowicz, J. Cumalat, L. Perera, M. Povoli, **R. Mendicino**, A. Vilela Pereira, R. Brosius, A. Kumar, S. Wagner, F. Jensen, S. Bose, S. Tentindo, "Pre- and post-irradiation performance of FBK 3D silicon pixel detectors for CMS", Nucl. Instr. and Meth. A, Vol. 763, pp. 404-411, 2014.

[8] G.-F. Dalla Betta, C. Betancourt, M. Boscardin, G. Giacomini, K. Jakobs, S. Kühn, B. Lecini, **R. Mendicino**, R. Mori, U. Parzefall, M. Povoli, M. Thomas, N. Zorzi, "Radiation hardness tests of double-sided 3D strip sensors with passing-through columns", Nucl. Instr. and Meth. A, vol. 765, pp. 155-160, 2014.

[9] G. F. Dalla Betta, G. Batignani, M. A. Benkechkache, S. Bettarini, G. Casarosa, D. Comotti, L. Fabris, F. Forti, M. Grassi, S. Latreche-Lassoued, L. Lodola, P. Malcovati, M. Manghisoni, **R. Mendicino**, F. Morsani, A. Paladino, L.Pancheri, E.Paoloni, L. Ratti, V. Re, G. Rizzo, G. Traversi, C. Vacchi, G. Verzellesi, H. Xu, "Design and TCAD Simulations of Planar Active-Edge Pixel Sensors for Future XFEL Applications", IEEE Nuclear Science Symposium and Medical Imaging Conference (NSS - MIC'14), Conference Record, Seattle (USA) 9 -15 Nov. 2014, paper N8-07.

[10] L. Ratti, D. Comotti, L. Fabris, M. Grassi, L. Lodola, P. Malcovati, M. Manghisoni, V. Re, G. Traversi, C. Vacchi, G. Batignani, S. Bettarini, G. Casarosa, F. Forti, F. Morsani, A. Paladino, E. Paoloni, G. Rizzo, M.A. Benckechkache, G. F. Dalla Betta, **R. Mendicino**, L. Pancheri, G. Verzellesi, H. Xu, "PixFEL: enabling technologies, building blocks and architectures for advanced X-ray pixel cameras at the next generation FELs", IEEE Nuclear Science Symposium and Medical Imaging Conference (NSS - MIC'14), Conference Record, Seattle (USA) 9 -15 Nov. 2014, paper N31-03.

[11] D. Comotti, L. Fabris, M. Grassi, L. Lodola, P. Malcovati, M. Manghisoni, L. Ratti, V. Re, G. Traversi, C. Vacchi, G. Batignani, S. Bettarini, G. Casarosa, F. Forti, F. Morsani, A. Paladino, E. Paoloni, G. Rizzo, M.A. Benckechkache, G. F. Dalla Betta, **R. Mendicino**, L. Pancheri, G. Verzellesi, H. Xu, "Low-Noise Readout Channel with a Novel Dynamic Signal Compression for Future X-FEL Applications", IEEE Nuclear Science Symposium and Medical Imaging Conference (NSS - MIC'14), Conference Record, Seattle (USA) 9 -15 Nov. 2014, paper N18-2.

[12] G. Rizzo, D. Comotti, L. Fabris, M. Grassi, L. Lodola, P. Malcovati, M.

Manghisoni, L. Ratti, V. Re, G. Traversi, C. Vacchi, G. Batignani, S. Bettarini, G. Casarosa, F. Forti, F. Morsani, A. Paladino, E. Paoloni, G-F Dalla Betta, L. Pancheri, G. Verzellesi, H. Xu, **R. Mendicino**, MA. Benkechkache, "The PixFEL project: development of advanced X-ray pixel detectors for application at future FEL facilities", Journal of Instrumentation, JINST 10, C02024, 2015.

[13] A. Bagolini, M. Boscardin, P. Conci, M. Crivellari, G. Giacomini, F. Mattedi, C. Piemonte, S. Ronchin, N. Zorzi, MA. Benkechkache, GF Dalla Betta, **R. Mendicino**, L. Pancheri, M. Povoli, DMS Sultan, "Micromachined Silicon Radiation Sensors–Part 1: Design And Experimental Characterization", Proceedings of the 2015 XXVIII AISEM Annual Conference, Trento (Italy), 3-5 February 2015.

[14] A. Bagolini, M. Boscardin, P. Conci, M. Crivellari, G. Giacomini, F. Mattedi, C. Piemonte, S. Ronchin, N. Zorzi, MA. Benkechkache, GF Dalla Betta, **R. Mendicino**, L. Pancheri, M. Povoli, DMS Sultan, "Micromachined Silicon Radiation Sensors–Part 2: Fabrication technologies", Proceedings of the 2015 XXVIII AISEM Annual Conference, Trento (Italy), 3-5 February 2015.

[15] L. Ratti, D. Comotti, L. Fabris, M. Grassi, L. Lodola, P. Malcovati, M. Manghisoni, V. Re, G Traversi, C. Vacchi, S. Bettarini, G. Casarosa, F. Forti, F. Morsani, A. Paladino, E. Paoloni, G. Rizzo, MA. Benkechkache, G-F Dalla Betta, **R. Mendicino**, L. Pancheri, G. Verzellesi, H. Xu, "PixFEL: developing a fine pitch, fast 2D X-ray imager for the next generation X-FELs", Nucl. Instr. and Meth. A, vol. 796, pp. 2-7, 2015.

[16] **R. Mendicino**, M. Boscardin, S. Carturan, G.-F. Dalla Betta, M. Dalla Palma, G. Maggioni, A. Quaranta, S. Ronchin, "Characteri-

zation of 3D and planar Si diodes with different neutron converter materials" Nucl. Instr. and Meth. A , Volume 796, Pages 23–28, 2015.

[17] C. Da Già, M. Borri, G. Dalla Betta, I. Haughton, J. Hasi, C. Kenney, M. Povoli, **R. Mendicino**, "3D silicon sensors with variable electrode depth for radiation hard high resolution particle tracking", Journal of Instrumentation, JINST 10, C04020, 2015.

[18] G. Giacomini, L. Bosisio, G-F Dalla Betta, **R. Mendicino**, L. Ratti, "Integrated Source Follower for the Read-Out of Silicon Sensor Arrays", IEEE Transactions on Nuclear Science, Vol. 62(5), pp. 2187-2193, 2015.

[19] L. Pancheri, D. Comotti, L. Fabris, M. Grassi, L. Lodola, P. Malcovati, M. Manghisoni, L. Ratti, V. Re, G. Traversi, C. Vacchi, S. Bettarini, G. Casarosa, F. Forti, F. Morsani, A. Paladino, E. Paoloni, G. Rizzo, M.A. Benkechkache, G. F. Dalla Betta, **R. Mendicino**, L. Pancheri, G. Verzellesi, H. Xu, "PixFEL project: hybrid High Dynamic Range X-ray image sensor for application at future FEL facilities", Proceedings of 2015 International Image Sensor Workshop (IISW 2015), Vaals (Holland), 14-18 June 2015, pp. 276-279

[20] **R. Mendicino** , A. Bagolini, M. Boscardin, G.-F. Dalla Betta, M. Dalla Palma, A. Quaranta, "Semiconductor neutron detectors" (Invited paper), Proceedings of Science - 24th Workshop on Vertex Detectors (Vertex 2015), Paper 027, 2015.

[21] D.M.S. Sultan, **R. Mendicino**, M. Boscardin, S. Ronchin, N. Zorzi, G.-F. Dalla Betta, "Characterization of the first double-sided 3D radiation sensors fabricated at FBK on 6-inch silicon wafers" Journal of Instrumentation, JINST 10, C12029, 2015

[22] G. F. Dalla Betta, G. Batignani, M.A. Benkechkache, S. Bettarini, G. Casarosa, D. Comotti, L. Fabris, F. Forti, M. Grassi, S. Latreche, L. Lodola, P. Malcovati, M. Manghisoni, **R. Mendicino**, F. Morsani, A. Paladino, L. Pancheri, E. Paoloni, L. Ratti, V. Re, G. Rizzo, G. Traversi, C. Vacchi, G. Verzellesi, H. Xu, "Design and TCAD simulation of planar p-on-n active-edge pixel sensors for the next generation of FELs", in press on Nucl. Instr. and Meth. A, doi:10.1016/j.nima.2015.08.027

[23] G-F Dalla Betta, M. Boscardin, G. Darbo, **R. Mendicino**, M. Meschini, A. Messineo, S. Ronchin, DMS Sultan, N. Zorzi,"Development of a new generation of 3D pixel sensors for HL-LHC", in press on Nucl. Instr. and Meth. A, doi:10.1016/j.nima.2015.08.032

[24] G-F Dalla Betta, M. Boscardin, M. Bomben, M. Brianzi, G. Calderini, G. Darbo, R. Dell'Orso, A. Gaudiello, G. Giacomini, **R. Mendicino**, M. Meschini, A. Messineo, S. Ronchin, DMS Sultan, N. Zorzi, "The INFN–FBK "Phase-2" R&D program", in presso on Nucl. Instr. and Meth. A, doi:10.1016/j.nima.2015.08.74

[25] L. Lodola, G. Batignani, MA Benkechkache, S. Bettarini, G. Casarosa, D. Comotti, GF Dalla Betta, L. Fabris, F. Forti, M. Grassi, S. Latreche, P. Malcovati, M. Manghisoni, **R. Mendicino**, F. Morsani, A. Paladino, L. Pancheri, E. Paoloni, L. Ratti, V. Re, G. Rizzo, G. Traversi, C. Vacchi, G. Verzellesi, H. Xu, "In-pixel conversion with a 10bit SAR ADC for next generation X-ray FELs", in press on Nucl. Instr. and Meth. A, doi:10.1016/j.nima.2015.10.042

[26] G.-F. Dalla Betta, M. Boscardin, M. Bomben, M. Brianzi, G. Calderini, G. Darbo, R. Dell'Orso, A. Gaudiello, G. Giacomini, **R. Mendicino**, M. Meschini, A. Messineo, S. Ronchin, D.M.S. Sultan, N. Zorzi, "The

INFN–FBK “Phase-2” R& D program” Nuclear Instruments and Methods in Physics Research A 824 (2016) 388–391,

[27] G.-F. Dalla Betta, M. Boscardin, G. Darbo,**R. Mendicino**,M. Meschini ,A. Messineo ,S. Ronchin ,D.M.S. Sultan ,N. Zorzi, ”Development of a new generation of 3D pixel sensors for HL-LHC” Nuclear Instruments and Methods in Physics Research A 824 (2016) 386-387, http://dx.doi.org/10.1016/j.nima.2015.08.032

[28] G.-F.DallaBetta, G.Batignani, M.A.Benkechkache, S.Bettarini, G.Casarosa, D. Comotti, L.Fabris, F.Forti, M.Grassi, S.Latreche, L.Lodola, P.Malcovati, M. Manghisoni, **R. Mendicino**, F.Morsani, A.Paladino, L.Pancheri, E.Paoloni, L. Ratti, V.Reg, G.Rizzo, G.Traversi, C.Vacchi, G.Verzellesi, H.Xua, ”Design and TCAD simulation of planar p-on-n active-edge pixel sensors for the next generation of FELs” Nuclear Instruments and Methods in Physics Research A 824(2016) 384–385, http://dx.doi.org/10.1016/j.nima.2015.08.027

[29] L. Lodola, G. Batignani, M.A. Benkechkache, S. Bettarini, G. Casarosa, D. Comotti, G.F. Dalla Betta, L. Fabris, F. Forti, M. Grassi, S. Latreche, P. Malcovati, M. Manghisoni, **R. Mendicino**, F. Morsani, A. Paladino, L. Pancheri, E. Paoloni, L. Ratti, V. Re, G. Rizzo, G. Traversi, C. Vacchi, G. Verzellesi, H. Xu, ”In-pixel conversion with a 10 bit SAR ADC for next generation X-ray FELs”,Nuclear Instruments and Methods in Physics Research A 824(2016) 313–315,doi:10.1016/j.nima.2015.10.042

[30] G. Rizzo, G. Batignani, M.A. Benkechkache, S. Bettarini, G. Casarosa, D. Comotti, G.-F. Dalla Betta, L. Fabris, F. Forti, M. Grassi, L. Lodola, P. Malcovati, M. Manghisoni, **R. Mendicino**, F. Morsani, A. Paladino, L. Pancheri, E. Paoloni, L. Ratti, V. Re, G. Traversi, C.

Vacchi, G. Verzellesi, H. Xu, "The PixFEL project: Progress towards a fine pitch X-ray imaging camera for next generation FEL facilities" Nuclear Instruments and Methods in Physics Research A 824(2016) 131-134, doi:10.1016/j.nima.2016.01.027

[31] G. F. Dalla Betta,N. Ayllon, M. Boscardin, M.Hoeferkamp, S. Mattiazzo, H. McDuff,**R. Mendicino**, M. Povoli, S.Seidel, D.M.S. Sultan "Investigation of leakage current and breakdown voltage in irradiated double-sided 3D silicon sensors" Journal of Instrumentation, 11(09), P09006.

[32] D.M.S. Sultana, G.-F. Dalla Betta, **R. Mendicino**, M. Boscardin, S. Ronchin,N. Zorzi " First production of new thin 3D sensors for HL-LHC at FBK" Journal of Instrumentation, 12(01), C01022.

[33] **R. Mendicino**, A. Bagolini, M. Boscardin, G.-F. Dalla Betta,N. Laidani "Initial results from new 3D neutron detectors" Journal of Instrumentation, 11(11), C11002.

[34] G. -F. Dalla Betta, M. Boscardin, M. Bomben, M. Brianzi, G. Calderini, G. Darbo, R. Dell'Orso, A. Gaudiello, G. Giacomini, **R. Mendicino**, M.Meschini, A. Messineo, S.Ronchin, D.M.S. Sultan, N. Zorzi "The INFN–FBK "Phase-2" R&D program". Nuclear Instruments and Methods in Physics Research Section A: Accelerators, Spectrometers, Detectors and Associated Equipment, 824, 388-391.

[35] G. -F. Dalla Betta, M. Boscardin, G. Darbo,**R. Mendicino**, M. Meschini, M.Messineo, S. Ronchin, D.M.S Sultan, Zorzi, N. "Development of a new generation of 3D pixel sensors for HL-LHC" Nuclear Instruments and Methods in Physics Research Section A: Accelerators, Spectrometers, Detectors and Associated Equipment, 824, 386-387.

[36] F. Moscatelli, D. Passeri, A. Morozzi, **R. Mendicino**, G. -F. Dalla Betta, G.M. Bilei "Combined Bulk and Surface Radiation Damage Effects at Very High Fluences in Silicon Detectors: Measurements and TCAD Simulations" IEEE Transactions on Nuclear Science, 63(5), 2716-2723.

INDEX

Contents

List of Tables

List of Figures

CHAPTER 1

Solid state radiation detector

1.1 Interaction of Radiation with Matter

A physical quantity can be directly detected only if it strictly interact with the sensing part of a sensor. This chapter covers the basic principles underlying the interaction between radiation and matter, in order to better understand how a radiation detector works.

The interaction of radiation with matter strongly depends on the nature of the radiation source, that encompasses both charged or uncharged radiation. Heavy charged particles and fast electrons are charged particles, whereas electromagnetic radiation and neutrons belong to the group of uncharged radiation. Depending on the radiation type and on the applications, different detectors in terms of materials, geometries and dimensions are needed.

1.1.1 Heavy Charged Particles

The interactions of heavy charged particles (such as ions and alpha particles) with matter are affected by the Coulomb forces between particles and electrons. The maximum energy transmitted by a particle to a single electron in an interaction is 1/500 of the its initial energy. The electron moves to an excitation state if it remains within the higher-lying shell of the atom, otherwise it moves to an ionization state. Macroscopically, the Heavy Charged Particles are studied by considering the specific energy loss rate using the Bethe formula [36].

$$-\frac{dE}{dx} = \frac{4\pi e^4 z^2}{m_0 v} NZ \left[ln\frac{2m_0 v^2}{I} - ln\left(1 - \frac{v^2}{c^2}\right) - \frac{v^2}{c^2} \right] \tag{1.1}$$

where v and z(in multiples of the electron charge e) are the velocity and the atomic charge of the primary particle and N and Z are the density ($atoms/cm^3$) and the atomic number of the media. m_0 is the electron rest mass and e is its charge. I is an experimentally obtained number related the ionization/excitation potential of the material. The most relevant pieces of information coming from this formula are the dependence of the energy loss on the absorption material and the importance of the particle velocity in the media. The Bethe Bloch formula works well if the ion energy is high enough and does not allow to carry any free electron with it. At lower energies the combination of particle-electron reduces the effective charge reducing, consequently, the energy loss rate. Different corrections to the formula have been developed to describe this effect. As consequence of the Bhete corrections the relation between the specific energy loss and the particle track is described by the Bragg curve. As example, figure 1.1 shows the SRIM simulation [4] of the energy released by an alpha particle of 5 MeV in a silicon target.

Most of the energy is lost when the particle velocity is reduced to very low values. The absorption phenomens happen through a statistical or

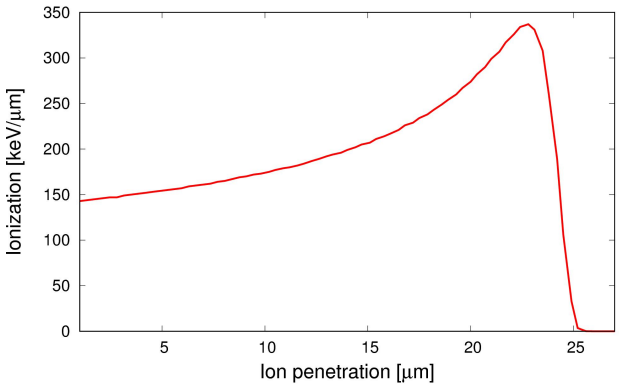

Figure 1.1: Bragg peak for a 5 MeV alpha particle in silicon [4]

stochastic process related to the random interaction between heavy ion particles and electrons. If a mono-energetic beam hits a thin target, the energy of the particles that pass through it will be in a wide range depending of the penetration distance. The time necessary to stop the particle, with range R, mass m_A and average velocity $\langle v \rangle = Kv$ (where v is evaluated at the initial energy) can be calculated using the formula 1.2:

$$T = \frac{R}{\langle v \rangle} = \frac{R}{Kc}\sqrt{\frac{m_A c^2}{2E}} \tag{1.2}$$

Considering real cases, it is on the order of few ps in solid state matter and few ns in gasses. An important difference is found for heavy particles generated as a result of a nuclear fission. In this case, the specific energy loss decreases when the energy of the particle decrease. This effect does not affect lighter particles such as protons or alpha particles. Another important effect to be considered are the so called ”secondary electrons”. If the ion particle transmits to an electron a sufficiently high energy, the electron itself will be a charged particle moving in the media. Because the maximum energy transmitted to an electron is considerably lower than the energy of the particle, the energy spectrum of these electrons will be

significantly shifted at lower values compared to the ion energy.

1.1.2 Fast Electrons

The mechanism of interaction between fast electrons and matter bears many similarities to heavy charged particles, the main difference being the much smaller mass. In this case the mass of the particle is equal to the mass of the electrons in the orbitals. As a result, the trajectory of a fast electron may be suddenly changed and, as result, the trace of particle path will look like a zigzag. The specific energy loss follows rules described by a modified Bethe Bloch formulations. In addition, two new effects called bremsstrahlung and back scattering must be taken in account in the new particle trajectory. The first one is an abrupt change of direction by the particle that can be considered as a particle acceleration, making the particle radiate an electromagnetic wave. The bremsstrahlung effect is negligible for low energy electrons but it can become predominant for high energy ones. The back scattering consists in the possibility of a single or multiple interaction able to change the direction of the particle up to a complete reversal, with the electron coming out from the impact surface.

1.1.3 Electromagnetic Radiation

Electromagnetic radiations have a different behaviour than charged particles. During the process of interaction the photons can completely disappear or scatter. Dependending on the energy, different models should be applied to describe the dynamics of the interactions, the main effects being:

- Photoelectric absorption
- Compton scattering
- Pair production

- Coherent scattering

The photoelectric absorption occurs when a photon disappears yielding completely its energy to an atom. As a consequence, an electron in the orbital of the atom will gain energy and, if the energy is big enough, it will be ionized. The atoms will lose an electron that should be quickly replaced. The excited electron energy is described by the equation 1.3:

$$E_{e^-} = hv - E_b \tag{1.3}$$

where E_b is the original energy of the electron in its orbital. The probability that a photoelectric absorption occurs depends on the photon energy and the atomic number of the target media. The probability can be calculated by the equation 1.4:

$$\tau \cong constant \times \frac{Z^n}{E_\gamma^{3.5}} \tag{1.4}$$

where n is a number between 4 and 5.

The Compton scattering describes the collision phenomena between a photon and an electron. The photon gives away part of its energy, creating a scattered electron (called recoil electron) and a new photon of lower energy (1.5):

$$hv' = \frac{hv'}{1 + \frac{hv}{m_0c^2}(1 - cos\theta)} \tag{1.5}$$

m_0c^2 is the rest-mass energy of the electron (0.511MeV). The angular distribution is predicted by the Klein-Nishima formulation [36]. The probability of interaction for Compton scattering is proportional to the number of electrons in the atoms and consequently to Z. At higher energy ($\geqslant$ 1.02 MeV) a new effect becomes possible, called pair-production. The probability of interaction in this case cannot be expressed by a formula, but it follows approximately the rule of $\sqrt{Z}$.

Neutron classification	Energy (meV)	Velocity (m/s)	λ (nm)
Ultra-cold	0.00025	6.9	57
Cold	1	437	0.9
Thermal	25	2187	0.18
Epithermal	1000	13832	0.029
Fast	>1000	>13832	<0.029

Table 1.1: Neutron characteristics at various energies [1]

1.1.4 Neutrons

Neutrons, like photons, do not have an electrical charge and consequently are not affected by the Coulomb law. They interact mainly with nuclei and for this reason they can penetrate the matter for relatively long distances ($\sim$ centimeters) before being entirely absorbed or scattered. With a spin of 1/2, neutrons interacts with the magnetic field and, in the matter, with the magnetic moment of unpaired electrons. Quantum mechanics governs the interactions between neutrons and nuclei, but a classical unit to describe the probability of interactions is the cross section σ. Its units is the barn and it corresponds to $10^{-24}\ cm^2$. The neutron energy is classified as shown in Table 1.1 [1] depending on its energy, which strongly affects the cross section.

In slow neutrons the kinetic energy is low and the possibility to interact by nuclei scattering is very low. In this case there is a high cross section for absorbing the neutron that induces nuclear reactions. The Q-value of the reaction can be big enough to generate particles that can be easily detected. The possible reactions are (n, γ) and can be difficult to be detected because of the γ-background, and (n, α), (n, p) and $(n, fission)$ that are the most convenient for detectors. On the contrary, fast neutrons are characterized by very low cross section for absorption but their particle energy makes them suitable for scattering. The main differences between scattering and

absorption is in the outgoing particles energy and angles. For absorption the angle is random and the energy depends on the Q-value of the reaction. For scattering, the recoil particles have an energy and an angle described by the formula 1.6:

$$E_R = \frac{4A}{(1+A)^2}\left(\cos^2\theta\right)E_n \tag{1.6}$$

where A is the mass of target nucleons, E_n is the neutron energy and θ is the recoil nuclei angle that can be calculated from 1.7:

$$\cos\theta = \sqrt{\frac{1-cos\Theta}{2}} \tag{1.7}$$

where Θ is the scattered neutron angle. For fast neutrons the maximum energy of the recoil atoms is the maximum energy of the neutron.

1.2 Interaction of Radiation with Silicon

Silicon plays a major role in solid state detectors for the possibility to use the same fabrication techniques developed in microelectronics. Silicon is a semiconductor with atomic number Z=14 and a density of 2.329 g/cm^3.

1.2.1 Nuclear particles

Charged particles interact with silicon by a mechanism governed by Coulomb force as described in section 1.1.1. By replacing Z=14 in the Bethe-Block formula reported in equation 1.1 it is possible calculate the energy loss in Silicon. Unfortunately not all the terms of the equation are known and the exact calculation is not possible. When a charged particle interacts with matter the released energy has statistical fluctuations depending on the number of collisions and on the scattering events. The resulting spectra of released energy in material is described by the Landau distribution [37]. For silicon the most probable value (MPV) of the Landau distribution depends

on the thickness of the detector. Figure 1.2 shows the MPV scaled to the mean loss at minimum ionization for several silicon thicknesses.

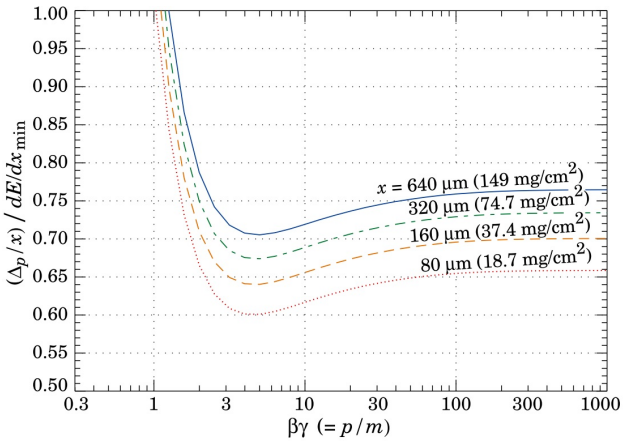

Figure 1.2: MPV scaled to the mean loss at minimum ionization (388 ev/μm) for several silicon thicknesses [5]

The average ionization energy (E_{ion}) valid for energies much larger than the band gap (E_G) follows the rule $E_{ion} \cong 2.8 \cdot E_G + 0.6eV$ and for Silicon is $E_{ion} = 3.6eV$. It is three times larger than the band gap because part of the energy is involved in lattice thermal vibrations (creation of phonons). For a m.i.p. (Minimum Ionizing Particle) that traverses a detector with a thickness of 300μ the MPV of released charge is around $76e^-$. The total charge generating from the detector for a m.i.p. is only ∼3.6fC, so the front-end circuit must be able to process such a small signal.

Due to the density, alpha particles have a short range in silicon of just a few micrometers. Figure 1.3 shows the range-energy curves calculated for different charged particles in silicon. An α-particle with an energy of 5 MeV has a range of less than $\cong 20\mu$m.

The cross section for thermal neutronx is extremely low (only $\cong$2.24 barn). The mean free path before a scattering or capture event is around $\cong$8.6 cm.

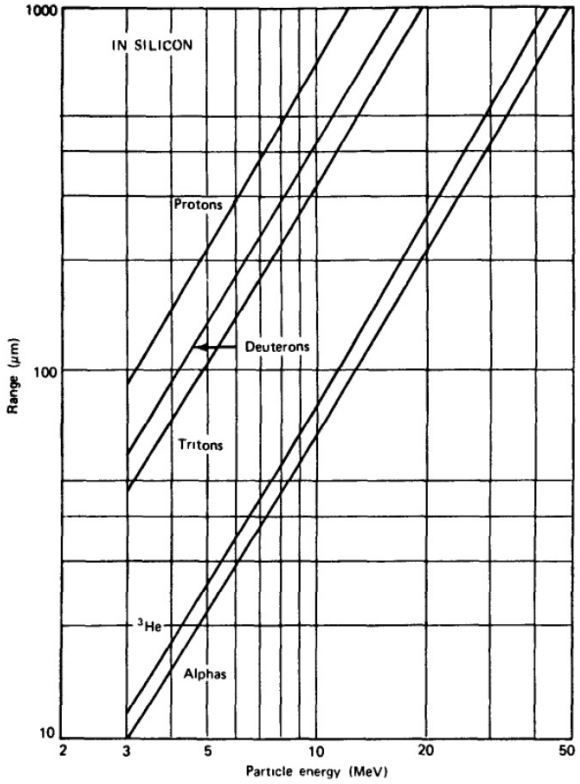

Figure 1.3: Range energy calculated for different radiation particles in silicon[6]

1.2.2 Photons

Photons in silicon can release energy only if their energy is larger than the band gap; the corresponding maximum wavelength λ is $\approx$1.11μm. This is related to the band structure described in section 1.3. The Lambert-Beer's law is $I(x) = I_0 \exp^{-\alpha \cdot x}$ where I(x) is the intensity, x is the photon penetration in the silicon, I_0 is the intensity of incoming light and α is the absorption coefficient. Figure 1.4 shows the photon absorption coefficient as a function of the photon energy.

In silicon, the photoelectric effect is predominant up to 100keV. Beyond this energy threshold Compton scattering becomes the most effective; only at energies higher than 10MeV the absorption coefficient becomes dominated by pair production.

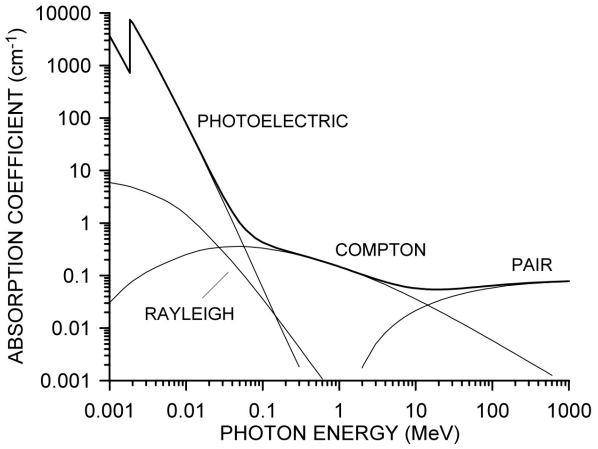

Figure 1.4: Photon absorption coefficient vs. energy in silicon [7]

1.3 Elements of semiconductor detectors

Silicon used in the electronics industry and for radiation detectors is composed by mono crystal with a diamond cubic lattice structure. The possible cutting planes are identified by the Miller indexes. The solution of the Schrödinger equation using the Bloch theorem provides as solution an energy band structure with a band gap. It is an indirect semiconductor (the minimum distance between valence and conduction bands is not in correspondence of the same k) with a band gap of 1.12eV at room temperature. Obtaining pure silicon is very difficult; for this reason most of the detectors are doped in order to make a P-N junction. The charge carrier dynamics is described by the drift-diffusion 1.8 and continuity equations 1.9 :

$$\begin{cases} J_n = q\mu_n n\vec{E} + qD_n \nabla_n \\ J_p = q\mu_p p\vec{E} - qD_p \nabla_p \end{cases} \tag{1.8}$$

$$\begin{cases} \frac{\partial n}{\partial t} = G_n - U_n + \frac{1}{q}\nabla \cdot J_n \\ \frac{\partial p}{\partial t} = G_p - U_p - \frac{1}{q}\nabla \cdot J_p \end{cases} \tag{1.9}$$

where J_n and J_p are the current densities, μ_n and μ_p are the mobilities,

D_n and D_p are the diffusivities for the electrons and holes of densities n and p, respectively. The terms G_n and G_p are the electron and hole generation rates and U_n and U_p are the terms of net recombination. In steady-state condition the relations $G_n = U_n$ and G_pU_p hold.

PIN diodes

Most silicon radiation detectors are composed of P-N junctions. The basic theory of P-N junction is described by Shockley, Sah, Noyce and Moll [38] [39]. A diode is composed by doped silicon crystals in order to have a change of concentration of acceptor impurities (Na) and donor impurities (Nd). In steady-state condition, due to diffusion, there is a internal potential called built-in potential V_{bi}. This means that at zero Volt bias ($V_{bias} = 0$) there is a depleted region that is then further extended when reverse bias is applied. In case of abrupt junction, the depletion region width (W) can be calculated by the equation 1.10:

$$W = \sqrt{\frac{2\epsilon_s}{Q}\left(\frac{N_A + N_D}{N_a N_D}\right)(V_{bi} + V_{bias})} \tag{1.10}$$

The full depletion voltage is then proportional to the square of the silicon thickness. If the applied voltage is higher than the full depletion voltage, the device is said to be "over depleted". A leakage current is present, mainly due to thermal generation in the depleted bulk and at the surface. The bulk thermal generation current per unit of area J_{lk} can be approximated with equation 1.11:

$$J_{lk} \simeq -q\frac{n_i}{\tau_g}W \simeq -q\frac{n_i}{\tau_g}\sqrt{\frac{1\epsilon_s}{qN_D}V_{bias}} \tag{1.11}$$

where τ_g is the carrier generation lifetime and n_i is the intrinsic carrier concentration. Equation 1.11 relates the current to the depletion volume that depends on the applied voltage as described in the equation 1.10. It is

therefore possible to predict the theoretical current-voltage characteristic: the current increases proportionally to the square root of the voltage until full depletion is reached. After that, the current should saturate, unless significant contributions from surface are present.

n_i and τ_g have a strong dependence with the temperature. Those dependences can be transferred to the current with the equation 1.12:

$$J_{lk} \propto T^2 e^{-E_g/2kT} \tag{1.12}$$

The described behaviour is valid until the internal electrical field does not reach the critical value for which breakdown phenomena start to increase the current value. The three main breakdown phenomena are: thermal instability, tunnel effect and avalanche that is the predominant one in radiation detectors. For the avalanche effect the critical electric field value that engages breakdown is reported in equation 1.13:

$$E_{crit} = \frac{4 \times 10^5}{1 - \frac{1}{3} log_{10}(N_B/10^{16})} \tag{1.13}$$

Where N_B is the ionized background impurity concentration of the lightly doped side.

The breakdown voltage (V_{bd}) is quantifiable by the relation 1.14:

$$V_{bd} \sim \frac{\epsilon_s}{2qN_D} E_{crit}^2 \tag{1.14}$$

A reverse biased detector has a capacitance to the backplane that can be estimated with reference to a parallel plate capacitor having a thickness equal to the depletion width. At full depletion the capacitance should saturate at a minimum value dependent on the detector thickness.

1.3.1 Charge motion and signal formation

A radiation that interacts with silicon can generate electron-hole pairs in the detector. Equation 1.8 of drift-diffusion describes the charge motion.

Considering the two effects separately, for the diffusion the charge will move according to the charge concentration gradient and spread out in time with a Gaussian shape with a variance of 1.15:

$$\sigma = \sqrt{Dt} \tag{1.15}$$

where D is the diffusion constant (diffusivity) and t the time. For the drift effect the charge will move driven by the electric field with a velocity that can be expressed as 1.16:

$$\vec{v_{n,p}} = \mu_{n,p}\vec{E} \tag{1.16}$$

where $\mu_{n,p}$ are the mobilities of electrons and holes.

The particle detection can start as soon as charges start their motion. The current induced on the electrodes was formally described by S. Ramo with the following equation 1.17[40]:

$$i(t) = -q\vec{v}(t) \cdot \vec{E_w} \tag{1.17}$$

where $\vec{E_w}$ is the so-called weighting field. It is important to remark the electric field and and weighting field are different. The weighting field can be obtained by applying unit potential to the electrode under consideration and zero potential to all the others. The internal electric field plays, anyhow, a very important role, since the carrier velocity and the charge path depends on it. Radiation damage in the detector bulk or at the surface can deteriorate the amount of collected charge. Trapping can remove part of the generated and moving charge. Depending on the nature of traps, temperature and electric field the traps can give back the charge creating a delayed charge collection. Considering Q_0 the moving charge, it will decay with the following law 1.18:

$$Q(t) = Q_0 e^{-\frac{t}{\tau}} \tag{1.18}$$

where τ is the trapping time. Further information on radiation damage will be given in 1.5

1.3.2 Energy resolution

An important feature in radiation detectors is the ability to distinguish the different energies of incoming particles. This capability is required in spectroscopy where it is necessary to distinguish particles having nearly the same energy. As already described in section 1.2.1 the average number of electron-hole pairs N_{ave} generated by X-rays or by short range particles can be calculated by the equation 1.19:

$$N_{ave} = \frac{E}{E_{ion}} \tag{1.19}$$

However, in case of a monochromatic source, due to the statistic nature of charge generation process, the corresponding energy spectrum will not be a single line, but rather a Poisson distribution. The Full Width at Half Maximum (FWHM) and the standard deviation of the Gaussian are given by the following equations 1.20:

$$\begin{cases} \sigma = \sqrt{N_{ave}} E_{ion} \\ FWHM = 2.35\sigma = \frac{dE}{E} N_{ave} \sigma \end{cases} \tag{1.20}$$

Combining the two equations it is possible to obtain 1.21:

$$\frac{dE}{E} = 2.35 \sqrt{\frac{E_{ion}}{E}} \tag{1.21}$$

Considering the dependence on the radiation energy, the material (and its band gap) should be accurately chosen for optimizing the energy resolution. Nevertheless, measurements show significant differences between the expected energy resolution and the one obtained in laboratory. In particular there is a factor of 3-4 between the theoretical resolution and

the experimental one. This discrepancy is caused by the non-independent process of generation of electron–hole pairs and phonons. In order to take in account this effect, the equation should be corrected as follows 1.22 [36]:

$$\frac{dE}{E} = 2.35\sqrt{F\frac{E_{ion}}{E}} \tag{1.22}$$

where F is called Fano factor and for silicon is close 0.1 [41]. Of course, besides the intrinsic fluctuation in the generated charge, the energy resolution is influenced by the noise in the read-out electronics.

1.4 Front-end electronics for radiation detectors

Radiation detector read-out can have many different configurations. The most relevant ones are the current sensitive amplifier and the charge sensitive amplifier (CSA). Current sensitive amplifiers are based on transimpedance amplifiers that convert a current signal to a voltage signal and amplify it. This kind of configuration is often used in measurements where the signal shape is important. An example is the Transient Current Technique where the observation of signal shape allows to estimate the charge dynamics of the device under test. In case it is not necessary to know the signal shape but only the collected charge, architectures based on charge sensitive amplifier are preferred. CSA was ideated by Emilio Gatti [42]: it is basically an inverting amplifier circuit (see Fig. 1.5) that ideally gives an output voltage proportional to the charge at its input charge and to the feedback capacitance.

Considering the reset switch open, the Voltage gain for unit of charge will be equal to 1.23:

$$A_Q = -\frac{Q_{in}}{C_f + \frac{C_D+C_i+C_f}{A}} \rightarrow -\frac{Q_{in}}{C_f} \tag{1.23}$$

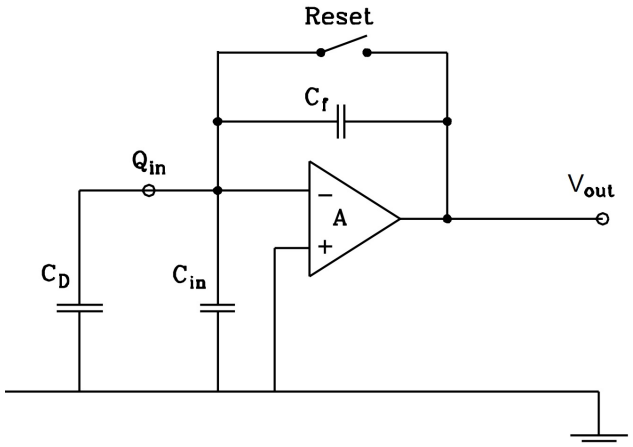

Figure 1.5: Semplified schematic of an CSA architecture [8]

The input dynamic capacitance is equal to 1.24:

$$C_{eff} = (A+1)C_f + C_i \tag{1.24}$$

The total transfer of charge with sensitivity loss from the detector to the electronics is possible only if $C_{eff} >> C_D$. In addition to the CSA, usually a calibration capacitance is connected. The simple injection circuit is composed by a capacitance (C_T) connected to the input of CSA. If the relation $C_T >> C_{eff}$ is satisfied the injected charge will be equal to 1.25:

$$Q_T = \frac{C_T}{1 + \frac{C_T}{C_{eff}+C_d}}\Delta V \approx C_T(1 - \frac{C_T}{c_{eff} + C_d})\Delta V \tag{1.25}$$

Many different solutions, depending on the application and rate of particles, are suitable for the implementation of the reset switch. For low events rates, the easiest solution is represented by a resistor in parallel to the feedback capacitance. Summarizing, the CSA output is a voltage proportional to the injected charge on the input. The number of events that contribute to build a spectrum is generally very high and a conditioning of the signal is required. The most common solution is a filter circuit called ”shaper”, that allows to optimize the Signal to Noise ratio (SNR)

and reduce the signal to a pre-determined timing. The transfer function of the best filter can be determined by the reduction of the SNR. Assuming $Q_1 \cdot s(t)$ to be the signal carrying the information about the parameter to be measured, $N(\omega)$ the spectral power density of the noise associated with $Q_1 \cdot s(t)$ and $H(j\omega)$ the unknown transfer function of the network which leads to the optimum, the SNR^2 will be equal to 1.26:

$$SNR^2 = \frac{Q_1^2}{2\pi} \frac{[\int_{-\infty}^{\infty} H(j\omega)S(\omega)e^{j\omega t})\, d\omega]^2}{\int_{-\infty}^{\infty} N(\omega)|H(j\omega)|^2\, d\omega} \tag{1.26}$$

Starting from this SNR definition of equation, using the Schwartz inequality is possible to define the minimum noise as reported in 1.27:

$$SNR^2 \leq \frac{Q_1^2}{2\pi} \int_{-\infty}^{\infty} \frac{|S(\omega)|^2}{N(\omega}) \, d\omega \tag{1.27}$$

The transfer function of the filter which makes SNR to reach the limit is 1.28

$$H(j\omega) = k' \frac{S^*(\omega)}{N(\omega}) e^{-j\omega\tau_m} \tag{1.28}$$

where the τ_m is the value of the signal at the measurement time.

Therefore, the optimum filter (or matched filter) has as delta-response the mirror image of the signal present at its input.

The matched filter has the following transfer function 1.29

$$h(t) = -Ke^{\frac{t}{\tau_c}}t \tag{1.29}$$

where τ_c is called noise corner time constant and is the reciprocal of the frequency at which the contributions from series and parallel noise at the pre-amplifier input become equal. The need of working with finite peaking time suggests that only a part of the output signal can be used. The SNR degradation is only 8% if $\tau_m = \tau_c$.

1.4.1 Noise in readout electronics

In the hypothesis of time invariant systems, the noise components can be modelled as white series noise and white parallel noise. Figure 1.6 is a representation of the read-out circuit with the addition of noise components. In particular series noise is symbolized by a voltage source with an amplitude A_W and parallel noise with current source of amplitude B_W.

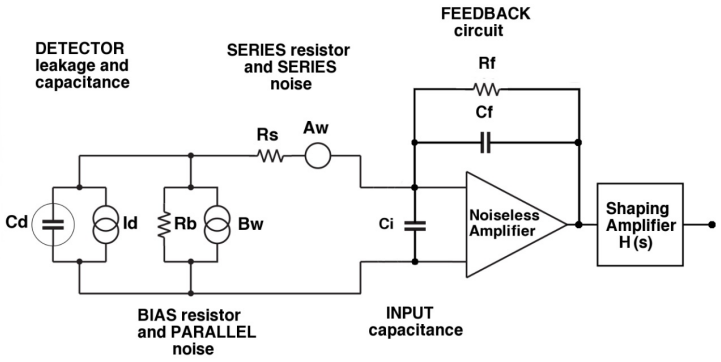

Figure 1.6: Schematic model of all noise sources in a CSA-shaper circuit

After several mathematical passages, the output mean square noise voltage can be expressed as in equation 1.30 where the input signal is a Dirac impulse of area Q.

$$\overline{v_{u,N}^2} = A_W \frac{C_T^2}{C_f^2} \frac{1}{2\pi} \int_0^\infty |H(j\omega)|^2 \, d\omega + A_f \frac{C_T^2}{C_f^2} \int_0^\infty \frac{|H(j\omega)|^2}{\omega} \, d\omega + B_W \frac{1}{C_f^2} \frac{1}{2\pi} \int_0^\infty \frac{|H(j\omega)|^2}{\omega^2} \, d\omega \quad (1.30)$$

where A_f represents the 1/f noise and $C_T = C_D + C_i + C_f$. The shaping factors are defined as in equations 1.31 and their values are tabulated in literature for different types of filters:

$$\begin{cases} A_1 = T_P \frac{1}{2\pi} \int_0^\infty |H(j\omega)|^2 \, d\omega \\ A_2 = \int_0^\infty \frac{|H(j\omega)|^2}{\omega} \, d \\ A_3 = \frac{1}{T_P} \frac{1}{2\pi} \int_0^\infty \frac{|H(j\omega)|^2}{\omega^2} \, d\omega \end{cases} \tag{1.31}$$

The square of the equivalent noise charge is expressed as (1.32)

$$ENC^2 = A_W C_T^2 \frac{A_1}{T_P} + A_f C_T^2 A_2 + B_W A_3 T_P \tag{1.32}$$

By analysing the individual terms in the equation it is possible to note:

- A_W depends on the current in the input transistor. The shaping time should be as long as possible if the total capacitance is high.
- B_W depends on the gate current of the input transistor, the detector current and the thermal noise of the feedback resistance and of the bias resistance. The shaping time should be the shortest possible if the currents are high.
- A_f depend of the input device and is independent of the shaping time

Figure 1.7 summarizes the trend of the ENC for the different noise contribution.

1.5 Radiation damage in silicon

The performance of radiation detectors degrade because of the highly radioactive environment in which they operate. Long term interactions between particles and matter can change the detector behaviour from the electrical and functional points of view. It is possible to distinguish two main effects of damage: bulk damage and surface damage.

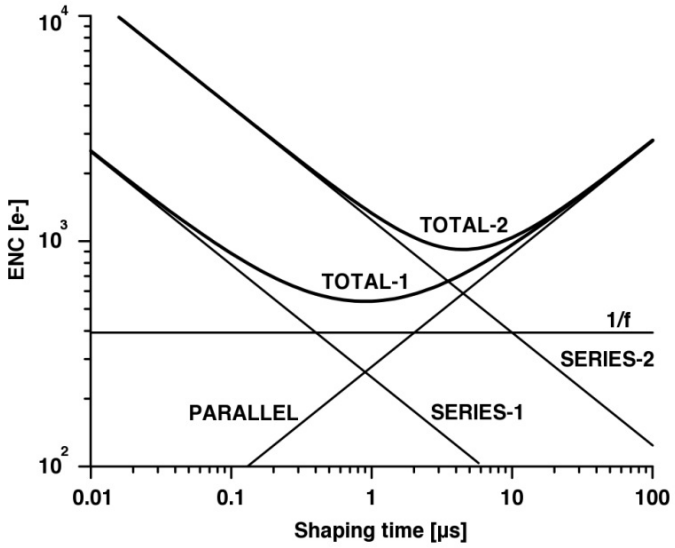

Figure 1.7: Different contributions to the ENC: parallel, series and 1/f noise versus shaping time [7]

1.5.1 Bulk damage

Particles travelling through the detector bulk can displace silicon atoms from their lattice positions creating defects. The resulting damage causes interstitial and vacancies and is called Primary Knock-on Atom or Frenkel[43]. The threshold energy to activate this mechanism is $E_d \sim 25eV$ for silicon. If the particle energy is much higher than E_d, the atom of recoil can generate clusters of damage. The damage is different for different types of radiation. Particles like neutrons that do not have a Coulomb barrier opposing the impact with nuclei are more effective. The common method to indicate and compare the irradiation damage is to refer to the equivalent damage of a mono energetic flux of neutron with an energy of 1MeV. The three main macroscopic effects are: an increase of the leakage current, a change in the effective bulk concentration and charge trapping. The leakage current is related to the new levels in the forbidden band gap that increase significantly the generation-recombination mechanisms. The increase of current follows the relation 1.33 [44]:

$$\Delta I = \alpha \Phi_{eq} V \tag{1.33}$$

where α is a constant of damage, Φ_{eq} is the fluence expressed in 1 MeV neutron equivalent and V is the volume of the depleted sensor.

The effective bulk doping concentration is changed according to the capture of dopant atoms in complex defects that change the doping property. In many cases (in particular for N-type doping) an inversion of effective doping can happen at high fluences.

The radiation induced increase in the density of energy levels in the forbidden band gap can capture free charge (and consequently signal) reducing the charge collection efficiency [45]. The capture probability per unit time is 1.34:

$$\frac{1}{\tau_{n,h}} = \sum_t N_t (1 - P_t^{e,h}) \sigma_t^{e,h} v_{th}^{e,h} \tag{1.34}$$

where N_t is the defect concentration, $P_t^{e,h}$ is the occupation probability for electrons and holes, $\sigma_t^{e,h}$ is the trap cross section and $v_{th}^{e,h}$ is the thermal velocity.

The term $\frac{1}{\tau_{n,h}}$ depends linearly with the fluence [8].

1.5.2 Surface damage

Radiation damage also affects the oxide (or any other insulator) material and the interface, giving rise to:

- Interface trapped charge: defects at the interface create traps (levels on the forbidden bandgap) with a charge dynamically dependent on the electric field. Their main effect on the device properties is a possible increase of the surface recombination and, therefore, of the surface current.

- Oxide charge: the charge trapped within the oxide bulk can, in absolute terms, increase (e.g., in Silicon oxide) or decrease (e.g., in Aluminium oxide), thus changing the electrical properties of the insulator and its ability to passivate the surface [46].

  The change of charge in the insulator can, through the MOS effect, affect the electrical behaviour of the sensors (e.g., the isolation between neighboring regions, the interstrip capacitance and the breakdown voltage).

CHAPTER 2

State of the art of silicon neutron detectors

The helium isotope ^3He started to be marketed for research applications in the early 80s and it was massively used for slow neutron detection. High efficiency of neutron conversion and low gamma sensitivity made ^3He a "gold standard" for neutron detection [47]. The common Helium is composed by a major part of ^4He isotope and only few parts per million of ^3He [48]. Most of the production is obtained by the radioctive decay of tritium. It plays an important role in the enhancement of nuclear weapons power. The ^3He was obtained as by product from the maintenance of purity of tritium. The end of Cold War partially stopped the nuclear weapons race and consequently the production of ^3He decreased, so that the demand exceeds to the supply [49]. The lack of this gas generated a big increase of its price and other detection solutions had to be considered.

The main types of slow neutrons detectors can be obtained from gas, solid state detectors or using scintillator materials. The technology is chosen considering the spatial accuracy and the requirements of active area in the application. For large areas, the main thecnologies are boron-

lined proportional detectors, boron trifluoride (BF_3) proportional detectors, and lithium scintillators [50]. The boron-lined proportional detectors are composed by a tube filled with a mix of gasses with a thin layer of ^{10}B placed on the internal surface. The efficiency reached is around 10-15 % and, for this reason, in order to be comparable in efficiency to ^3He, these detectors have to be used as arrays [51]. Boron trifluoride (BF_3) proportional detectors share the same thecnology of ^3He tubes but replacing the converter gas. They have an efficiency of 30-50 % compared the ^3He. They are the least expensive of the three alternatives but BF_3 is a very toxic material [52]. The lithium scintillators consist in coating optical fibers with scintillating materials. A neutron is converted into a charged particle by the ^6Li, the particle is converted to light by the scintillator, and the light is detected by photodetectors coupled with the optical fiber [53]. Solid state detectors for neutrons can be suitable for applications that require small active area and very high spatial resolutions. They can be divided in two categories, depending on the design approach. The first approach regards neutron-sensitive materials (e.g., $LiInSe_2$,hBN), where most of the charge from the particle reaction is available for transduction within the sensor itself [54][55]. As a result, the efficiency can be very high, but this approach is very difficult: the main problem is the crystal quality and the understanding of defects that significantly reduce the signal charge collection[56] [57]. The second approach uses semiconductor sensors coated with thin films of neutron converter materials: of course, the mean free path of the neutron reaction products should be long enough to penetrate in the semiconductor sensor depleted region, where they induce a ionization signal.

2.1 Gaseous detector

Gaseous detectors are devices containing a certain volume of gas mixture in which, between two biased electrodes, there is a high electric field. The ionization of the gas in the chamber is a measure of the radiation. By using gasses reactive to neutrons it is possible detect neutrons. The main three neutron gaseous detectors are based on ^3He and BF_3. The operating voltage is usually very high (hundreds or thousands volts). They are normally used when covering large areas is important. The dead time (200-400 μs) is the most limiting factor because it causes low counting rates.

It is possible to distinguish three main types of neutron gaseous detector: proportional counters filled with ^3He gas, proportional counters with BF_3 and boron-lined proportional counters.

The proportional counter filled with ^3He exploits the absorption of nuclear reaction of this isotope with neutrons described in the reaction 2.1:

$$^3He + n \longmapsto ^3H +^1 H + Q \tag{2.1}$$

where the Q value is 764 keV. The two reaction particles are emitted with opposite directions. Figure 2.1 shows a schematic example of proportional counter filled with ^3He.

The ^3He gas is intrinsically not sensitive to gamma rays. The γ-rays that interact with the wall of the tube release electrons that traverse the gas releasing low amount of energy (usually it is a m.i.p). On the contrary, charged ions released by the reaction product are stopped and the release of energy is much bigger than a m.i.p.. Using this principle it is possible to have a high rate of discrimination between neutrons and gamma rays. Proportional counters with BF_3 uses essentially the same technology by replacing ^3He with BF_3.

Boron-lined proportional counters share the same working principle but

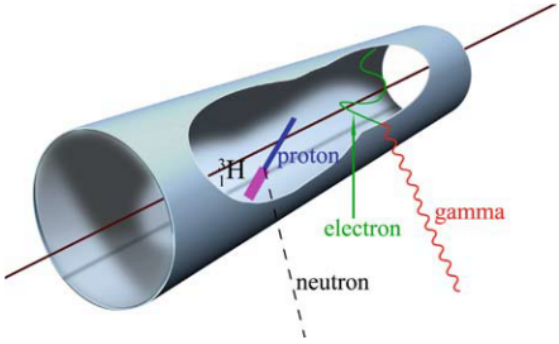

Figure 2.1: A sketch of a proportional counter filled with ^3He [9]

the reactive material is not the gas but the solid coating of boron compound deposited inside the tube.

2.2 Thin-film coated neutron detectors

Neutrons do not interact significantly with the semiconductor materials commonly used in microelectronics as already discussed in Chapter 1. One possible solution is to use a converter material in order to convert the incoming neutrons into charged particles or photons that can be detected by semiconductor devices. A good material converter stands out for its high cross sections for neutron; moreover, the reaction product must have a high Q-value of reaction and the particle coming from the nuclear reaction should be easy to detect. The candidate materials are: Boron-10 (^{10}B), Lithium-6 (^6Li), Gadolinium-157 (^{157}Gd) and Cadmium-113 (^{113}Cd). For thermal neutrons (25.9eV) the highest cross sections are found in ^{157}Gd (240000 b) and ^{113}Cd (20000 b); Boron and Lithium have significantly lower cross sections of 3840 b for ^{10}B and 940b for ^6Li [58].

Gadolinium, despite the high cross section, is rarely used for detector because the nuclear reaction products induced by neutrons are γ-rays in a

range of energy up to 9 MeV and electrons in the range 29-250keV, that are difficult to be detected. Figure 2.2 shows the simulated energy of electrons from the neutron reaction in 250 μm thick natural Gd converter [10].

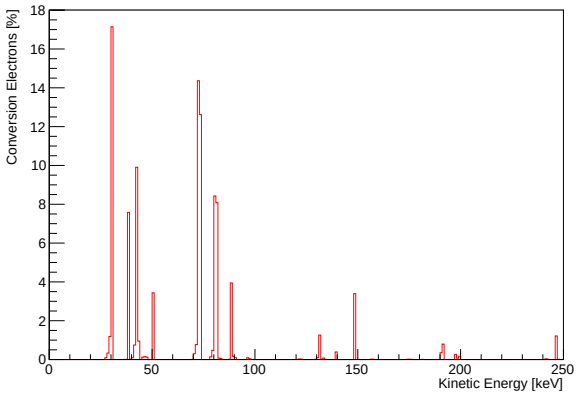

Figure 2.2: Kinetc energy of electron in 250 μm thick natural Gd converter [10]

The reaction for Cadmium is similar to the Gadolinium one with emission of gamma. The reaction is described by equation 2.2 with gamma emission reported in Fig. 2.3. Unfortunately, neutron sources have usually a gamma background that makes very difficult to distinguish the gamma from the background reaction.

$$^{113}Cd + n \longmapsto ^{114}Cd + \gamma \tag{2.2}$$

The neutron reactions for ^{10}B and ^{6}Li are reported in the following equations 2.3 and 2.4. In both cases the reaction products are released in opposite directions.

$$^{10}B + n \begin{cases} \overset{94\%}{\longmapsto} \alpha(1.47MeV + ^{7}Li(0.84MeV) + \gamma(0.48MeV) \\ \overset{6\%}{\longmapsto} \alpha(1.78MeV + ^{7}Li(1.01MeV) \end{cases} \tag{2.3}$$

$$^{6}Li + n \longmapsto ^{3}H(2.72MeV + \alpha(2.05MeV) \tag{2.4}$$

It should also be noted that the cross section values are inversely proportional to the neutron energy following the $1/v$ law.

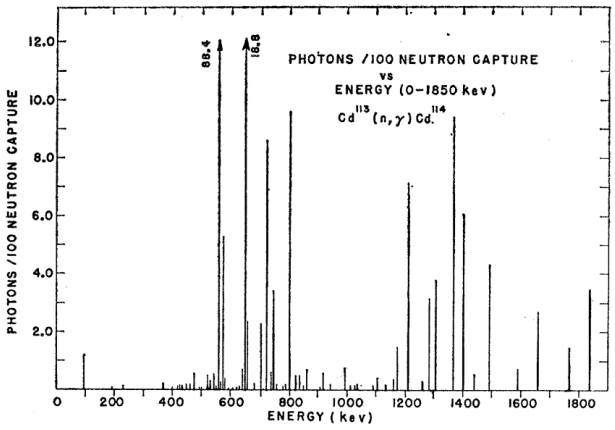

Figure 2.3: γ spectra of ^{113}Cd caputure reaction [11]

2.2.1 Developments based on Boron and Lithium

The working principle for the detector is to have a thin film of converter material touching a detector sensitive to charged particles. Charged particles interact with the matter by Coulomb scattering as discussed in section 1.1.1 and their detection is very efficient in semiconductors. But the range of the reaction products is usually small, of the order of few μm, and this creates two main problems for the measurement: the self absorption of the particle in the converter layer and the need to minimize the dead layer thickness between the active area of the detector and the converter layer.

Particles generated from absorption nuclear reaction start to lose energy immediately after they start moving. Part of the energy is released in the converter by reducing the charge generated in the active area of the semiconductor detector. In extreme cases, if the converter thickness is not optimized or a combination of angle and initial position is not particularly efficient, the particles can be stopped and the energy is entirely released in the converter material. These effects are called self-absorption and can affect dramatically the efficiency of the detector. The other main problem is related to the the dead layers between the converter layer and

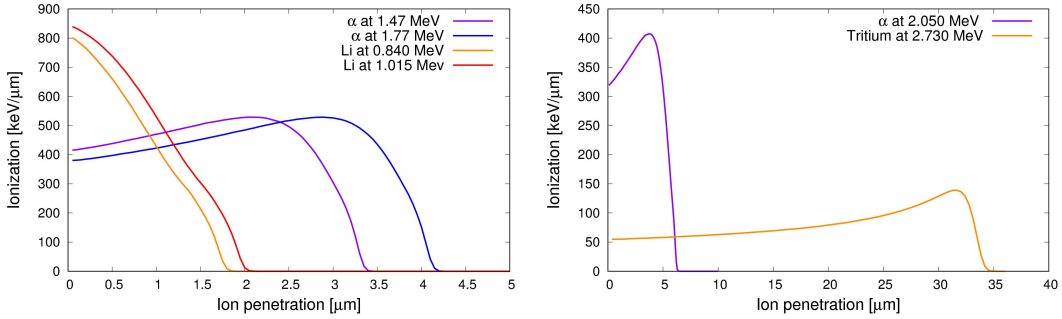

(a) Ion range in ^{10}B (b) Ion range in ^{6}LiF

Figure 2.4: Range of reaction products for ^{10}B and ^{6}LiF

the semiconductor. In fact a semiconductor requires to have metal contact on the interfaces, high doping regions or passivation layers that are not efficient at all for the particle detection.

The possibility of using different converter materials like pure Boron or Lithium or their compound changed substantially the properties of the converter material. Neutron-Boron reactions produce two different possible reactions with different ion energy. Making a SRIM [4] simulation it is possible to calculate the range of the products of reaction in Boron and Lithium. Figure 2.4(a) shows the maximum range and the energy distribution (and related Bragg peak) of the products for both possible reactions. The maximum range for the products of reaction is respectively $\sim$ 3.5-4 μm for the alpha particle and $\sim$ 1.7-2 μm for the lithium ions. The mass and the energy of Lithium reaction product are very different compared the Boron ones; their range is reported in figure 2.4(b). In this case the maximum range for alpha particles is $\sim$ 6 μm and $\sim$ 33μm for the tritium in lithium fluoride compound. Pure lithium could be an option to be used as converter but it has a corrosive and reactive nature [59], so that LiF is usually preferred.

In planar sensors, the coating thickness is the key factor for obtaining

good results. It depends on the maximum range of the reaction products and can be analytically calculated for orthogonal back and front irradiation. Further details can be found in [12].

Figure 2.5 shows the calculated front and back thermal neutron detection efficiency on dependence of the converter thickness. The different range of reaction products justifies the difference in the optimum thickness of the converter: if a generated ion does not have the possibility to escape from the converter, it will not contribute to the neutron detection. In case of front illumination the ^{10}B converter can reach the maximum efficiency of 4% with 2.8μm with a fast decrease for greater thickness. In the same configuration ^{6}LiF can reach 4.4% with a thickness of 12μm with a gradual decrease for higher converter thicknesses. The different shapes are related to the big difference of neutron cross sections between the two materials. In case of back illumination the neutron flux does not suffer attenuation due to the absorption of the excess converter material which does not take part in the neutron sensing. This allows to reach a slightly better efficiency with a desensitization of the neutron converter material thickness.

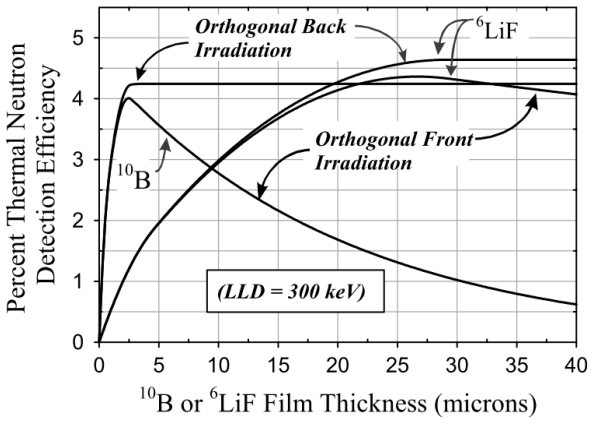

Figure 2.5: Calculated thermal neutron detection efficiency for different converter materials.[12]

Starting from late 1960s many groups started research in this field using

pure Boron or Lithium or their compounds [60][61] [62][63] [64]. In the past few years several research groups have been very active in this field, especially in the USA: among them, Kansas State University, Lawrence Livermore National Laboratory (LNL) , Rensselaer Polytechnic Institute.

In order to make solid state detectors competitive with ^3He and possibly replace it, the planar sensor efficiency and the gamma discrimination should be improved. To this purpose there are two main solutions, or a combination of both: stacked detectors or 3D detectors. The total absorption thickness of thermal neutrons for ^{10}B and ^6Li is much higher compared to the best thickness of the converter and, for this reason, stacked detectors can be an option. The efficiency does not increase linearly with the number of layers. Each layer will absorb part of the neutron flux and the successive layer receives an attenuated neutron flux. The ideal converter thickness is not constant for each layer and should be carefully calculated, but an adequate combination of converter layers can give a theoretical efficiency of up to $\sim$ 50 % [12][65][66]. The main drawbacks of this approach are the very low gamma discrimination and the difficulty to make pixelated detectors. In both ^{10}B and ^6Li reactions a dependence between the direction of the reaction product and that of the incoming neutron does not exist. The combination of this principle and the short range of reaction products in the converter suggests to go for higher aspect ratio structures between silicon and converter that can be obtained using 3D technology. The 3D architecture for neutron detection was first proposed by Muminov and Tsvang in 1987 [67] and developed at the end of 90' by Schelten et al. [64] and Allier [68].

2.2.2 3D development at Kansas State University

Kansas State University has been active in neutron detector research since the dawn of 3D solid state neutron detectors. In depth studies of planar and

3D detectors with both ^{10}B and ^{6}Li converter material were developed with excellent results. At the beginning, 3D detectors were developed for their particular surface morphology that allows to have better boron adhesion as compared to planar detectors [69]. Boron coating suffers of delamination and also in case of thin layers can be an issue during the deposition. The mechanism used is to deposit boron with a higher stability induced by the footholds tranches. Cylindrical trenches with 3.5 μm in diameter spaced at 9.5 μm center-to-center and 1.7 μm depth were fabricated on a substrate of SI GaAs and were tested obtaining an efficiency of 4.3 % with a good converter uniformity[66].

The shapes, their mutual distance and the depth of trenches were investigated according to the technological capabilities available at the time the research was conducted.

Monte Carlo simulations for circular holes and parallel trenches were performed for both converter materials [70]. The simulation results, parametrized as a function of the cell size and the trench diameter promise high efficiency with the condition of having very small cells size and large cavity fractions. Particularly interesting is the difference of one order of magnitude of cell/trenches size between ^{10}B and ^{6}LiF for a similar efficiency[71]. This difference is due to the range of the reaction products and the bigger trench sizes are in favour of ^{6}LiF. For similar dimensions, efficiency results are very similar for parallel trenches with supporting flange between the trenches for strengthen the mechanical properties. Regular parallel trenches were used in a "sandwich" configuration with a significant increase of efficiency up to 50% for thermal neutron detection.

Neutron Monte Carlo simulations for determining the efficiency are made considering a flux perpendicular to the surface. In semiconductor perforated neutron detectors the direction of incoming neutrons strongly affects the efficiency results [72]. The trench geometry can contribute to have a reduced

efficiency variation. Sinusoidal trenches give a very low efficiency variation on dependence of the azimuthal and polar angles for both ^{10}B and ^{6}LiF converter materials [73].

Perforated detectors with different trench shapes were produced and tested under a thermal neutron flux [14] [74] [13] [75] [76]. They were fabricated on float zone silicon wafer with a thickness of 325 μm and etched using an ICP (Inductively Coupled Plasma)-RIE (Reactive Ion Etching) process for 100μm or 200μm and the perforation was passivated with native oxide or doped by diffusion as shown in Fig. 2.6. The neutron converter material considered was ^{6}LiF. Figure 2.7 shows the different patterns for the trenches: circular hole, straight trench, and sinusoidal trench.

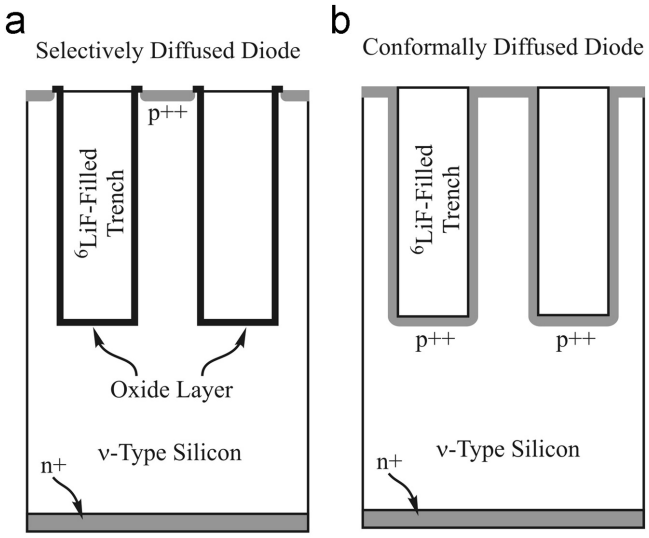

Figure 2.6: Cross-section for the different trench surface treatments [13].

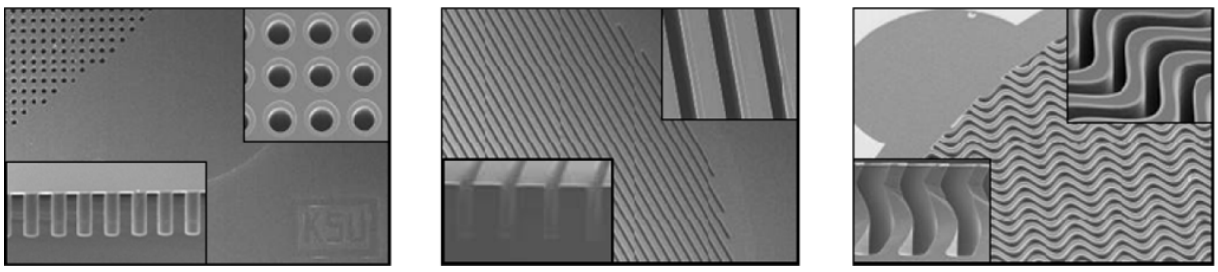

Figure 2.7: Different perforated micro-structure detector designs [14]

For incident thermal neutron fluxes the measured efficiency was 9.7%, 12.6% and 16.2% for circular, straight trench and sinusoidal trench devices, respectively. Strip detectors using perforated 3D detectors are possible and they were made successfully in arrays of 64 strips with a spatial resolution of 120μm [77].

Combining the 3D structure and stacked detectors can represent the state of the art in terms of maximum detection efficiency. The basic idea is to stack different 3D detectors with a spatial shift following the criterion of getting the trenches of the first detector coincident with the trench wall separation of the second detector. If the surface ratio wall/trenches is around one, neglecting the neutron absorption in silicon, all the incident neutrons will have the same probability to be absorbed (it will run into the same converter material). Back-to-back detectors were produced and tested with two depths of the trenches variants, obtaining a best efficiency of about 42% [78] [79][80] [81]. As for planar stacked solutions, the drawback is a higher sensitivity to the gamma background usually present in neutron source facilities. Anyway, they are very attractive for applications of direct ^3H replacement used in arrays and packaged in cylindrical containers similar to ^3H tube [82]. One way to combine some advantages of both solutions (3D and stacked and their combinations) is represented by double sided detectors. They consist of detectors processed from both wafer sided in order to have the stacked efficiency and the gamma sensitivity similar to a common 3D detector. However, they would be difficult to use in combination with a pixel front-end for imaging applications. Figure 2.8 shows the two technologies: complementary opposing trenches, that consist in the fusion of two detectors back-to-back, and interdigitated-trenches where the separation wall is etched becoming a trench on the other side. The advantage of the first solution is to have, as for the stacked solution, a good uniformity of efficiency along the surface, while the second solution

would lead to a faster charge collection lie in a 3D sensor. The thermal neutron detection efficiency is comparable toback-to-back stacked detector, but with an improvement of gamma discrimination due to lower sensitive material [15].

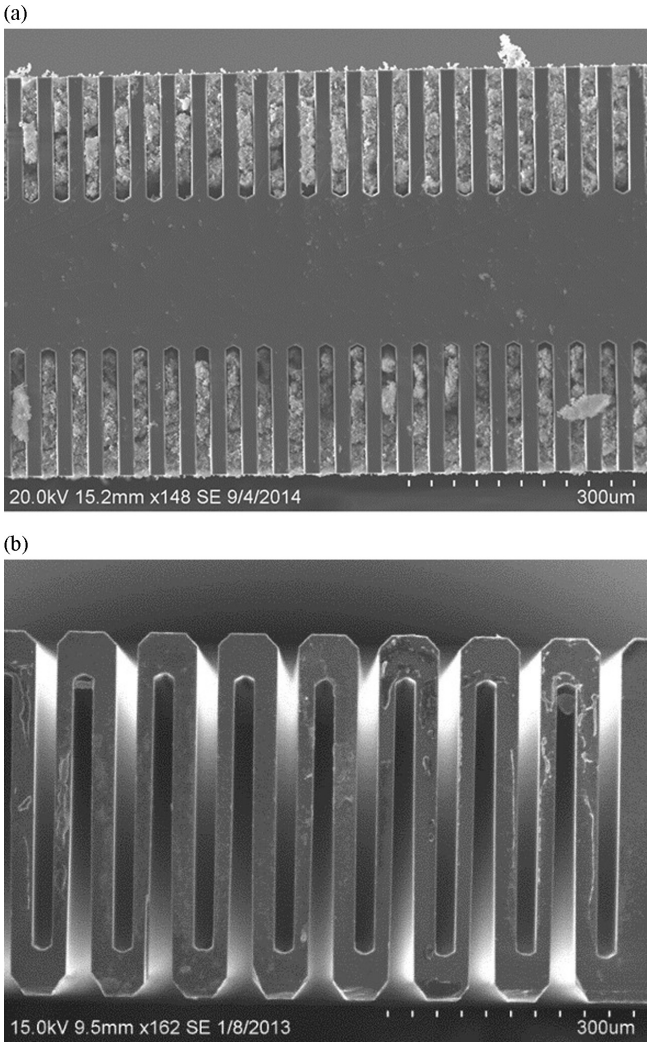

Figure 2.8: Different double-sided detectors: complementary opposing trenches and interdigitated-trenches [15]

As for stacked detector, double-sided detector can be a good solution for direct ^3He replacements [83].

2.2.3 Lawrence Livermore National Laboratory

The development of 3D neutron detectors at Lawrence Livermore National Laboratory began in 2005 with revolutionary geometries consisting of semiconductor pillars submerged in a converter material (^{10}B). Two different fabrication technologies were proposed: etching silicon substrates around the pillar or a selective grow of nanowire pillars by chemical deposition[16]. Of particular interest are the pillar inter-distance, the diameter and the height of the pillar. Figure 2.9 shows two representative cases: 100nm and 2μm diameter pillars respectively interspaced of 100nm and 2μm on dependence of the pillar height. The neutron efficiency trend goes in the direction of having small and deep pillars.

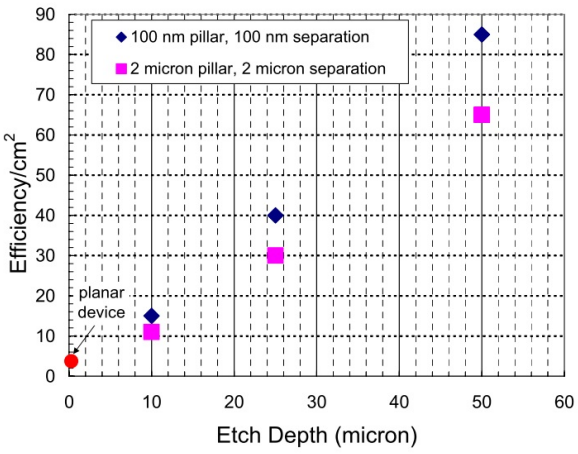

Figure 2.9: Neutron detection efficiency versus cell dimension for pillar covered with ^{10}B [16]

Detectors with pillars of 2μm diameters and a 4 μm pitch etched for only 12 μm have been fabricated with a multi-step process. Using an appropriate mask, the pillar was etched by DRIE (Deep Reactive Ion Etching) with an ICP source, time-multiplexed "Bosch Process" using ions SF_6 for Silicon and C_4F_8 for the passivation. For taller pillars, after DRIE, the detector was immersed in a nitric acid based solution in order to remove the plasma

damaged silicon surface [84]. The etched volume around the pillars should be filled by the neutron reactive material. The process used for the ^{10}B deposition is a chemical deposition with $^{10}B_{10}H_{14}$ (decaborane) as precursor and argon as the carrier gas at 425C. In order to make contacts, aluminium is sputtered on the pillar after that the ^{10}B deposited on the tip of pillar is removed with an etching using electron cyclotron resonance etching (ECR) with a tri-source plasma of $CF_4/H_2/O_2$. Thermal neutron tests under a moderated ^{252}Cf source were performed with an efficiency of ∼7.3% [85] [86]. One issue in 3D neutron detectors is the conformal boron deposition in the interspace between the pillars (or similarly in perforated detector). CVD technique is the most controllable process for boron filling of geometries with relatively high aspect ratio (1:10) [87][88]. Other options, like physical deposition (sputtering or evaporation) are not suitable to this purpose. In particular a low Pressure chemical vapor deposition (LPCVD) technique has been developed for boron coating in high aspect ratio neutron detectors. The LPCVD process was performed with an enriched $^{10}BH_{14}$ gas with a purity of 98% and a Boron enrichment of 99.23%. The deposition was carried out at low pressure (2 mTorr), $^{10}BH_{14}$ was at vapour pressure of $\sim$ 20 Torr at 105C. A heated mass flow controller was used to deliver the precursor with precise flow control and argon gas was used to curry and dilute the precursor. The process was optimized in order to obtain high fill factor by varying four parameters: process pressure, buffer gas flow rate, temperature and process period. The temperature that allowed for a good fill factor for all the different aspect ratio devices analysed was 420C. Figure 2.10 shows the cross sections, for different geometries and two different temperatures, and the fill factor is found to be much higher at low temperature.

The proposed devices were almost completely filled for a process temperature of 420C and a pressure of 50 mTorr[17]. Pillars that make up the

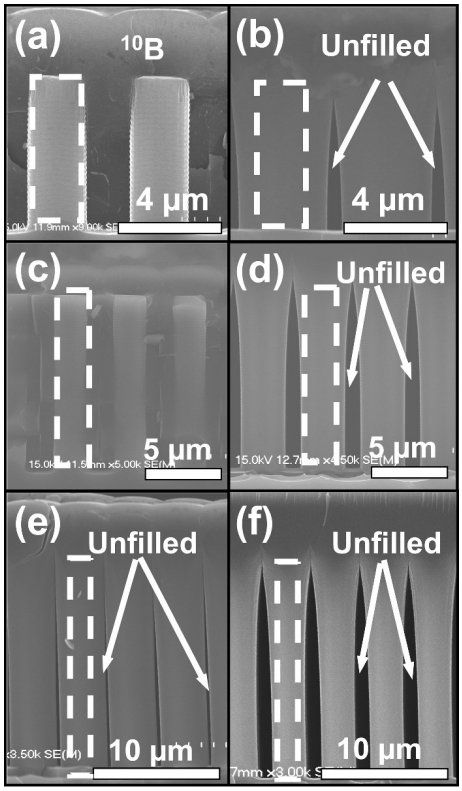

Figure 2.10: Cross sections of different geometries with different aspect ratio on dependence of deposition temperature [17]

sensor should be directly coated with metal in order to make an electrical contact. For the boron removal two different techniques were developed: planarization with photoresist and etch-back and planarization by etch rate matching. Both of them allowed for a good contact to the pillar to apply the bias[89]. The methods use an ECR (Electron Cyclotron Resonance) plasma etching with SF_6 optimized for the boron removal [90]. The internal forces due to the boron deposition were studied with a Raman spectroscopy and used for find a correlation between strain concentrations versus the fracture of micropillar [91]. Varying the depth of the pillars may affect the neutron detection efficiency; with a pillar height of 12 μm an efficiency of $\sim$ 7.3 % was reported [92], whereas with a pillar height of 26 and 50 μm the efficiency was incresead to 22% and 48.5%, respectively [84]. The

gamma-ray discrimination was measured using a high gamma-ray field and it is 8.5×10^5 for a threshold corresponding to a neutron detection efficiency of 38% [93].

2.2.4 Rensselaer Polytechnic Institute

The Rensselaer Polytechnic Institute has been very active in solid state neutron detectors in the past few years with remarkable results. They proposed a high aspect ratio honeycomb geometry using Boron as neutron reactive material. The hexagonal trenches host boron deposited by a LPCVD developed to this purpose. Figure 2.11 shows a sketch of the silicon honeycomb structure where the hexagonal trenches are filled with boron. The 3D fabrication process uses a DRIE masked with photoresist and 300 nm of SiO_2. The junction is obtained during the boron deposition using a LPCVD process. The temperature of deposition changes during the process: at the beginning the process is carried out at 900C for diffusing dopant into silicon and after that the temperature is gradually reduced to 500-600C and a pressure of 300 mTorr for the boron deposition [94]. In the LPCVD the precursor gas was diluted B_2H_6 in H_2 with a flow rate of 50SSCM at 525C [95]. The metal used for the front and back contact was Ti–Al deposited using sputtering. Before the metal deposition it was necessary to remove the excess boron using a RIE plasma etching with SF_6 and O_2. The silicon oxide deposited for the mask definition is used for stopping the etching process and is removed before the metal sputtering.

Monte carlo simulations using GEANT4 were performed to optimize the geometrical dimensions of the structure. Despite the shapes and the geometries are different from those described in section 2.2.2 and reported in [71], simulation results are in good agreement. High efficiency for thermal neutron is possible if the cell is small enough and the trenches occupy most of it. GEANT4 simulations reported in 2.12 show that, for a given

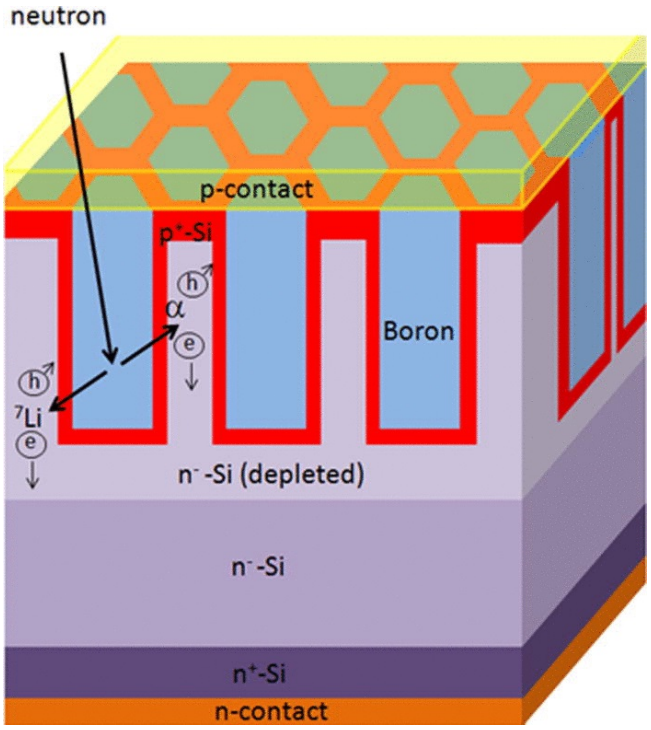

Figure 2.11: Honeycomb structure sketch [18]

combination of ratio between trenches and separation walls, it is possible to reach $\sim 45\%$ for a hole depth of 40μm[18]. Simulations also highlight a sensitivity of the efficiency to the size of the structures [94].

The electrical characteristics are very good: the trenches are doped, thus eliminating surface generation/recombination problems induced by DRIE process, and full depletion is achieved at very low voltage. The first fabrication run used natural boron for filling the trenches. Detectors were tested under perpendicular neutron flux with moderated ^{252}Cf source with an efficiency of 4.5% and a gamma sensitivity of 1.1×10^{-5} [18]. Varying the threshold it was possible to obtain a higher neutron detection efficiency at the expense of gamma discrimination. By replacing natural boron with enriched ^{10}B an efficiency of $\sim 26\%$ was reached [96].

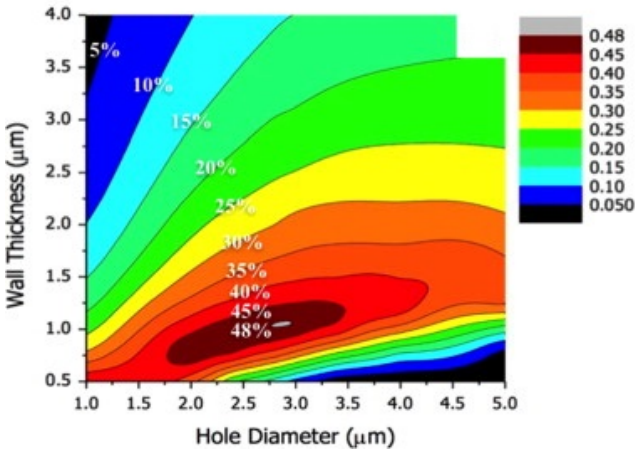

Figure 2.12: Simulated efficiency for parametrized honeycomb geometry [19]

2.2.5 Other groups

The Czech Technical University in Prague has been among the pioneers in semiconductor based neutron detectors. They started by investigating planar sensors covered with ^{6}LiF [97] [61]. More recently, they used silicon detectors coupled with neutron converters for imaging applications by using Medipix read-out chips [98][99][100]. 3D detectors have been also considered and developed in collaboration with Sintef and other institutes. Simulations of cylindrical and square pores have been developed and they predicted an efficiency of 28% and 32% for ^{6}LiF and 20% and 22% for ^{10}B [101] [102]. Another important geometry proposed in collaboration with Sintef was a 3D structure with pyramidal structures filled with TiB_2 and ^{6}LiF [103]. The advantage of this solution is the simplified fabrication process: the pyramidal grooves were obtained by TMAH (tetra-methyl-ammonium hydroxide) wet chemical etching. The etching follows the crystal plane 111 with an angle of 54.6 degrees. The remaining part of the process is the same as for planar detectors. A relative efficiency increase of up to 38% was obtained with respect to standard planar detectors coated with the same neutron reactive layer.

The Instituto de Microelectrónica de Barcelona (IMB-CNM, CSIC) is also involved in this research field. They developed two different 3D detector concepts: classical trenches filled with neutron converter and very thin 3D detector covered by neutron converter but working as planar. Sinusoidal and honeycomb trenches were simulated, fabricated and tested with encouraging results. The converter material was ^{6}LiF and the efficiency was $\sim$ 8.6 % [104]. The concept of ultra-thin 3D detectors is aimed at reduced gamma sensitivity. It is different from the 3D etched detectors used to maximize the surface area of interaction of the converter material with silicon. As well known, the capacitance in a planar sensor is increased as the thickness is decreased, and this is generally an issue for the noise of the electronic read-out. A 3D structure, on the contrary, allows the thickness to be reduced, while still keeping the capacitance at acceptable values. 3D detectors were proposed by S. Parker in 1997 [105] and are currently used in many experiments at Cern (European Organization for Nuclear Research). They will be described in detail in 4.

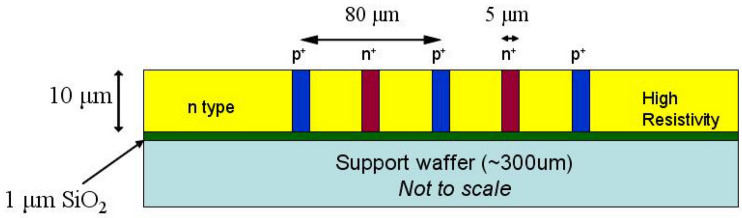

Figure 2.13: Sketch of a 3D ultra-thin detector of neutrons with reduced gamma sensitivity [20]

Figure 2.13 is a sketch of the ultra-thin 3D detector developed, fabricated and tested. The holes in silicon have a diameter of 5μm and are positioned at a distance of 80μm between columns of the same doping type. Holes are not filled with converter material but they behave as Ohmic and junction contacts of the device. The efficiency for different converter materials (^{10}B, ^{10}BC) are in line with standard planar detectors, but the gamma ray

sensitivity is inded very good, of the order of $\sim 10^{-8}$.

2.3 Neutron detector applications

As compared to X-rays, neutron cross section has an opposite trend for different materials (see Fig. 2.14), and this makes them a good candidate to investigate light materials.

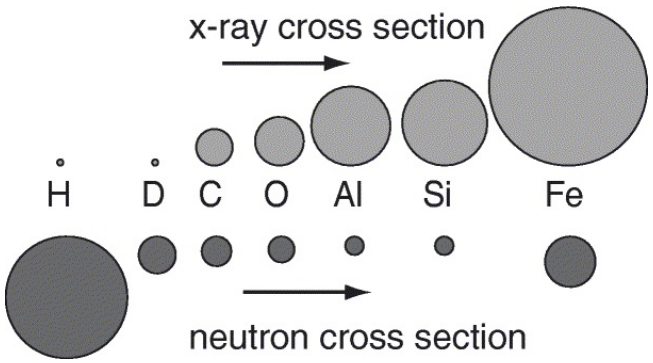

Figure 2.14: Relative cross-sections of various elements for neutrons and X-rays [21]

Attenuation of X-ray increases with the atomic number of the elements and, in imaging applications, there is a very low contrast between light materials and background. In materials rich of water or hydrogen, having a sufficient contrast is very complex, making them impractical for imaging techniques. For this reason neutron tomography finds application in a broad spectrum of fields. As an example, it is possible to apply this technique in archeology for dating and studying historical artworks, in materials science, in fuel cells research, in biological and medical applications, in homeland security and contraband detection. Both 2D and 3D neutron imaging are non-destructive and non-invasive techniques that provide information about the materials structure, texture, phase contrast and composition of the material. From neutron beam attenuation through the matter it is possible to extract the information useful for the neutron radiography. The attenuation coefficient depends on the material characteristics and the

neutron wavelength. Beam absorption and scattering in the analysed object decrease the transmitted beam intensity. This can be used in the analysis of rare artefacts because the information about the material composition can be extracted (each material has a different cross section). This permits to make analysis in materials like bronze where X-rays would not penetrate deeply. The different bronze alloy composition can be used to determine the fabrication period. An example of neutron imaging of archaeological bronzes is shown in Fig. 2.15. It represent a statuette of a small dog with a resolution of approximately 75 μm.

Figure 2.15: Photograph and neutron radiograph of an bronze dog statuette (7.5 cm x 3.5 cm) [22]

The same technique used for archeological studies can be used for imaging of biological samples. The contrast is mainly provided by the scatter with hydrogen atoms [106]. The measurement setup is reported in figure 2.16.

As in the previous case, neutron radiography measures the flux attenuation for absorption and scattering within the sample. Internal cracks in the material can be investigated by direct imaging in metals like iron [107]. The residual strain in materials can be determined through Bragg's law by measuring distances between crystallographic planes of the strained

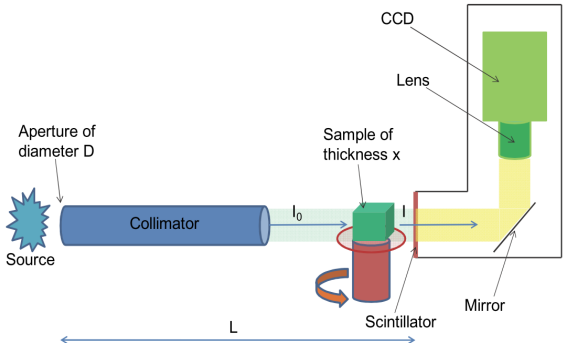

Figure 2.16: Layout of a neutron imaging beamline [23]

sample and a reference [108] Images with high contrast on hydrogen-rich materials allow to make in situ non-destructive analysis of polymer electrolyte membrane hydrogen fuel cell. In this case it is possible to check the functionality of the system during its operation and discovery defects [21].

Another application, where in most cases it is not necessary to have imaging systems, is homeland security, where sensors able to detect materials normally used in nuclear weapons, like plutonium, are extremely important [50].

CHAPTER 3

Neutron detector: design, fabrication and simulation

The neutron detectors designed at the University of Trento were fabricated at FBK (Fondazione Bruno Kessler), Trento. This activity was carried out within the HYDE project (HYbrid for Neutron Detector), that was funded by the Italian National Institute for Nuclear Physics (INFN) through the CSN5. In this project two batches of sensors were fabricated. In the first batch (Hyde 1), a modified 3D-STC (3D Single Type Column) sensor structure [109] was fabricated with the purpose to ease the coupling with different neutron converter materials. Rather than aiming at a high detection efficiency, such a structure should be intended as a test vehicle to carry out experiments useful to investigate the main issues with neutron detection. In the second batch (Hyde 2), optimized sensor geometries have been considered, trying to address the problems that were discovered in the first batch. Since the complex geometrical topography and the non ideal charge collection behaviour of 3D detectors of the first batch made the interpretation of experimental results difficult to be fully understood,

planar detectors were also tested in comparison, that also helped to tune the Geant4 simulations.

3.1 Hyde 1 device description

The Hyde 1 layout contained two different main device types: test structures and detectors. The wafer layout, shown in figure 3.1 is designed to be fabricated on 4 inch wafers with a nominal thickness of 230 μm. Most of the wafer area is covered with detectors (37 devices with 12 different geometries), whereas at the corners are 8 blocks of test structures. A wide safety margin ($\sim$ 1 cm) is left at the wafer edge.

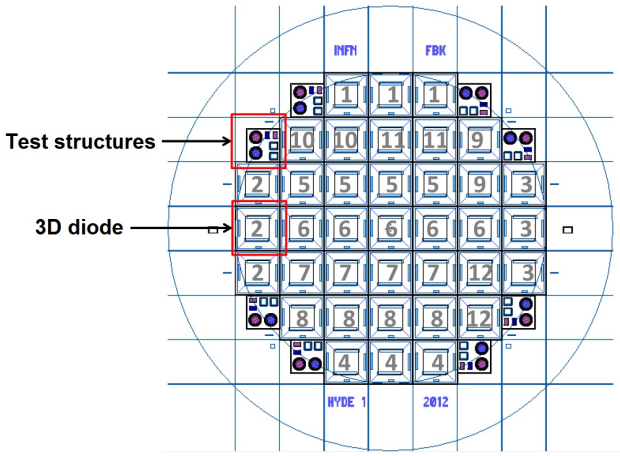

Figure 3.1: Wafer layout of batch Hyde 1

3.1.1 Test structures

The test structures are mainly aimed at monitor the fabrication process quality. They include a planar diode, two coupling capacitors, different resistors, and 3D "basic structures". Figure 3.2A shows the layout of the block of test structures. It has a dimension of $7.5 \times 7.5\ mm^2$. The diode are a made of a circular n^+ implantation on the p substrate, surrounded by a

guard ring. They are used for current-voltage (I-V) and capacitance-voltage (C-V) characterization, from which information about leakage current, carrier lifetimes, breakdown voltage, depletion voltage and substrate doping concentration are obtained. The MOS (Metal Oxide Semiconductor) capacitors are made of a circular metal plate on top of an insulator, consisting of a stack of different oxide layers. Similarly to the diode, a metal guard ring is present (as a parallel MOS). Two additional MOS capacitors made on top of highly doped regions (p^+ and n^+ implantations), referred to as coupling capacitors, allows to extract information on oxide layers of different thicknesses used in the fabrication process. There are two types of resistors of the Van der Pauw type, aimed at measuring the sheet resistance the contact resistance of different doping layers. The 3D "basic structures", shown detail in Fig. 3.2B are the most important since they allow to check the most critical step in the device fabrication. As it will be described in Section 3.1.2, contacts to the trenches from the opposite side are made by using conductive micro holes similar to TSV (Through Silicon Via). Two alternatives were studied for these stuctures with a process split: a) micro holes filled with doped poly silicon and, b) micro holes only doped with phosphorus. 3D basic structures are available as single trenches with two separate contacts, through which a current could be forced, as shown in Fig. 3.2B, and small arrays of the same structures connected in series. These devices allow to measure the contact resistance to the trenches.

3.1.2 Hyde 1 neutron detectors

The considered detectors are essentially diodes aimed at test purposes and not optimized for neutron detection. In fact, in this first batch, in order to ease and speed up the electrical and functional characterization of the detectors, without need for bump-bonding with a read-out chip, all the cavities of the devices are short-circuited together by a metal grid to obtain

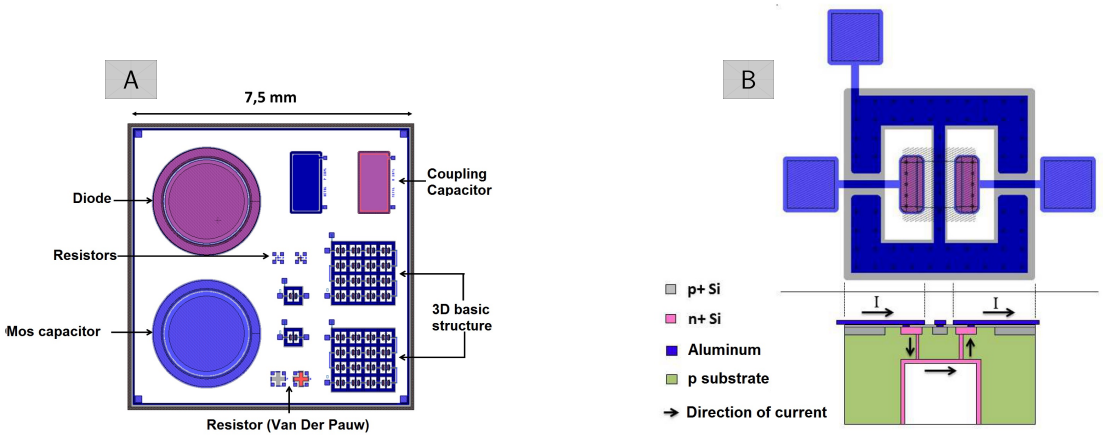

Figure 3.2: A) Test structures cell, and B) a detail of the 3D basic structure.

a diode-like structure. The schematic cross-section of the device is shown in Fig. 3.3A. The cavities are cubic with a size of 200×200×200 μm^3, and are obtained by using Deep Reactive Ion Etching (DRIE). The cavities are doped with a phosphorus diffusion to act as junctions, and are isolated at the Si/SiO_2 interface by using a uniform p-spray implantation.

The planar p^+ electrodes on the wafer side opposite to the cavities are obtained by boron implantation. Both p^+ and n^+ contacts are actually on the same side. This choice was dictated by different reasons: on one hand, after the DRIE etching, due to the severe topography, it would be difficult to perform lithography with good results on the cavity side; on the other hand, having the contacts and the cavities on opposite sides gives more flexibility for the converter deposition and the interconnections. As already mentioned, the developed technology uses narrow via holes (with a nominal diameter of 6 or 8 μm) to contact the cavities from the opposite side. Different geometrical options were considered during the layout design. In particular, the pitch between the cavities (from 300 to 400 μm), the width of the p^+ regions (from 50 to 150 μm) and the via holes size. An example of layout is shown in Fig. 3.3B. The die size 1 cm^2, but the active area is about 0.25 cm^2. Two metal pads for the anode and two for the

cathode (in order to have redundancy) are available to make the electrical connections to the readout system.

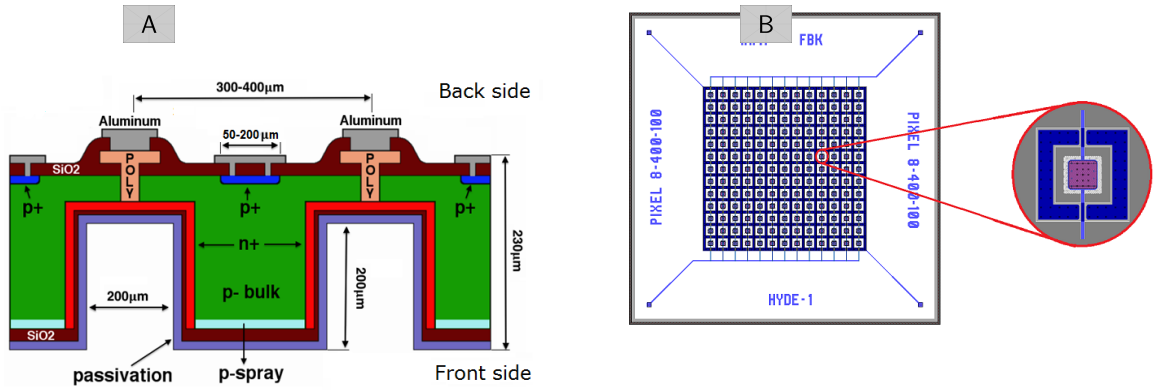

Figure 3.3: A) Schematic cross-section (not to scale), and B) layout of 3D sensor of batch Hyde 1[24]

The advantages achieved by using this technology are mainly:

- the cavities can be filled with converter material without interfering at all with the electrical contacts, i.e., the converter material can be deposited everywhere without need to mask any contact or to later etch the converter;
- in case of deposition of scintillator materials, an external photodetector could be coupled to the sensor for the detection of the emitted light;
- the back side is not affected by the converter deposition and so is completely available for the interconnection with the read-out chip.

3.1.3 Hyde 1 fabrication process

As already mentioned, the process was split in two parts, which are different in many steps: in the first one the n^+ contact to the junction cavity is based

on phosphorus diffusion of the narrow via holes, whereas in the second one the via holes are filled with doped poly-silicon.

Figure 3.4 summarizes the fabricatiob process for the first part:

- implantation of p-spray on the front side, and of p^+ and n^+ contacts on the back side (1);
- etching of trenches, doping by diffusion and deposition of passivation materials on the front side (2);
- etching by DRIE of the connection via holes after the removal of silicon nitride on the back (3);
- doping of via holes, metalization of the contacts and excess oxide removal (4).

In the second process split, the connection between trenches and contacts is realized by doping and poly-silicon filling. The fabrication sequence differs mainly in two steps: I) the n^+ contact region is not implanted, because the contact with the metal is done directly on the poly-silicon layer, and II) after the etching of the via holes there is a deposition of n^+ doped poly-silicon.

A list of all the different geometries of devices is reported in Table 3.1.

Before starting the fabrication of the Hyde 1 batch, many tests were performed for tuning the single steps of the process. In particular, the two most difficult steps are the etching of the trenches and of the via holes. Some results from these tests are shown in Fig. 3.5. In particular, the figure shows: (1) a cross section of the wafer taken with an optical microscope, and (2) highlighting the via holes. Using SEM microscopy it is possible to observe in detail the DRIE etching of the via hole (3) and of the trenches (4). The latter SEM images allow to appreciate the typical scalloping effect typical of DRIE process.

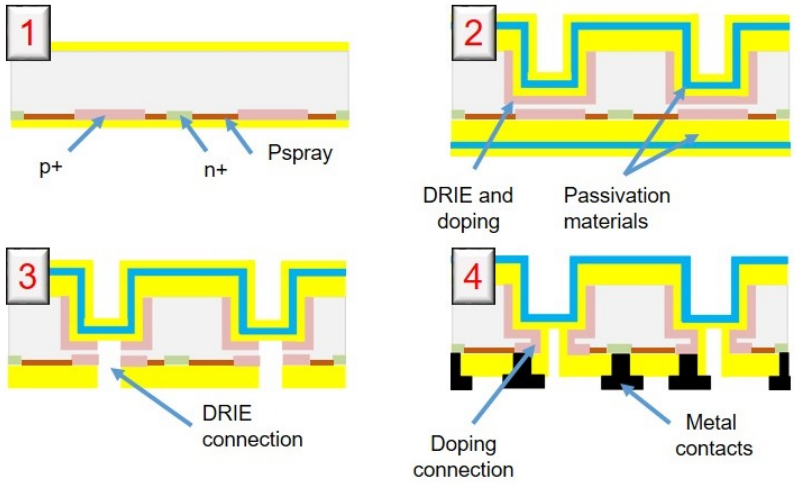

Figure 3.4: Main steps of the Hyde 1 fabrication process

3.1.4 Converter materials used with Hyde 1 sensors

Big trenches like those of Hyde 1 sensors lend themselves to be easily filled with many different materials and using different filling techniques . The materials used as neutron converter were: sub-micrometer particle size of ^{6}LiF, based compounds of polysiloxane containing ^{10}B compounds and thin layers of ^{10}B compounds.

Neutrons imaging and tracking is based on the detection of protons emitted by the converter material. The working principle is based on multiple elastic neutron-proton scattering in organic and plastic scintillator [110]. The converter material considered for the trenches filling of Hyde 1 was Poly (22-25 mol% diphenylsiloxane-co- dimethylsiloxane) (22PDPS) or condensation curing polydimethylsiloxane (PDMS). PDPS has an higher scintillation light yield [111][112] but PDMS is to be preferred because it has an higher hydrogen content (79 mol/l against 71 mol/l for 22PDPS)[113]. The performance with neutrons have reached detection efficiencies as high as 70% in comparison of standard commercial plastic scintillators [114].

This materials can be easily produced using processes at room tempera-

Name	Cavities Pitch	Array dimension	p^+ region width	Via holes size	Multiplicity
400-50-6	400	13x13	50	6	3
400-100-6	400	13x13	100	6	3
400-150-6	400	13x13	150	6	3
400-200-6	400	13x13	200	6	3
400-50-8	400	13x13	50	8	4
400-100-8	400	13x13	100	8	5
400-150-8	400	13x13	150	8	4
400-200-8	400	13x13	200	8	4
300-50-8	300	17x17	50	8	2
300-100-8	300	17x17	100	8	2
350-100-8	350	15x15	100	8	2
350-150-8	350	15x15	150	8	2

Table 3.1: Geometrical details of Hyde 1 detectors

ture. The low viscosity permits to be an option suitable for the trenches filling. The thermal range has a wide range from -60 C up to 200 C and a good transparency even with high radiation doses [115][114].

Table 3.2 resumes all the materials and the techniques used for the deposition of the converters.

The mechanical filling, performed by pressing the ^6LiF powder with average grain size smaller than 1 μm on the trenches, was made at the Czech Technical University in Prague. Figure 3.6A shows the SEM micrograph of the 3D diode filled completely and quite uniformly with ^6LiF.

The PDMS containing 10_{wt}%o-carborane or 30_{wt}%o-carborane was produced by mixing the desired quantities of additives in the resin. In order to pour it into the cavities the PDMS deposited on the front surface of the sensor at low pressure. As soon as it is moved to atmospheric pressure, the difference of pressure pushes the resin into the cavities getting a complete

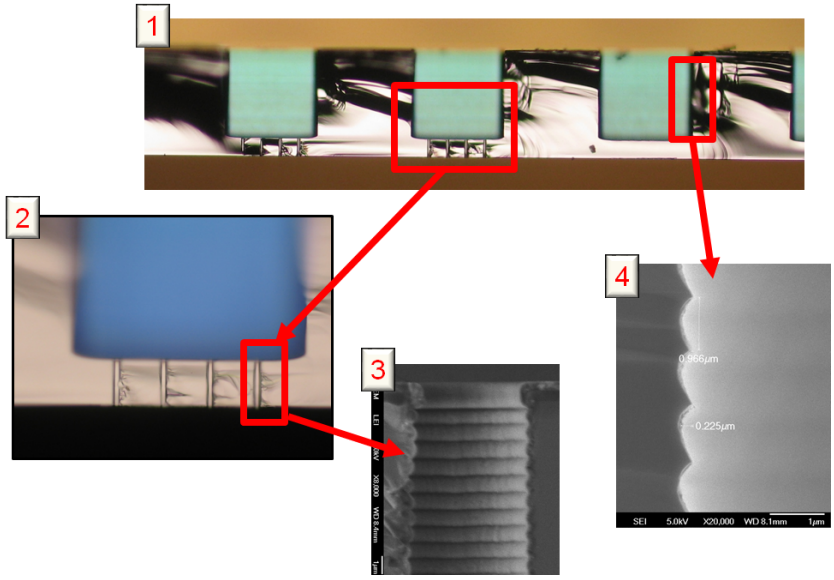

Figure 3.5: Microscopic details of Hyde 1 production

filling. The detector is finally put in a oven at 60C for a couple of hours. Figure 3.6B shows the good adhesion with the walls of the detector and the complete and homogeneous filling.

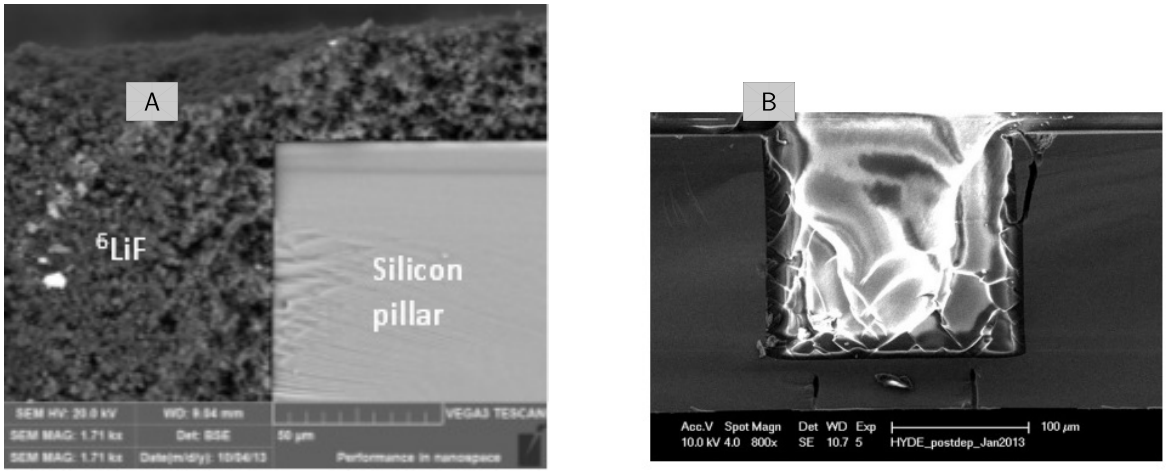

Figure 3.6: A) SEM image of the cross-section of a 3D diode filled with ^6LiF, B) SEM image of the cross-section of a 3D sensor filled with PDMS [25]

Sputtering of a thin layer of $^{10}B_4C$ and ^{10}B were also performed. The resulting thickness for $^{10}B_4C$ was 0.5 μm for 30 min of deposition and 1 μm

Sample	Material	Converter	Deposition tecnique
^{6}LiF	Enriched sub-micrometric ^{6}LiF	^{6}Li	Dry mechanical filling
PDMS carborane	Polydimethylsiloxane doped with 10_{wt}%o-carborane	^{10}B	Polysiloxane resin filling
PDMS ^{10}B	Polydimethylsiloxane doped with 30_{wt}%o-carborane	^{10}B	Polysiloxane resin filling
$^{10}B_4C$ 30 min	Thin enriched $^{10}B_4C$ layer	^{10}B	Sputtering 30 min
^{10}B	Thin enriched metallic ^{10}B layer	^{10}B	Sputtering 1h

Table 3.2: Different depositions on Hyde 1 samples

for 1 h of deposition. A smaller rate of only 0.4 μm per 1h of deposition was obtained for ^{10}B deposition.

3.2 Planar sensor description

Planar sensors, available from previous productions for other purposes, were also used as neutron detectors. A sketch of their cross-section is shown in Fig. 3.7. They were fabricated on Float Zone, p-type substrate, 300 μm thick and with a resistivity higher than 6 k$\Omega \cdot cm$. The active area was 1.71×1.71 mm^2, surrounded by a 100 μm wide guard ring.

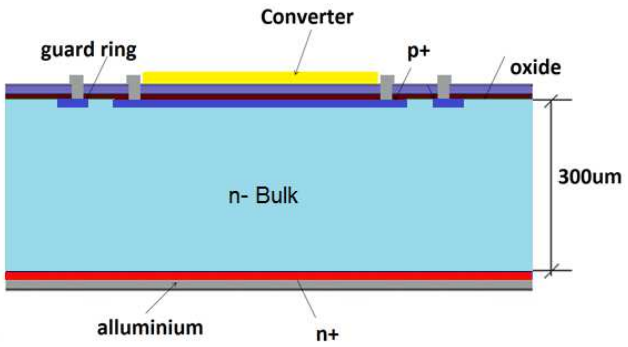

Figure 3.7: Sketch of the planar sensor with sputtered converter on the top (not to scale) [26]

For these devices, the deposition of the converter material had to take into account of the presence, on the front side, of the diode and guard ring contacts. For this reason, in order to prevent short-circuits between contacts and to ease the bonding, a tape mask was applied before sputtering. The masking process had a low reproducibility and there was a small variability ($\sim 10\%$) in the deposited area of converter. The non-optimized deposition process does not allow to achieve a high thickness due to the high mechanical stress on the surface of the detector. By profilometer measurements and SEM images (see e.g. Fig. 3.8) it was possible to estimate the thicknesses. Details for these devices are summarized in Table 3.3.

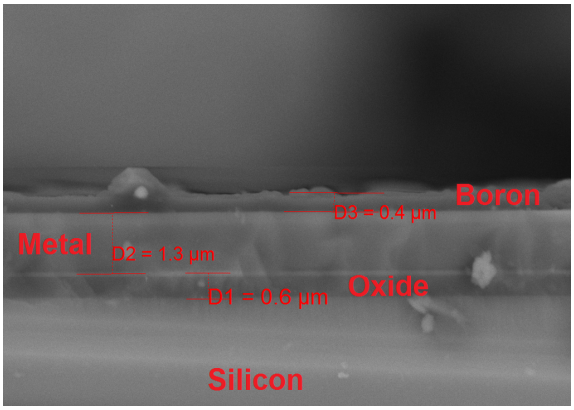

Figure 3.8: A SEM micrograph of a planar sensor with $\simeq$ 500 nm of ^{10}B sputtered on the surface.

Sample	Thickness [μm]	Area [mm^2]
$^{10}B_4C$ 30 min	0.4±0.1	1.45
$^{10}B_4C$ 60 min	1±0.1	1.53
^{10}B	0.5±0.1	1.46

Table 3.3: Planar diode deposition parameters

Figure 3.9 shows two examples of deposition of metallic boron (A) and B_4C (B). The deposition rate of ^{10}B was lower ($\sim 50\%$) but the quality of the deposition was better than for B_4C.

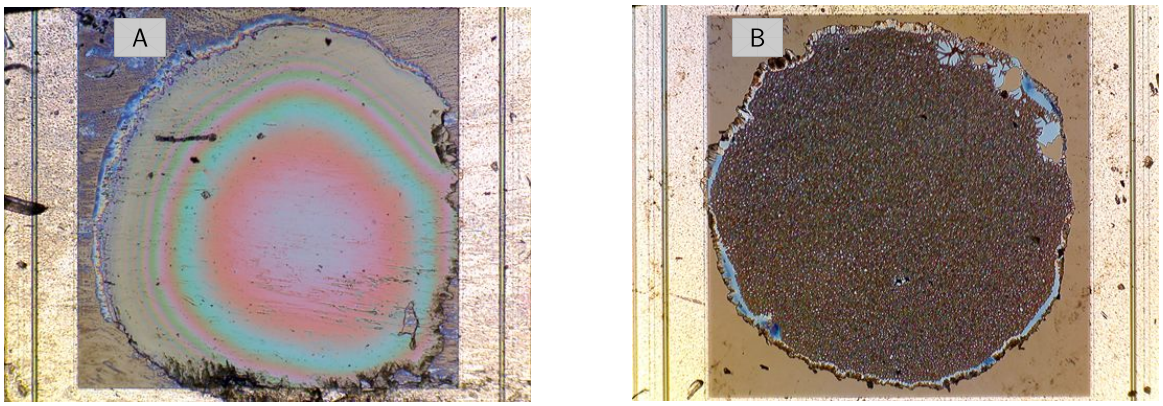

Figure 3.9: A) Optical micrograph of $\simeq$ 500 nm of ^{10}B sputtered on a planar sensor, and B) optical micrograph of $\simeq$ 500 nm of $^{10}B_4C$ sputtered on a planar sensor.

3.3 Hyde 2 device description

The second batch of sensors, called Hyde 2, leveraged the experience acquired with the previous detectors. The main purpose was to have a simplified production process and, at the same time, good results in terms of neutron detection efficiency. In this case the detectors were conceived to be filled with enriched boron as a converter material. In previous works, already reported in chapter 2, different geometries were investigated in order to achieve good efficiency [19][16] [71]. The main conclusion was that, in order to obtain high efficiency, small dimensions should be used for elementary cells. The new design, assisted with Monte Carlo simulation, followed this basic rule for the definition of the cell. The choice to use boron is justified by the small range of reaction products that can be useful in imaging applications. The drawback of this approach is the difficulty to fill the small trenches with neutron reactive material. The Hyde 2 wafer layout, shown in Fig. 3.10, is composed of three parts. Most of the wafer area (5×6=30 devices at the center of the wafer) is devoted to pixelated sensors compatible with the readout chips of the Medipix/Timepix family [99]. All around these sensors are 50 smaller devices (diode detectors) and 10 blocks of test

structures. Two different diode topologies were designed: the ”diode-like” structures are composed by an array (128×128) of short-circuited pixels, whereas the ”big diode” has a single, uniform junction implantation on the back side. The Hyde 2 batch was fabricated on 6 inch wafers with a nominal thickness of 275 μm. Also in this case the area close the wafer border was not left empty because of the low uniformity of processes in this peripheral region.

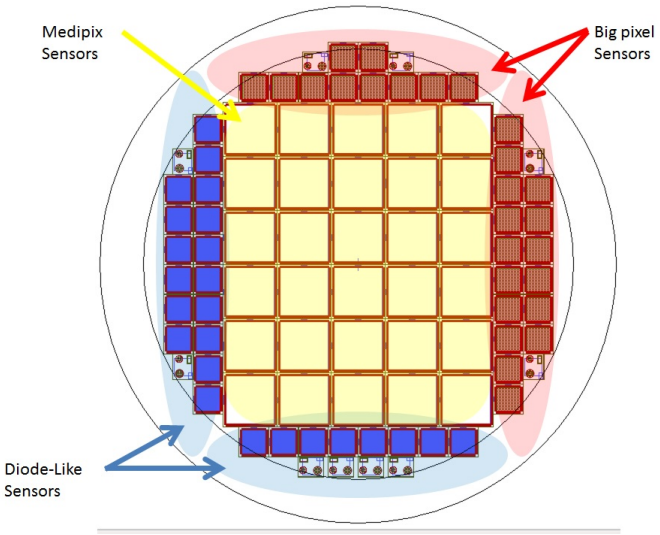

Figure 3.10: Hyde 2 Layout

3.3.1 Test structures

Also in this case, test structures were included to check the quality of the production process. They include a planar diode, a MOS capacitor, different resistors, a gated diode, a NMOS transistor and a coupling capacitor. The layout of the block of test structures is shown in Fig. 3.11. Compared to the Hyde 1 layout, in this case there is a gated diode that is useful to measure the surface generation/recombination velocity [116]. The electrical properties of this batch of devices were good enough and only a few test structures were measured.

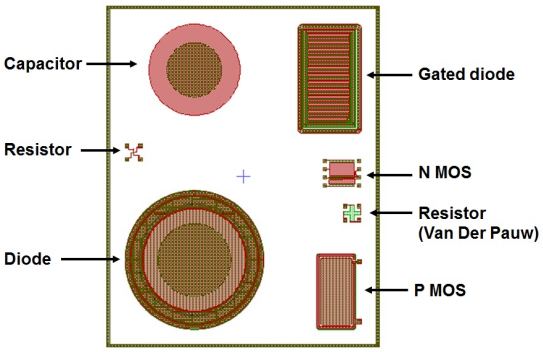

Figure 3.11: Test structures of Hyde 2

3.3.2 Hyde 2 neutron detectors

The neutron detectors, as already mentioned, were composed of pixelated sensors compatible with the Medipix front-end, as well as "diode-like"/"big diode" detectors. The cross section of the device, with the main geometrical dimensions highlighted, is reported in Fig. 3.12. Looking at the dimensions of the trenches and of the separation walls in between, it is possible to immediately note a huge reduction as compared to the previous batch Hyde 1. The mechanical stress caused by the different thermal expansion during the boron deposition can severely damage the narrow walls between the trenches. For this reason the chosen design was a web structure. Medipix detectors have an overall size of about 1.5×1.5 cm^2, whereas the diode size is about 0.7×0.7 cm^2. The pixel pitch is 55×55 μm^2. The cavities are etched by DRIE.

On the etched side (front), only at the surface, is a thin p^+ Ohmic implantation and a layer of aluminium that should be contacted for applying the bias. To minimize the dead layer and simplify the fabrication process, the walls of the etched trenches are not doped, but a very thin layer of Al_2O_3 is deposited as a passivation. Nanolayers synthesized by atomic layer deposition (ALD) emerged as a passivation solution of solar cells [46]. The passivation property of Al_2O_3 were already used in the end of 80' by

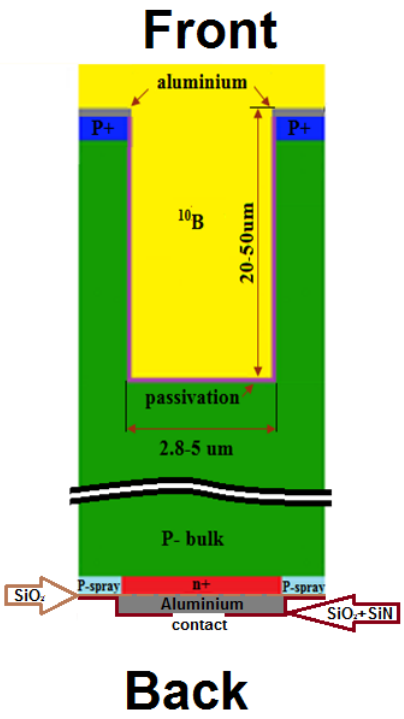

Figure 3.12: Cross-section of the Hyde 2 detector (not to scale) [27]

Hezel and Jaeger [117]. ALD technique has revived this technology for passivating p-type substrates in solar cells [118]. In radiation detectors it was successfully used in slim edge detectors [119]. In this application was developed a technique called Scribe-Cleave-Passivate (SCP) that consist in the wafer cleaving (compared other techniques as e.g. dicing saw the amount of defects is lower) and deposit, at low temperature alumina. The results in the charge collection shown no deterioration of the efficiency near the edge.

On the bottom side are the junctions obtained by n^+ implantation and arranged as pixels. The surface isolation between pixel is obtained by an uniform p-spray implant. Each pixel is an elementary block and, as anticipated, has a web structure as shown in Fig. 3.13A. Different sizes for the cavities and the walls in between them were considered in order to investigate the impact of different combinations of dimensions on the

detection efficiency.

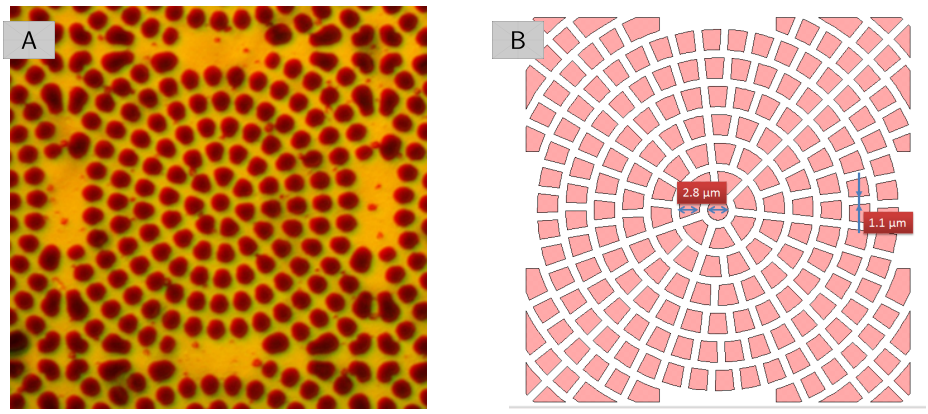

Figure 3.13: A) Optical micrograph of a detail on the perforated side, and B) mask layout of single pixel.

The key factor to obtain high efficiency in neutron detection is the geometrical dimension of the cavities. In the process flow it corresponds to the most difficult part and for this reason many etching tests were performed in order to define the maximum etching depth which does not affect the quality of the walls. In fact, an increase of the etching time can damage the walls close to the surface due the difficulty to dissipate heat. From the test results the best trade-off was found to be an etching depth between 20 and 30 μm.

On the layout of each device (see e.g. Fig. 3.14) are reported some metal labels corresponding to the cavities and of the walls. For example, in this case, the writing identifies a ”diode-like” detector with dimensions of 2.8-1.1. The dimensions are highlighted in the mask layout of a single pixel shown in Fig. 3.13B: The first number, in this case 2.8, represents the diameter of the central hole and the size of the trenches, whereas the second number, in this case 1.1, is the size of the wall.

Figure 3.15 shows a SEM image relevant to an etching test with a trench depth of 27.5 μm, where the presence of defects, visible as roughness close to the surface, can be observed. Lower cavity depths tend to extinguish

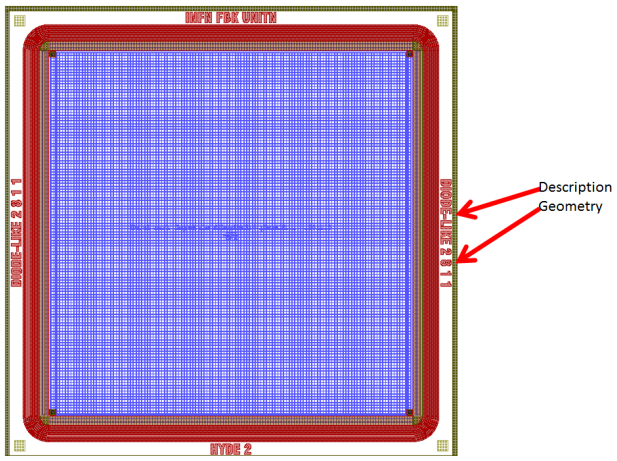

Figure 3.14: Layout of a ”diode-like” detector

completely this effect.

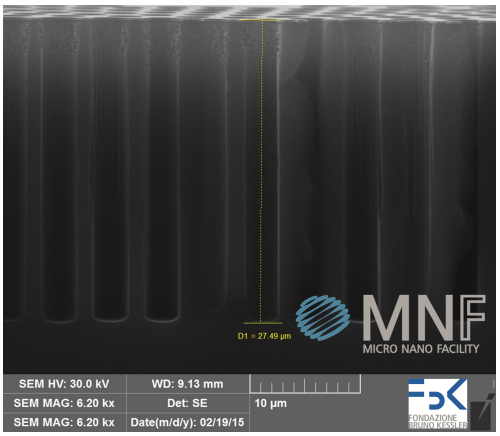

Figure 3.15: SEM micrograph of test cavities etched by DRIE [28]

3.3.3 Hyde 2 fabrication process

The fabrication process of Hyde 2 devices is essentially a standard planar process with the addition of the trench etching on the front side. Two different productions were carried out at FBK because in the first batch there was a problem with the wafer bowing which prevented the sensors with the smallest cavities to be obtained. In the second batch, the lithography of the trench geometries was performed with a stepper.

Figure 3.16 summarizes the fabrication process:

- implantation of p-spray and n^+ regions on the back side and uniform implantation of p^+ region on the front side (1);
- deposition of the metal on both sides and patterning on the back side (2);
- etching of the trenches on the front side (3);
- trench passivation with alumina on the front side (4).

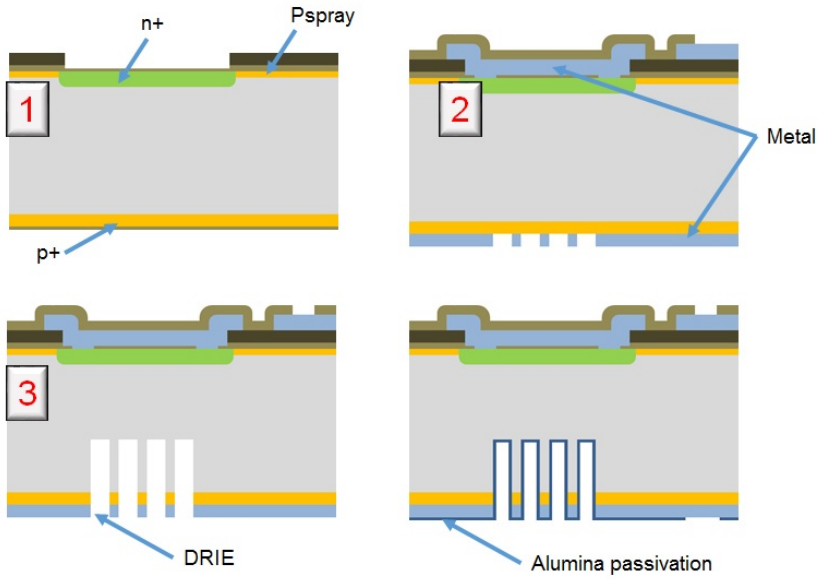

Figure 3.16: Main steps of the Hyde 2 fabrication process

A list of all the different device geometries is reported in Table 3.4.

Despite the preliminary tests were successful, during the device processing it was not possible to reproduce the results due to several accidents. In the first batch, the main problem was the large wafer bowing caused by the surface stresses from different materials, which were not properly taken into account. Due to this reason, the quality of the mask aligner lithography was not so good and the most important device geometry (i.e., the one

Geometry	diode-like	Big diode	Medipix
planar	2	2	2
2.8 1	3	3	5
3 1.5	3	3	4
4.5 2	3	3	3
4.5 2.5	3	3	3
4.5 3	2	3	3
5 3.5	2	3	3
5 5	2	2	2
honey	2	2	3
honey2	2	2	2

Table 3.4: Geometrical details of Hyde 2 detectors

with the smallest cavities) could not be properly defined. However, the characteristics of the other devices (including the trench passivation) were good enough to use them for measurements.

The stepper lithography is inherently much better than the mask aligner, and more tolerant to wafer bowing. However, in the first batch it was not possible to use the stepper because the alignment marks it needs were not available on the wafers. The second batch was conceived to be fabricated by using the stepper, but the alignment marks were not properly defined on all wafers, so that only one wafer could be fully processed, which did not include all the possible geometries. Moreover, on this wafer, the alumina deposition process was not able to reproduce the previous results in terms of charge density, thus compromising the electrical properties of the detector.

3.3.4 Converter materials used with Hyde 2 sensors

Filling Hyde 2 sensors with a neutron converter material represents a big issue due the very small dimensions of the trenches. Different solutions were considered and tested in collaboration with partner laboratories within the network of scientific collaborations of the University of Trento. Test

structures with etched cavities were tested with three different technologies:

- Direct current magnetron sputtering (DCMS)
- High-power impulse magnetron sputtering (HiPIMS)
- Low pressure chemical vapor deposition (LPCVD)

The sample depositions using DCMS and HiPIMS, suitable to deposit $^{10}B_C$, were performed at Linköping University (Sweden) in collaboration with the European Spallation Source (ESS). Different tests were performed by changing the applied bias for the process and the temperature of the substrate. The SEM image in Fig. 3.17A shows the best result obtained by using the DCMS process with no applied bias at a temperature of 350 C for the substrate. Figure 3.17B shows the best result obtained by using the HiPIMS process with 150 V bias voltage at a temperature of 430 C for the substrate. In the former case the $^{10}B_C$ is deposited only on the surface of the detector and does not enter the trenches. In the latter case, the situation is much better because about half of the trenches is filled.

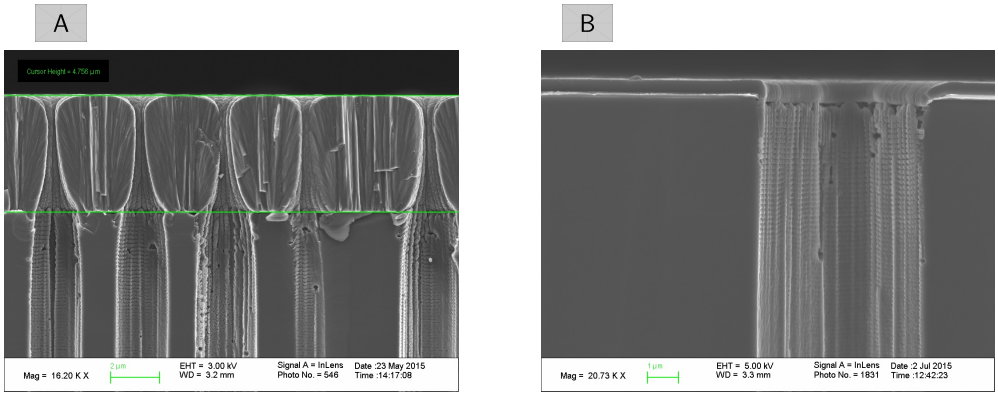

Figure 3.17: $^{10}B_C$ deposition tests on Hyde 2 structures with different techniques: A) DCMS, and B) HiPIMS.

LPCVD deposition technique was tested at the Lawrence Livermore National Laboratory (LLNL) in the USA. Figure 3.18 shows an example of ^{10}B filling performed using the following recipe:

- Furnace temperature: 285 C
- substrate temperature 340 C
- 10 mTorr base pressure, 70 mTorr background (Ar only) and 160-180 mTorr operating pressure (Ar + $B_{10}H_{14}$)
- 2.8 sccm Ar carrier gas
- 120 minute deposition

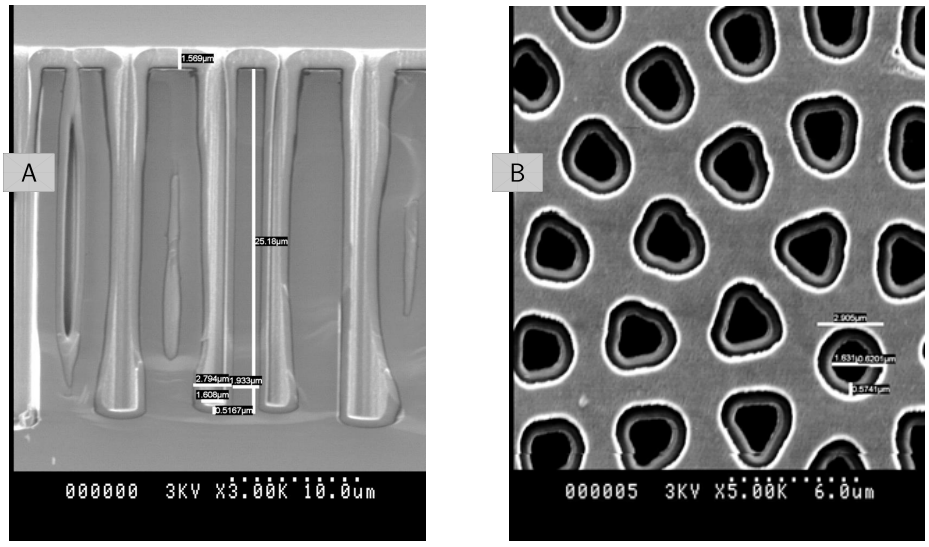

Figure 3.18: Deposition using LPCVD at LLNL: A) SEM image of the trenches, and B) front view of the sample after ERC etching

Boron is an electrical insulator, so it should be removed from the sensor surface in order to make a contact with the metal. To this purpose, Electron Cyclotron Resonance (ERC) etching was used and the results are reported in figure 3.18B.

Despite these encouraging results, the first ^{10}B deposition at LLNL on real detectors has failed because boron went accidentally on the back side of the sensors, making damage to the surface. Figure 3.19 shows such an effect on the passivated surface after the boron deposition.

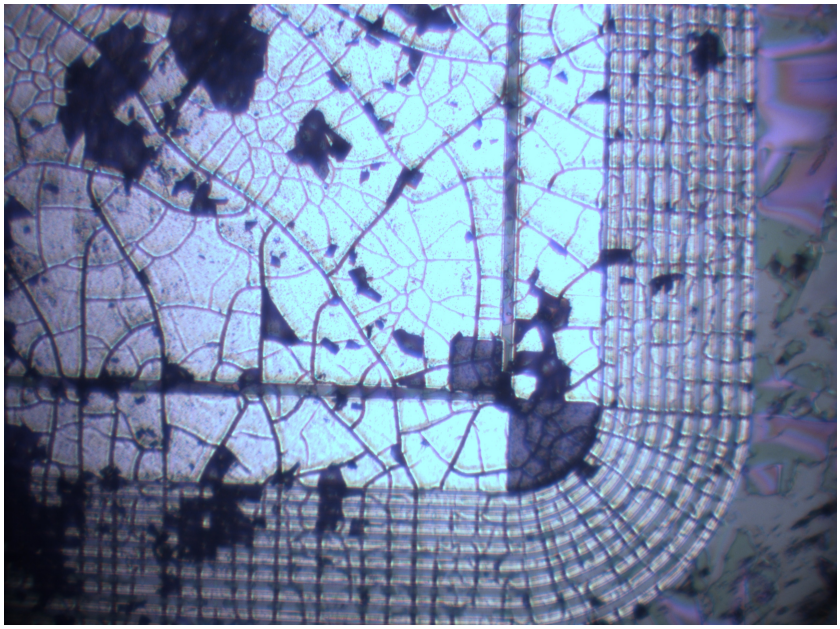

Figure 3.19: Surface damage after accidental boron deposition on the back side

In order to solve this problem, a high temperature compliant adhesive tape was used to protect the back side surface as well as the contacts on the front side. Using this approach it is not necessary to remove by ERC the boron deposited on the surface (and consequently on the contact) of the front side. In the future another option that could be tried for boron deposition is the ALD process reported in [120].

3.4 Sensor assembly

The functional tests with alpha particles, gamma rays and neutrons cannot be performed on a die. In order to be tested, sensors need to be packaged. Special PCB supports were purposely designed. A conductive bi-component glue with silver particles was used for the assembling of the detectors with PCB. The front side of the sensors was contacted through the glue to the board, while on the back side the connections were made by wire bonding between the contacts and the gold plated pads present on the PCB. Figure

3.20 reports the PCBs used for the Hyde detectors.

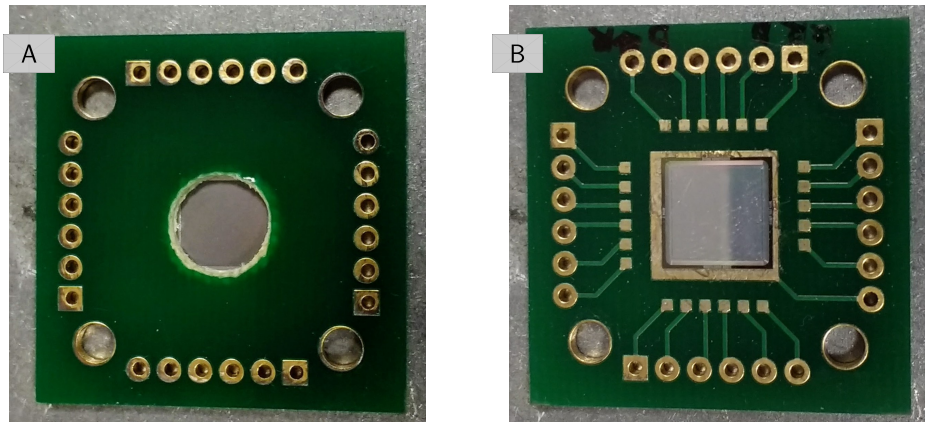

Figure 3.20: PCBs used for Hyde detector testing

It was decided that any contact should be avoided between the converter material and the big metal pad of the PCB where the detector is glued. The reason for this choice is twofold: I) in Hyde 1 sensors, the LiF and the PDMS depositions were made after the packaging, and II) the difference of thickness between the detector regions (coated with the converter and uncoated) could spoil the electrical contact. For these reasons the PCB was drilled with a hole of diameter of 7-8 mm so as to leave open the active area of the detector and connect with the glue only the periphery where the contacts are present.

3.5 Simulations

Different types of simulations were performed in order to predict and understand the behaviour of the detectors: Monte Carlo Simulations and numerical device simulations using Synopsys TCAD tools [121]. TCAD simulations will be described in parallel with the experimental results as an aid to their interpretation. The tools used for Monte Carlo simulations were the toolkit Geant4 [122] [123] and the already mentioned SRIM. Monte Carlo simulations are based on a stochastic mathematical technique based

on the use of sequences of random numbers and probability. The Geant4 simulations were performed by following the procedure described hereafter: I) definition of geometries and materials, II) simulation of one million of thermal neutrons (0.025 eV) particles, and III) analysis of the results. The geometries were directly imported from the CAD model by using the CAD interface for Geant4 described in [124]. The neutron flux was perpendicular to the detector surface with a uniform spatial distribution along the x-y axes. The converter materials considered, corresponding to the depositions on real samples, were:

- ^{6}LiF with enriched ^{6}Li and ^{19}F with a density = 2.64 g/cm^3 for the Hyde 1 devices

- $^{10}B_4C$ composed of ^{10}B at 99% and ^{11}B at 1% and ^{12}C at 100% with a density of 2.52 g/cm^3 for the planar detectors coated with boron carbide

- ^{10}B with enriched B at 99% and ^{11}B at 1% with a density of 2.46 g/cm^3 for the boron converter deposited on the planar and Hyde 2 detectors

The simulations were initially carried out with neutrons impinging from the front side of the detector and then were repeated with neutrons impinging from the back side. The physical model, appropriate for this simulation, has been the QGSP_BERT_HP, using the neutron cross section contained in the GDML library. The efficiency is calculated as the ratio between the number of events that released energy in silicon and the number of neutrons. The energy released from gamma rays is not considered in the calculation of efficiency and a settable threshold of minimum energy released was considered.

3.5.1 Geant4 simulation of Hyde 1 devices

The trenches of Hyde 1 devices were completely filled with ^6LiF, with an additional layer of the same covering all the detector surface with a thickness of 20 μm. Figure 3.21 shows the simulated spectra for neutrons impinging from the front and the back sides of the detector. Due to the not optimized thickness of the converter layer the back side illumination gives better results (the simulated efficiency was, with a threshold of 50 keV, 11.86% for the back side illumination and 8.90% for the front side illumination). Due to the large size of the cavities and their cubic shape, the probability to detect both reaction products is very low, as can be seen from the tails of the spectra.

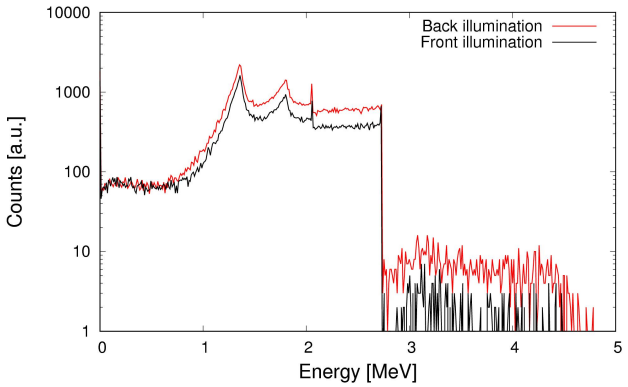

Figure 3.21: Geant4 simulation of Hyde 1 devices

3.5.2 Geant 4 simulation of Planar detectors

This simulation is of particular interest because it can be compared directly with data available from literature. The efficiency results, reported in figure 3.22, are referred to a million of thermal neutrons with a threshold of 50 keV. The converter material had an uniform thickness along the surface.

The efficiency is almost the same for front and back side neutron illumi-

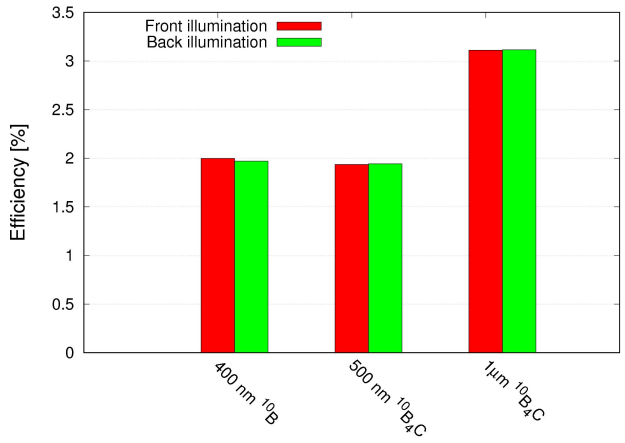

Figure 3.22: Comparison of simulated efficiencies for different planar detectors

nation. This behaviour is the expected one because of the relatively thin thickness of the converter material. The results are in very good agreement with both calculated and measured data, thus confirming the significance of the simulation also for the 3D detector.

3.5.3 Geant4 simulation of Hyde 2 devices

The proposed geometries for the second batch of neutron detectors were also simulated. These geometries are very complex to be designed using only Geant4, in order to maintain the volume of the trenches close to the volume of the central hole. This is the main reason why it was necessary to import the geometries from the CAD drawings. The deposited thickness of ^{10}B is only 1 μm. For this reason, a complex geometry able to cover silicon with a uniform converter layer was created. The simulated trenches depth was, according the fabrication process issues, 25 μm. The spectra for all the proposed geometries for front side and back side illuminations are shown in figures 3.23A and 3.23B, respectively.

The estimated efficiency, also in this case considering a threshold energy of 50 keV, is strongly dependent of the trenches and separation walls volume. The results for all the geometries and for both front and back side

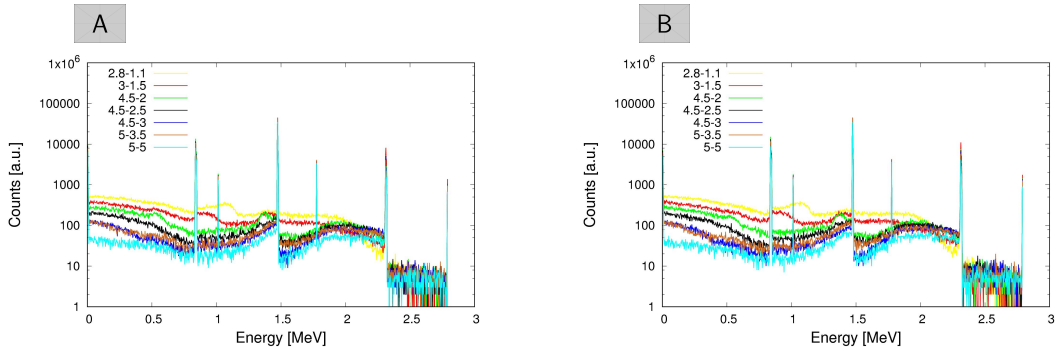

Figure 3.23: Geant4 simulation of Hyde 2 devices: front side illumination, and B) back side illumination.

illumination are summarized in figure 3.24. The importance of using small dimensions for the cavities and the walls is evident, with efficiency values decreasing from ∼30% to ∼12% as the sizes are increased from the smallest ones to the largest ones.

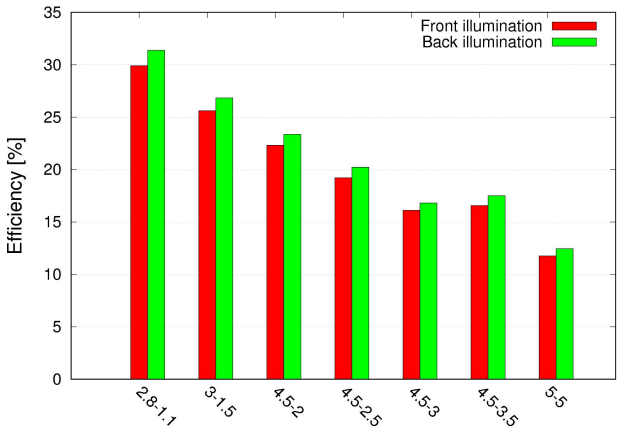

Figure 3.24: Comparison of simulated efficiency for the proposed Hyde 2 devices of different geometries

CHAPTER 4

Experimental results of Hyde detectors

A full characterization has been performed for 3D and planar detector productions. The electrical and functional tests have been performed at wafer level using probe stations at FBK, and, after packaging, in the "Electronics and Embedded Systems Laboratory" at the University of Trento. X-ray scans were performed at the Diamond light source in Didcot (United Kingdom).

4.1 Electrical characterization

The electrical characterization provides important information about the sensor behaviour (e.g., substrate doping concentration, depletion voltage, leakage current, breakdown voltage). Process problems, like those related to low level of charge in the alumina passivation layer, can be highlighted by anomalies in the curves. The two main types of measurements are the current-voltage (I-V) and the capacitance-voltage (C-V) tests.

4.1.1 Electrical characterization of Hyde 1 devices

The first generation of neutron detectors were electrically fully tested. The first measurements were performed at wafer level to check two main aspects: the quality of the process and the electrical contacts. All wafers of the batch, made with different process splits (i.e., with poly-silicon via filling and with phosphorus diffusion), were tested. The I-V measurements on wafer were performed by using a manual probe station connected to a Semiconductor Parameter Analyser HP 4156A. In figure 4.1 are reported the I-V characteristics for a selected part of the devices representative of all the designed geometries. The leakage current is quite good, with values of a few nA, and in most cases the breakdown voltage is close to 60 V, with few exceptions due to defects.

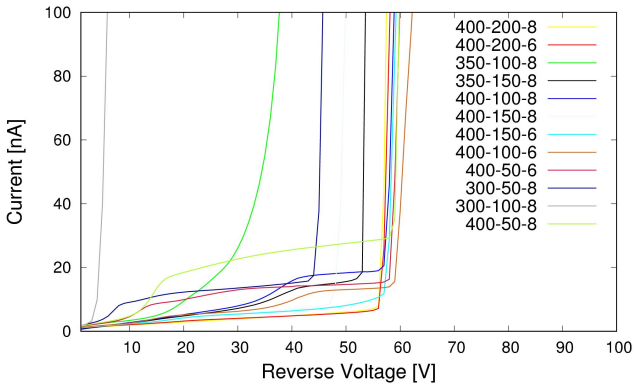

Figure 4.1: I-V characteristics of selected devices of different geometries from Hyde 1 batch

C-V measurements allow to obtain information about the depletion in the detector. A full characterization was performed for all the devices showing good I-V curves. An example of C-V curve for each considered geometry is reported in figure 4.2. All curves show the expected decreasing trend as the reverse voltage is increased, although the complex 3D structure of the devices make the very shapes of the curves differ from those of a

planar diode. Both I-V curves and C-V curves, in particular for geometries where the p^+ Ohmic contact dimension is small, show a sudden change of slope of the characteristics. The voltage at which these current/capacitance "steps" are observed decrease with the p^+ Ohmic contact dimension.

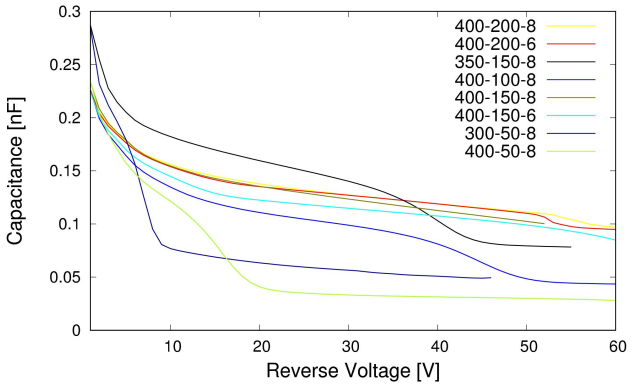

Figure 4.2: C-V characteristics of selected devices of different geometries from Hyde 1 batch

Such a behaviour suggests how the depletion of the sensor volume develops in the detector. At first the depletion region spreads in the interspace in between trenches, whereas, only at higher voltages , corresponding to the observed steps in the I-V and C-V characteristics, the space between the trenches along the diagonal starts to deplete. Further insight into this behaviour can be obtained using TCAD simulations. Static simulations were carried out with the aim of studying the depletion voltage, the electric field distribution, and the breakdown voltage. The computational time for large and complex structures is a critical issue. The choice of the simulation domain can take advantage of the device symmetry, so that for I-V and C-V simulations a quarter of a pixel was good enough. The simulated structure is shown in figure 4.3. It refers to the geometry (400-100-8) that was chosen as a representative case for understanding most of the device features.

The simulated I-V and C-V curves of fig. 4.4 are in quite a good agreement

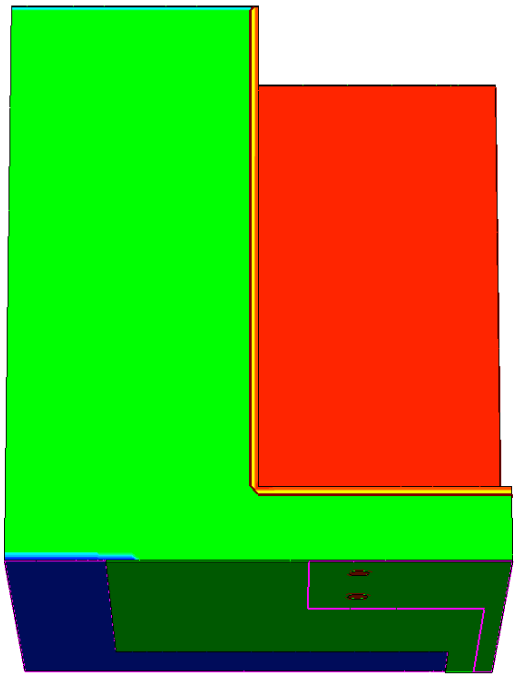

Figure 4.3: Hyde 1: simulation domain for static simulations

with the experimental ones shown in figure 4.1 and 4.2. In particular, the above mentioned step is clearly visible in the C-V curve, although at a lower voltage, and is also present in the I-V curve at about 40 V, albeit not so evident. The breakdown voltage at about 55 V is accurately predicted. The quantitative differences between simulation results and experimental data are probably related to the simplifications introduced in the simulation domain with respect to the real 3D structure.

The simulation is also useful to investigate the depletion behaviour. Figure 4.5 shows the electric field and the depletion volume at different bias voltages of 9, 15, 21 and 39 V. The depletion volume is represented by the white line and it confirms the predicted depletion dynamics, that starts from the volume between the trenches and then extends to the diagonal region between the trenches.

Test structures were also measured in order to check the quality of the

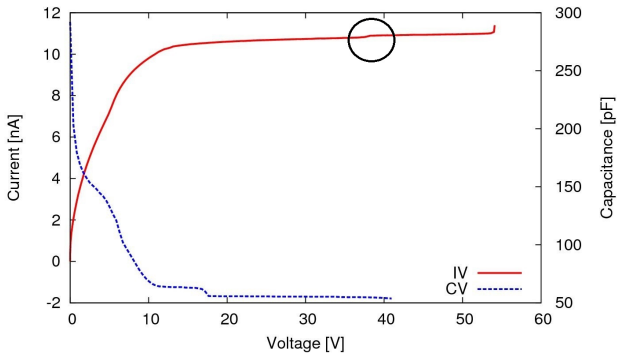

Figure 4.4: Simulated I-V and C-V curves for Hyde 1 device of (400-100-8) geometry

contacts. A total resistance of ∼200 Ω was measured on the contact chain structure, corresponding to a specific resistance of only a few Ω per contact, that is good enough.

Few samples were bonded as described in section 3.4 and the I-V characteristics did not change significantly after the cutting process and the packaging.

4.1.2 Electrical characterization for planar sensors

The planar detectors had good electrical performance, with leakage currents of a few nA and breakdown voltages higher than 200 V. I-V and C-V measurements are shown in fig. 4.6. The full depletion voltage is ∼ 20 V and the sensor capacitance at full depletion is ∼ 0.6pF.

4.1.3 Electrical characterization for Hyde 2

Also devices from the Hyde 2 batch were tested mainly with I-V and C-V measurements. Moreover, additional tests were performed to characterize the alumina layer used for the trench passivation. The measurements were performed only on diodes, not involving the pixel detectors. The two wafers available to be measured were measured three times: before ALD of deposition of alumina, immediately after the deposition and after

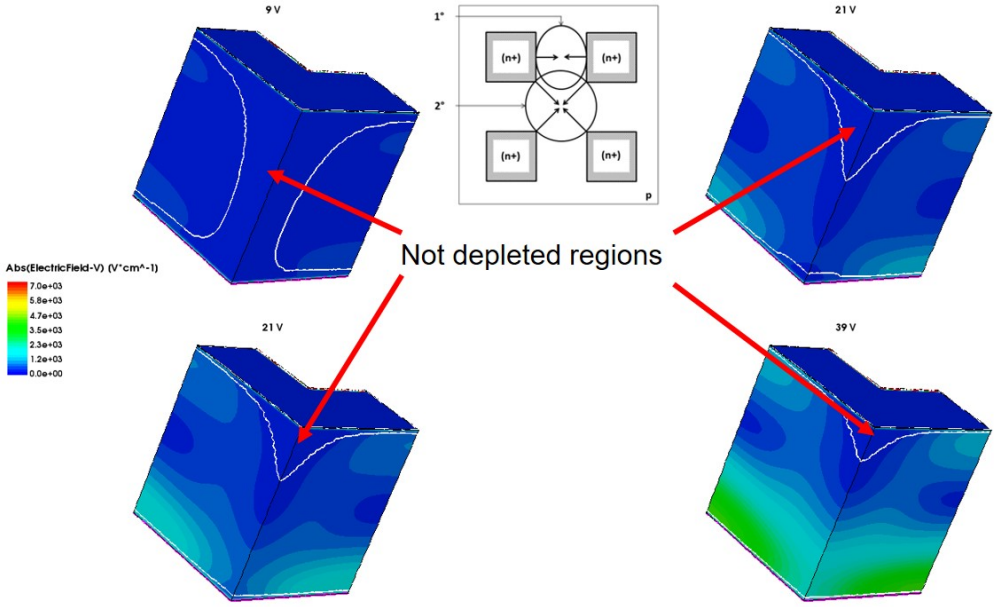

Figure 4.5: The dynamics of depletion volume in Hyde 1 devices.

the Al_2O_3 annealing. The purpose of this measurements was multiple: to check the integrity of the devices and evaluate the quality of the fabrication process, to evaluate the passivation quality of the alumina before and after a thermal cycle of annealing. Figure 4.7 reports a selection of I-V curves for the different geometries before the deposition of the alumina. The measured curves are almost independent of the geometry, the only significant difference being the voltage at which the leakage currents shows a

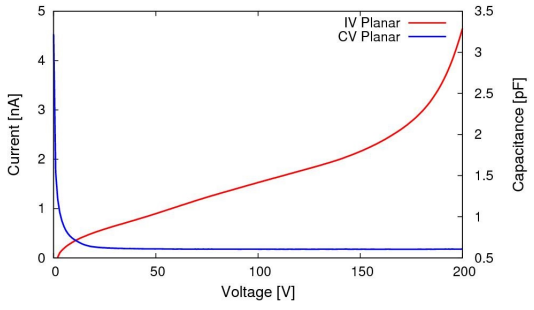

Figure 4.6: Measured I-V and C-V curves for planar sensors

sudden increase: at ∼80-90V for the big diode and ∼100-110V for the diode-like design. This difference is compatible with the larger depletion voltage of diode-like devices due to the junction segmentation, suggesting that the current increase is to be ascribed to the defects at the non passivated trenches. In comparison, the planar device (i.e., without trenches) does not show any current increase.

Also devices where lithography was not good enough to properly define the trench geometries were electrically tested and the current behaviour is comparable with the other devices. A part from the problems in the mask alignment, the process yield very good ∼ 100%.

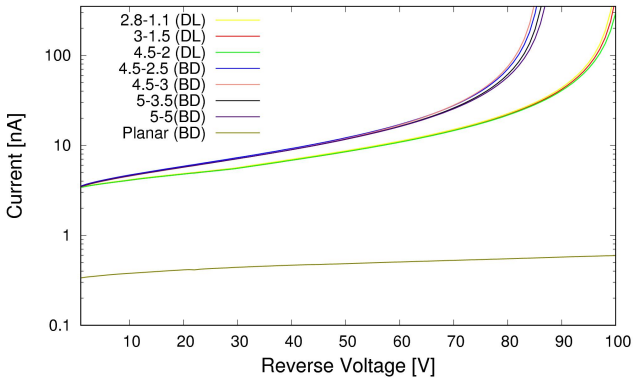

Figure 4.7: I-V characteristics of selected devices of different geometries from Hyde 2 batch

Immediately after the Al_2O_3 deposition, the measured I-V curves do not change significantly and the currents still exhibit a sharp increase at large voltage. After the Al_2O_3 annealing, the measured I-V curves change significantly, as shown in Fig. 4.8. The currents levels are very similar to planar detectors and do not exhibit an increase at large voltage.

TCAD simulations faithfully reproduce the measurements helping to understand the device behaviour in detail. The pixel geometry does not have any symmetry and for this reason the simulation was performed with a domain corresponding to an entire pixel (with geometry 2.8-1.1) in three

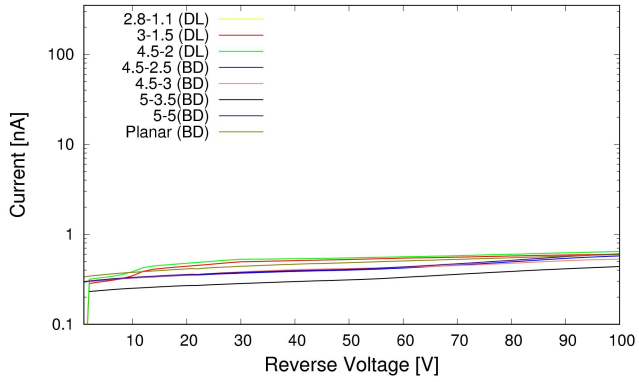

Figure 4.8: I-V characteristics of the same devices as in Fig. 4.7 remeasured after the Al_2O_3 deposition

dimensions. The geometry was designed using a commercial CAD software tool and the design was imported in TCAD as $*.sat$ model. Figure 4.9 reports the domain used for the static simulations. Since the software does not include alumina among available materials, in the simulations the passivation layer was modelled as silicon oxide with a different dielectric constant (3.9 instead of $\sim$ 7.5) and a negative fixed charge density. At the interface between alumina and silicon, i.e., at the surface of the trenches walls, surface recombination was activated with different values of the velocity (s_0), in order to mimic the damage created by the DRIE etching.

The simulations were performed for different s_0 in the range 0-1000 cm/s. The first case, summarized in Fig. 4.10A, refers to an Al_2O_3 layer with fixed charge density set to zero (not passivated). In the second one, reported in Fig. 4.10B, was simulated an Al_2O_3 layer with fixed charge density set to -1$\times 10^{12}$ cm^{-2} (passivated). In both cases, simulations and measurements, the well passivated devices are in good agreement and the value of current is very similar. In the cases of low charge in the Al_2O_3 the trend between measurements and simulation is similar on the case of higher s_0 despite 1000 cm/s appear to be not enough for reproduce the measurements.

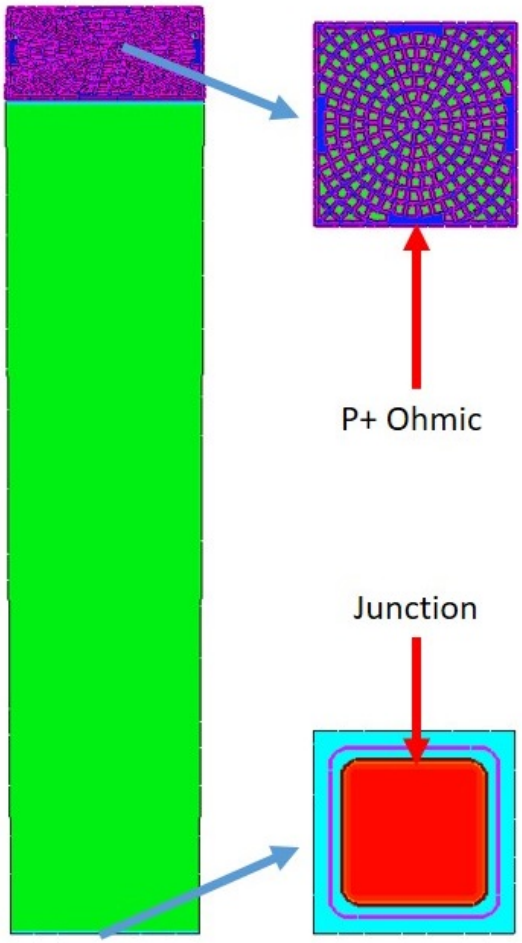

Figure 4.9: Electrical simulation domain for Hyde 2 devices

The I-V curve behaviour depends on the electric field distribution in the detector, which is shown in Fig. 4.11 for two different Al_2O_3 fixed charge densities, i.e., 0 (top slices) and -1×10^{12} cm^{-2} (bottom slices), and two different bias voltages, i.e., 80 V (left slices) and 110 V (right slices). On the top is the n-diffusion creating the junction with the p^- bulk, along with the p-spray. The peak of the electric field is concentrated in this region, whereas the electric field of course decreases with depth in the silicon substrate. In particular, close to the trenches, at bias voltages lower than 80 V, the region

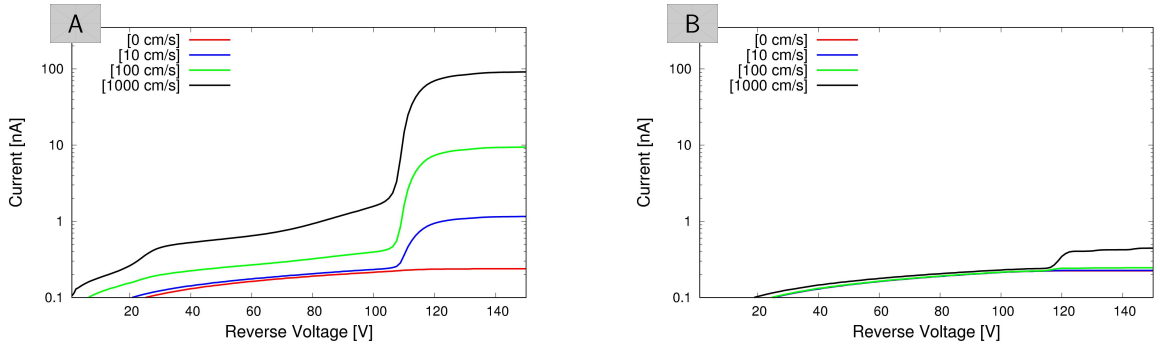

Figure 4.10: A)Simulated I-V curves at different s_0 without fixed charge in Al_2O_3 (not passivated) B)Simulated I-V curves at different s_0 with a fixed charge density in Al_2O_3 of -1×10^{12} cm^{-2} (passivated).

is not depleted and the electric field is negligible. At higher voltage (110 V) the depletion region is deeper and it starts touching the etched part. When this happens, due to the high s_0, the current abruptly increases, unless the surface is passivated. In fact, the absence of any fixed charge causes a large electric field within the silicon wall in between the trenches, that is fully depleted. As a result, surface generation significantly contributes to the leakage current that reaches high values. The situation is different in the presence of passivation with negative fixed charge: in this case the region of interest is not fully depleted and the electric field is weak, so that the surface generation does not contribute to the leakage current.

As far as the wafer fabricated using the stepper equipment for photolithography, the current behaviour was more or less the same before and after the Al_2O_3 passivation step. This was likely to be ascribed to the alumina deposition step, that caused the fixed charge density to be too small to passivate the surface. Several tests were performed to investigate this problem and with the aim of optimizing the process recipes for the alumina deposition and its annealing (temperature and time). The electrical characterization was carried out using MOS capacitor test structures. The

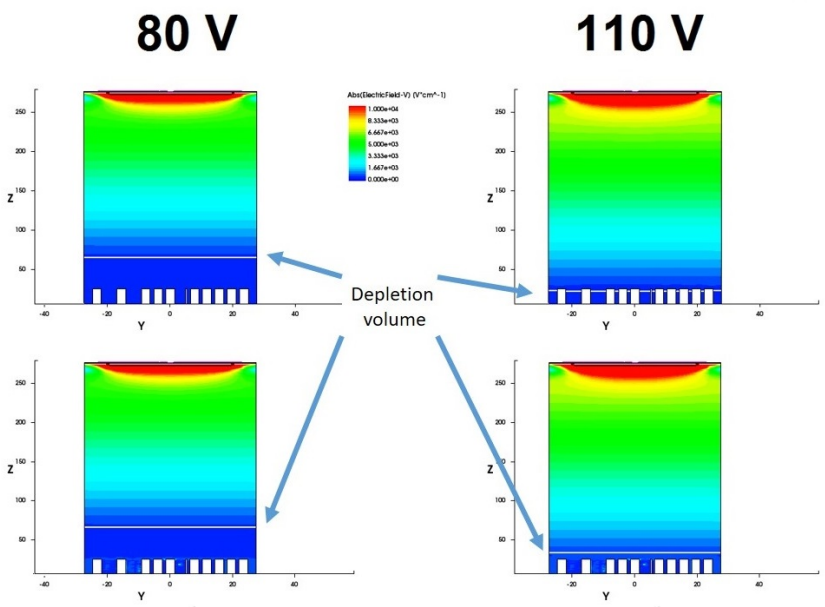

Figure 4.11: Simulated distribution of the electric field along a vertical cross-section of the pixel for two different Al_2O_3 fixed charge densities, i.e., 0 (top slices) and -1×10^{12} cm^{-2} (bottom slices), and two different bias voltages, i.e., 80 V (left slices) and 110 V (right slices).

$Al2O_3$ charge density was estimated from the flat-band voltage measured from C-V curves at high frequency. The resulting values of the charge density for different tests are reported in Table 4.1: it can be seen that in most cases using a larger annealing temperature (425 C) makes the charge density reach large negative values, regardless of the annealing time. Unfortunately, this is not completely reproducible (see production 2), so that low values, of the order of 10^{10} cm^{-2}, both positive and negative, are sometimes obtained, that are not enough to passivate the surface.

The last electrical measurements were the C-V characteristics. From the planar detector (without trenches) it was possible to determine the doping profile of the substrate, $\sim 2 \times 10^{12}$ cm^{-3}, that is compatible with the nominal resistivity of the wafers. Moreover, the full depletion voltage was found to be $\sim$ 110 V for big diode and 130 V for diode-like devices.

The C-V curves measured on the detector with trenches are qualitatively

Production	Annealing		Charge $[cm^{-2}]$
	Temperature [C]	Time [min]	
1	200	10	-9×10^{11}
	425	10	-1.5×10^{12}
	425	40	-1.5×10^{12}
2	425	10	2×10^{10}
3	425	10	-5×10^{12}

Table 4.1: Summary of $Al2O_3$ charge density values for different deposition and annealing recipes

similar.

An example of $1/C^2$-voltage is reported as in figure 4.12 for both a big diode and a diode-like device. In the latter, as expected, the junction segmentation causes the depletion voltage to be slightly larger, but in both cases the saturation value of the capacitance at full depletion is $\sim$ 19.0 pF, that is in good agreement with the geometrical dimensions of the devices. In good passivated perforated devices the depletion stops before extend in the trenches: the total capacitance is equivalent to a planar detector with a thickness reduced of the trenches depth. The capacitance for the produced device etched for $\sim$ 25 μm is $\sim$ 20.5 pF.

After the wafer cutting and device packaging, no significant differences were found in the electrical characteristics of Hyde 2 sensors.

4.2 Functional characterization

The functional characterizations allows the dynamic behaviour of the detector and the charge collection properties to be investigated. To this purpose, four different setups were used for the measurements, depending on the considered excitation source: alpha particles, gamma rays, laser, and X-rays.

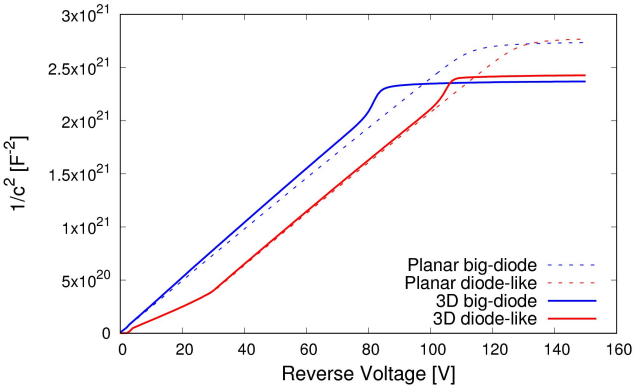

Figure 4.12: $1/C^2$-voltage characteristics of 3D and planar big diode and a diode-like sensors from Hyde 2 batch

4.2.1 Setup for α/γ source

The $\alpha/$ and γ setups are composed of commercial components assembled in order to obtain a full read-out system. The schematic diagram reported in Fig. 4.13 summarizes the different blocks within the chain. The first block is a Charge Sensitive Amplifier, for which two different options were used, depending on the noise performance required: Cremat mod. CR110 and Amptek A250, the latter featuring a lower noise figure. The CSA is connected either to a Cremat Gaussian shaper (CR-200 series) with different possible options for the peaking time, or to a digital trapezoidal shaper (Amptek DP4) with variable shaping time. In case of the gaussian shaper, the data acquisition is carried out by means of a Multichannel Analyser from Amptek (MCA8000D). On the contrary, the digital trapezoidal shaper includes a Multichannel Analyser on board.

To the CSA board are connected the power supply voltages through a low-pass filter. Reverse bias voltage is applied directly to the detector read-out electrode, whereas there is a coupling capacitor between the detector and the amplifier. To the input of the CSA circuit is also connected a capacitor for injecting well known charge packets in order to calibrate the

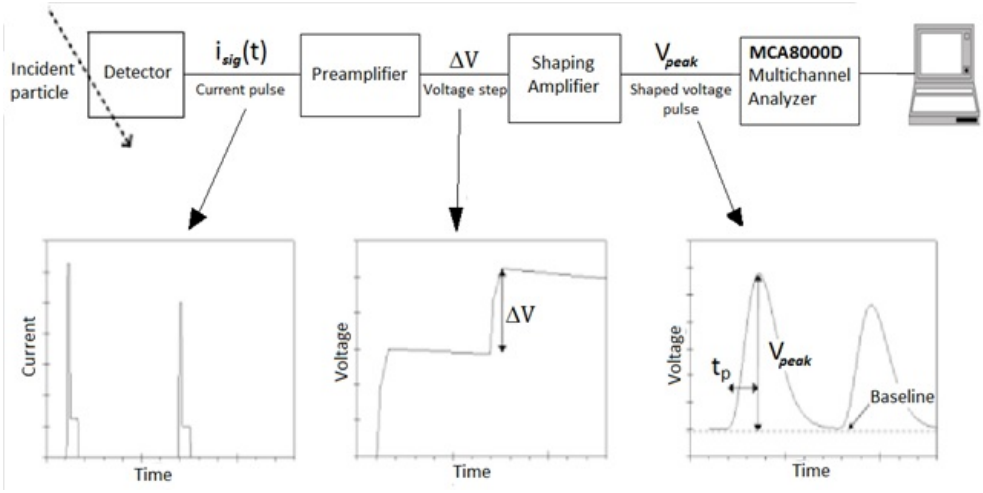

Figure 4.13: Block diagram of the read-out electronics used for α/ and γ tests

measurements. Different shaping times are necessary for two reasons: I) optimize the noise, and II) understand the detector signal dynamics by way of the the ballistic deficits observed with a pulse shaping amplifier. The ballistic deficit is an error in measurements that happens when the detector signal duration is longer than the peaking time [125]. In this case the output voltage is proportional to the charge collected at the peaking time (and not to the total charge induced by an ionizing particle). Another second order effect of ballistic effect is the deformation of the Gaussian tail.

4.2.2 Setup for laser scan

Laser scans allow to obtain spatial information of the collection of charge in the detector. The drawbacks are mainly two: I) the laser light absorption is due to the photoelectric effect and the charge released in the substrate can be very different from that of a charged particle; II) the metal layers covering the sensor shield completely the light, making it impossible to study some regions within the detector, that appear as shadows in the scan. The block diagram if the read-out chain used for laser scans is shown in Fig. 4.14. The front-end section is exactly the same described for the α/γ

source setup, but the digitization is made using an oscilloscope instead of the MCA. The main advantage to use the oscilloscope is related to the possibility to use the laser trigger during the acquisition. By doing so, the signals can be averaged over many samples, with a drastic noise suppression. The oscilloscope used was a Tektronix TDS3052B, with a Matlab software controlling the automatic positioning of the motors and the acquisition. The positioning precision is in the order of 1μm and different laser wavelengths were used to tune the depth of the released charge within the detector. The additional parts of the setup are the two motors (Thorlabs Z712B) and related servo motor (Thorlabs TDC001), as well as the translational stage and the Thorlabs KT112 to couple the fiber to the laser diode. The optical focus lens is a FFC-8/5-λ and the best resolution achievable is few micrometers. The laser driver is home made and it provides pulses with a duration of hundreds picoseconds [126].

4.2.3 Setup for X-ray scan

This setup was used for the measurements with X-rays at the B16 beam line of the Diamond Light Source (Didcot, UK). The X-ray photon flux had an energy of 15 keV and the beam size was $\sim 3\mu$m FWHM. In this case the measurements are performed in a continuous current mode. The detector current is accurately measured using a Keithley 428 current amplifier while the detector is exposed to the X-ray beam. The change of the measured current at each position gives a relative value of the detector efficiency. A picture of the entire setup is shown in Fig. 4.15, highlighting the main components that make up the system.

4.2.4 Laboratory tests on Hyde 1 detectors

For Hyde 1 detectors, the functional tests performed in the laboratory of the University of Trento included α source measurements and laser scans.

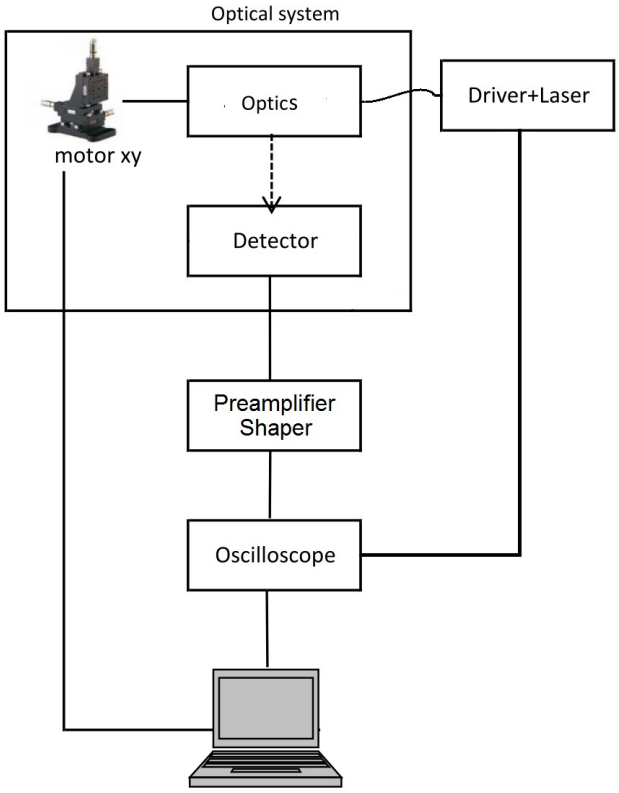

Figure 4.14: Block diagram of the read-out electronics used for laser scan setup

Subsequently, in order to confirm the explanation of some non idealities observed in the charge collection behaviour, X-ray scans were also made.

Noise characterization

The noise characterization is the first step before making any functional measurement, which do require a relativity low noise. The system noise is estimated by measuring the fluctuations of the output signal for a well defined amount of charge fed to the input. The measurements were performed according to the following steps:

- Injection of charge by using a ceramic capacitor with value 1.83 nF. The input voltage was a square signal with tens mV of amplitude generated by using a wave generator (mod. agilent 33220A). The

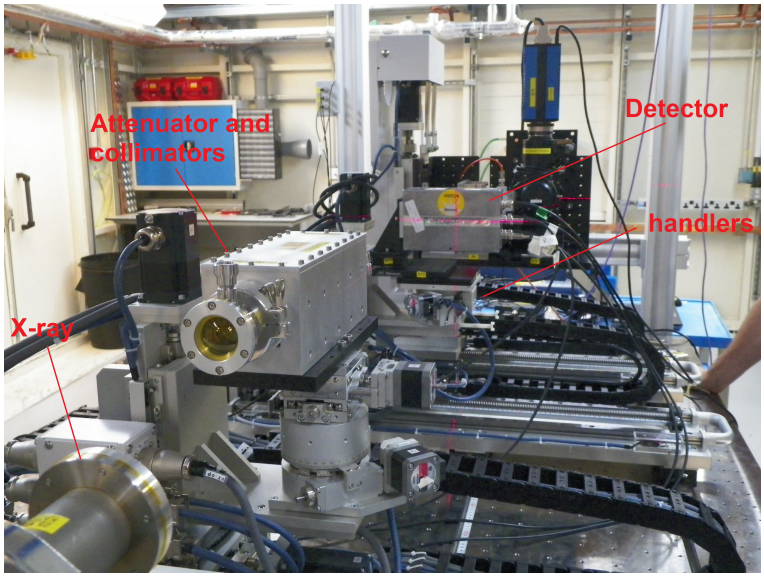

Figure 4.15: X-ray scan setup at B16 beam line at Diamond Light Source.

chosen frequency was 100 Hz according to the dynamic transient of the resistor present in parallel with the feedback capacitor C_f.

- A charge spectrum is obtained at the output of the system, having a gaussian shape due to the noise.
- the standard deviation σ of the Gaussian function is defined as the noise.
- this procedure is repeated for different peaking times of the shapers used (analog and digital) and different bias voltages of the detector.

The observed trends and values do not show significant differences between the digital and the analog shapers. As expected, the digital shaper allows to obtain slightly better noise results mainly because the final MCA stage is embedded in the same shaper board, thus minimizing the introduction of additional noise. A part from its initial impact on the depletion depth, which reduces the noise owing to a lower capacitance, the bias voltage does not significantly change the levels of noise. Figure 4.16

reports the noise for the digital shaper as a function of the shaping time and bias voltage. The minimum noise is $\sim 2\ ke^-$ for a shaping time of $2\mu s$ at the maximum bias voltage of 45 V.

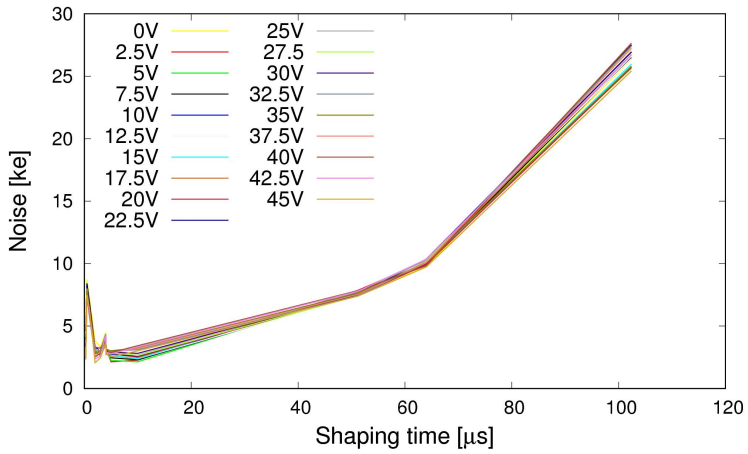

Figure 4.16: Noise as a function of shaping time of the digital shaper at different bias voltages

α source measurements

These measurements are aimed at emulating the detector behaviour when it is coupled with a converter material, but they can be performed on bare silicon sensors (without any converter deposition). The converter material, in fact, would totally stop or at least decelerate most of the α particles, making more difficult the interpretation of the results. The α particles are generated from a source of ^{241}Am with a nominal activity of 3 kBq and a main energy at 5.5 MeV. The setup used is described in section 4.2.1 and uses the Cremat CSA. The source is leaning on an custom made support at a distance of about 1 cm from the detector. The measurements were performed at different bias voltages of the detector and different shaping times, and having the α particles impinging on either the trench side or the contact side of the detector. The contact side is in fact not so interesting,

since its behaviour is expected to be the same as that of a planar detector. In fact, the detector confirmed to be collecting most of the charge already at low voltage and for all the shaping times. Very different is the detector behaviour when the α particles impinge from the trench side: in this case the amount of collected changes dramatically on dependence of the detector bias voltage and of the shaping time. Unfortunately, due to the signal dynamics, the optimum value of the shaping time cannot be used during the measurements. Only two shaping times were used, namely 4μs and 102μs. Shaping times smaller than 4μs are not useful because the collected charge is not high enough, whereas 102μs is the maximum shaping time available in our system. In Fig. 4.17 are reported the α-source spectra using a 4μs shaping time and different bias voltages. The spectra of the collected charge are different from the one predicted by theory: note that the amount of charge expected for α particles travelling in air for 1 cm is approximately 950 ke^-. Some events at about this charge value are in fact present in the spectra (see the relatively flat peak at higher charge in the distribution, which is almost independent from the voltage). However, most of the events correspond to a lower charge value, and this trend is more pronounced at larger bias voltage. At a much longer shaping time of 102μs the detector behaviour dramatically changes, as can be seen in Figure 4.18: the second peak disappears and the charge of the remaining peak is approximately the expected one. However the collected charge slightly decreases as the bias voltage is increased. The trends of the collected charge as a function of bias voltage at both short and long shaping times are reported in 4.19.

Laser scan

Laser scans allow to map the detector efficiency at different geometrical position in the pixel. This analysis was carried out using lasers of different wavelength, different shaping times, and different bias voltages for the

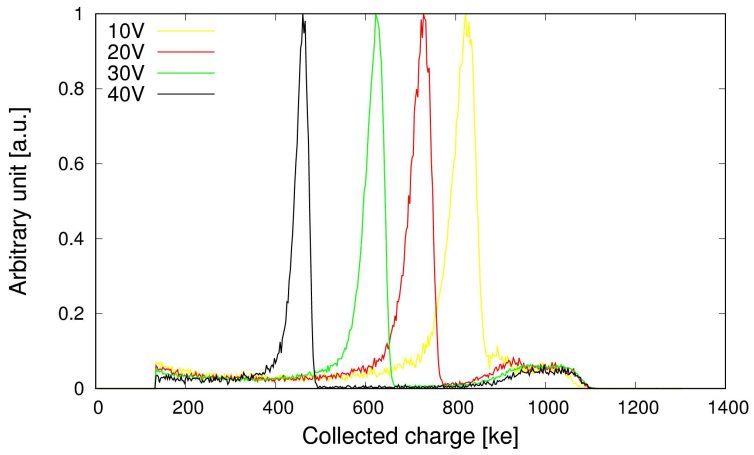

Figure 4.17: Alpha spectra for Hyde 1 detectors measured at different bias voltages with a shaping time of 4μs

detector. The used wavelengths were: 635, 850 and 900 nm. The photon absorption depth is a function of the wavelength: at 635 nm it is ∼2 μm, so as to involve only a region close to the surface of the detector. At 850 and 900 nm, the absorption depths are ∼20 and ∼30 μm, respectively, so as to involve different regions within the detector substrate. However, for the Hyde 1 devices, measurements performed with laser diodes of different wavelength did not show significant differences. On the contrary, varying the shaping time and the bias voltage, it was possible to observe different behaviours, as it also occured with the α source measurements.

Figure 4.20 shows the laser scan of a portion of a pixel (square area of 200×200 μm^2), including part of a trench and the surrounding silicon pillar. The measurements were performed with laser pulses at a wavelength of 850 nm impinging on the sensor trench side. The shaping time is 4 μs and two bias voltages are considered, namely 20 V (A) and 45 V (B).

At 20 V, higher signals are measured from the region surrounding the trenches, as expected, because 850 nm photons are not fully absorbed in the region beneath the bottom of the trenches that is only 30 μm thick.

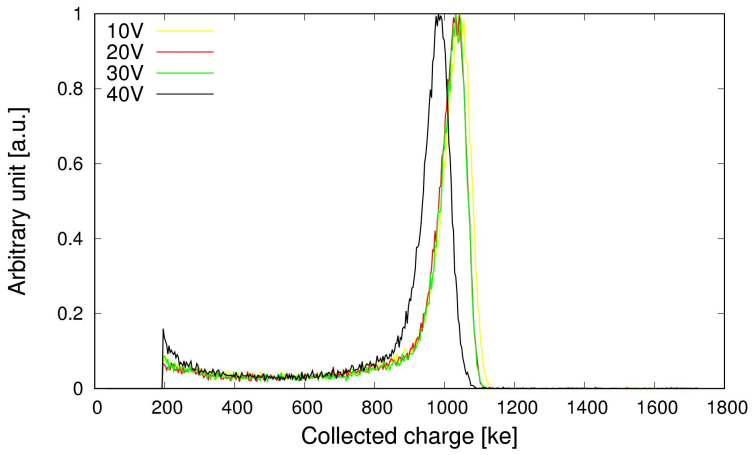

Figure 4.18: Alpha spectra for Hyde 1 detectors measured at different bias voltages with a shaping time of 102μs

On the contrary, a clear signal inversion can be observed at higher voltage: while the signal from the trench region remains almost constant, the signal from the surrounding region is largely reduced. Conversely, in laser scans performed at 102 μs shaping time (see Fig. 4.21) such a behaviour is not observed, and the signals measured at 20 V and 45 V are comparable.

Comparing results from the α source measurements and laser scans, and taking into account the analytical calculation of the probability that α particles impact on the floor of the trenches, based on the geometry of the sensor and the details of the experimental setup, it is possible to attribute the second peak observed in the α spectra to events relevant to the trench region. Similarly, the first peak in the spectra can be assigned to events relevant to the separation wall surrounding the trench.

X-ray scan

The experimental setup for X-ray measurements, involving a current-mode read-out, allows very long shaping times to be emulated. Figure 4.22 shows the maps of the signals at two different voltages, 10 V and 40 V. A normal

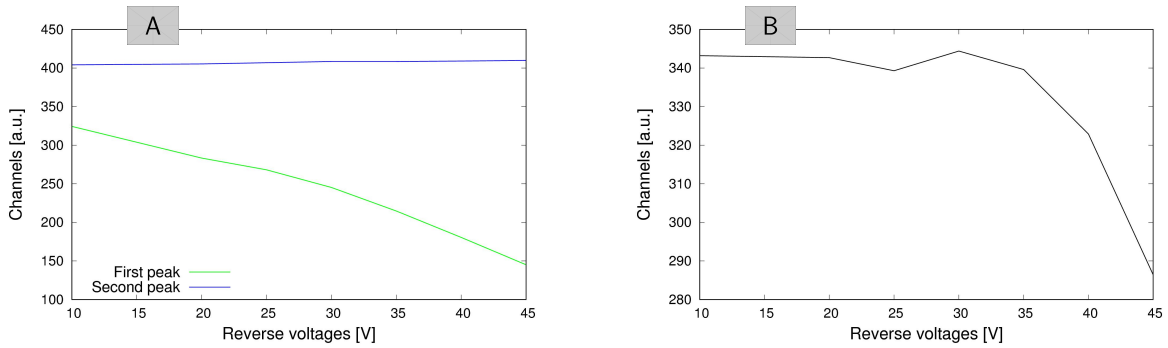

Figure 4.19: Collected charge as a function of bias voltage measured on Hyde 1 detectors with α particles at two different shaping times: A) two peaks trend at $\tau = 4$ μs, and B) single peak trend at $\tau = 102$ μs

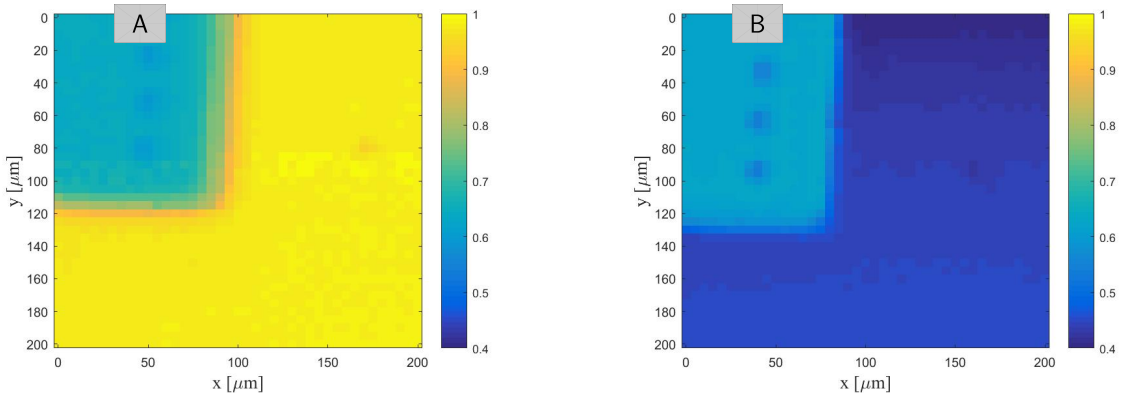

Figure 4.20: Laser scan (wavelength 850 nm) from the sensor trench side performed at 4 μs shaping time and at two different voltages: A) 20 V , and B) 45 V.

trend can be observed, with signals increasing with bias in both regions of the device, i.e., the non-etched active volume around the trench (higher signals because of larger thickness) and the region beneath the trench (lower signals), where the narrow via holes can also be distinguished. Hence, the expected charge collection behaviour can be established in case of very long shaping times. In this respect, looking at the α spectra results, it appears that the maximum shaping time available in the laboratory setup, 102μs, is just enough.

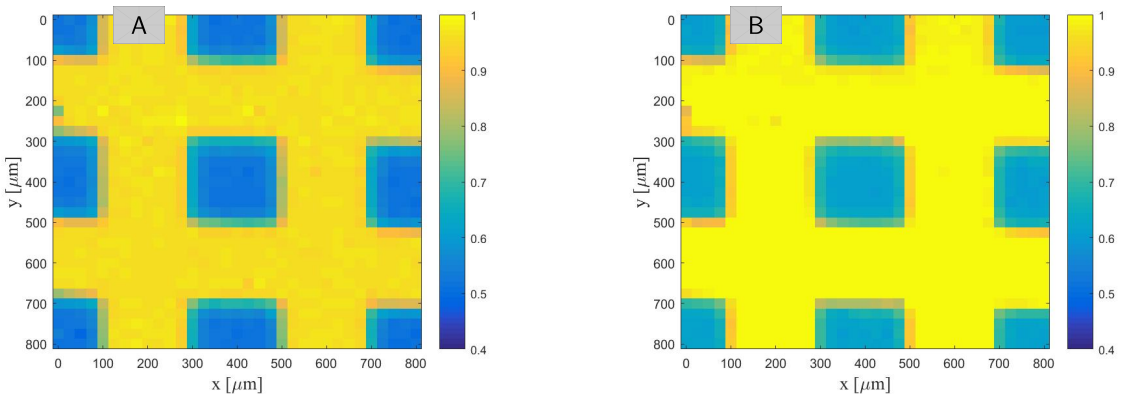

Figure 4.21: Laser scan (wavelength 900 nm) from the sensor trench side performed at 102 μs shaping time and at two different voltages: A) 20 V , and B) 45 V.

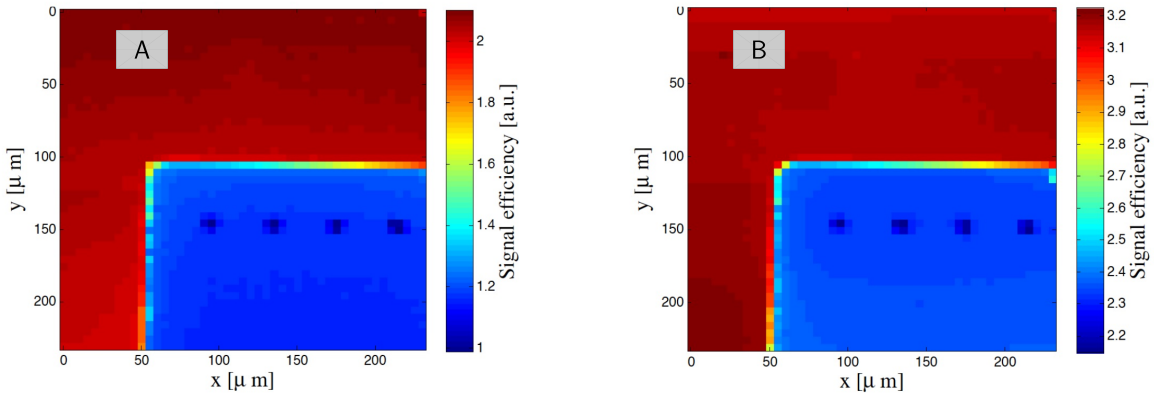

Figure 4.22: X-ray scan from the sensor trench side with current-mode read-out and at two different voltages: A) 10 V , and B) 40 V.[29]

TCAD simulations

The charge collection dynamics, and in particular the response to α particles, can be also simulated using the TCAD software. The Ramo's theorem predicts that signals can also be induced on neighbour pixels. If all pixels are short-circuited, that is the case in our devices, this can influence the observed signals. For this reason, in order to analyse the mutual influence between the trenches, the simulation domain should ideally include four quarters of four neighbour cells. The resulting structure would be very large

and complex, making the computational time a critical issue. A compromise between the computational time (number of nodes in the structure) and the accuracy of the results was considered, focusing the analysis on events relevant to only two quarters of two neighbour cells, as shown in Fig. 4.23a. In particular, four different hit positions for the α particles from the sensor trench side were considered, as shown in Fig. 4.23b.

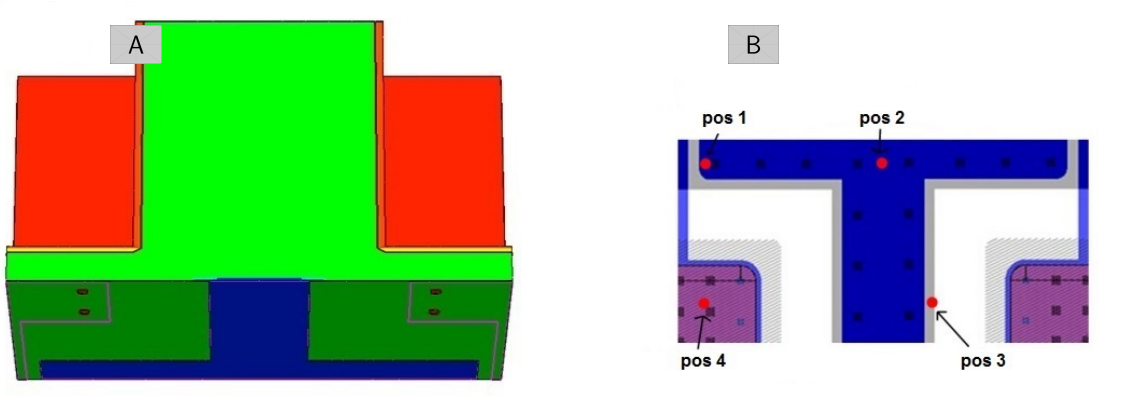

Figure 4.23: A) Simulation domain for α particle simulations; B) Simulated hit positions of α particles from the trench side of the detector.[27]

The hit points were chosen to simulate all cases of practical interest for the measurements: the floor of the trenches (pos. 4) and different positions within the separation wall between trenches (pos. 1-2-3). In fact, positions 1, 2 and 3 yield very similar results, so only those relevant to position 2 will be shown.

The output currents for the two neighbour electrodes and their sum for position 2 at low voltage (5 V) and high voltage (40 V) are shown in Fig. 4.24a and 4.24b, respectively. Due to the weighting field and electric field distributions, the fast components of the individual electrode signals have similar amplitudes but opposite polarities, so they tend to compensate one another if they are summed (note that the sum reflects what happens in a 3D diode, where all cavities are shorted). As a result, the net current has a much smaller amplitude than the two individual currents. This effect was

also present in 3D-STC sensors [127], but it is here much more pronounced due to the large size of the cavities compared to the relatively narrow columnar electrodes of 3D-STC sensors.

Due to the cancellation of the fast signal components, the main contribution to the collected charge comes from the slower tails characterizing the net signals. As a result, the charge collection efficiency increases with the shaping time: it is small at 4 μs but reaches almost 100% at 102 μs. The compensation effect is further enhanced at higher voltage, because the fast components of the signals become more important, leading to a charge collection decrease. This explains the laser scan result and also presence of two distinct peaks at lower charge values in the α spectra measured at at 4 μs (Fig. 4.17), that instead merge into one peak at higher charge at 102 μs peaking time (Fig. 4.18).

The situation is quite different for hits in position 4 (i.e., the trench floor), for which simulations show an almost 100% charge collection efficiency in all cases (see Fig. 4.23c). Accordingly, events relevant to this region are always observed at high charge values, regardless of the shaping time and bias voltage. Since at high shaping time most of the events relevant to different regions within the device correspond to similar (almost full) charge collection values, only one broader peak is observed in Fig. 4.18.

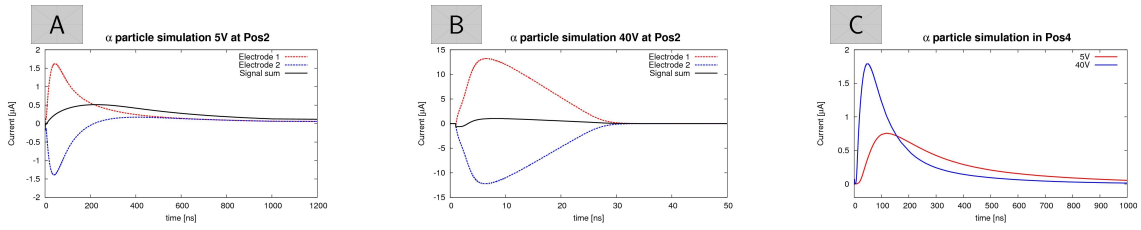

Figure 4.24: Simulated currents from two individual electrodes and their sum for α particle hit position 2 at A) 5 V, and B) 40 V. C) Sum of simulated currents for α particle hit position 4 at 5 V and 40 V.[27]

4.2.5 Laboratory tests on planar detectors

α particle tests on planar detectors were also performed in order to check the charge collection properties and anticipate the behaviour as neutron detectors. To this purpose, the α setup with Cremat CSA was used and, after characterizing the noise, a shaping time of 4μs was chosen. The sensors were tested with α particles impinging on the same side where, afterwards, the converter material was deposited.

Considering the energy loss in air and in dead layers, that for these planar detectors had a considerable thickness (600 nm of silicon oxide, 1.3 μm of aluminium, and a $\sim 1.5 \mu m$) deep n+ junction region), from SRIM simulation it was expected a peak energy for the ^{241}Am of $\simeq$ 2.7 MeV. The measured spectra are shown in Fig. 4.25 for two different voltages: 20 V and 175 V. Only minor differences can be observed between the two spectra, evidence of the negligible effect of the bias voltage on the charge collection efficiency once full depletion is achieved. The relatively low energy of the main peak ($\simeq$2.6 MeV) can be explained by the energy loss of the α particles in air ($\simeq$2 cm) and through the dead layers in the sensor.

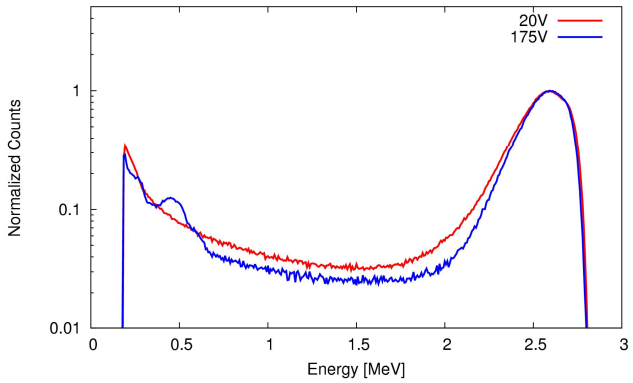

Figure 4.25: Energy spectra for a planar sensor exposed to ^{241}Am source at 20 V and 175 V bias [26]

4.2.6 Laboratory tests on Hyde 2 detectors

For the second generation of our neutron detectors, called Hyde 2, most of the measurements were performed on the "big diode" detector described in section 3.3. The measurements are relevant to devices coming from different wafers, and the deterioration of the charge collection properties due to the low charge density in the alumina passivation layer is also studied. With Hyde 2 devices, as described in details in section 4.2.6, it is possible to use the discrimination setup for the γ suppression. Discrimination results with different γ sources are also reported.

Noise characterization

The first step, also in this case, was the noise characterization of the system. Differently from previous tests, this time the Amptek CS was used in place of the Cremat one. In order to explore a wide range of shaping times, the noise characterization was made using the digital shaper. The noise, expressed in ke^-, is reported in Fig. 4.26. The minimum noise is $\sim$2 ke^- for 20 μs of peaking time, but in fact it does not change significantly in the range 2-20 μs.

α source measurements on devices with a good passivation

The measurements were performed positioning the source at a distance of $\sim$5 mm from the surface of the sensor. The measurements were repeated for two different shaping times (4μs and 250ns) and different bias voltages.

SRIM simulations predict for the α particles an energy loss in air of 0.519 MeV, so that the residual energy when interacting with silicon is about 5 MeV, corresponding to a total ionization charge of $\approx$1.4 Me^-. The alpha spectra for the two considered shaping times at 60 V bias is reported in Fig. 4.27A. The collected charge peaks are significantly different in the two acquired spectra: in particular, for the 4μs shaping time the peak value

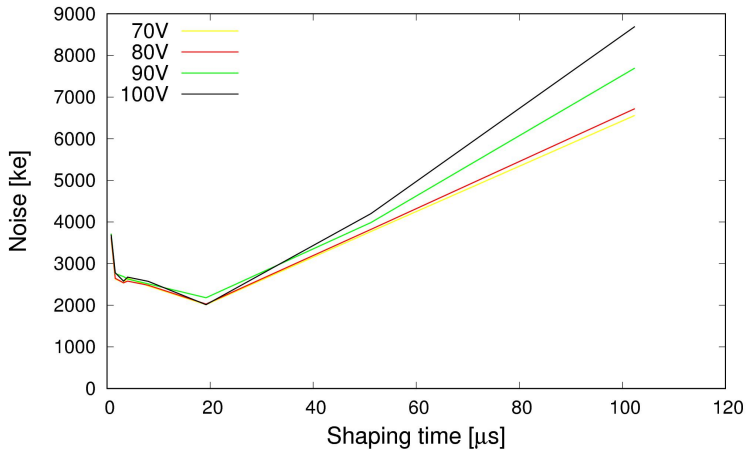

Figure 4.26: Noise as a function of shaping time of the digital shaper at different bias voltages

corresponds to full charge collection, that is not the case for the shorter shaping time. This effect suggests that the signal is not fast enough at the given bias voltage.

Fig 4.27B shows the collected charge as a function of the bias voltage. It can be seen that only at around 90 V there is an increase of the signal speed that allows to observe values corresponding to full charge collection at both shaping times.

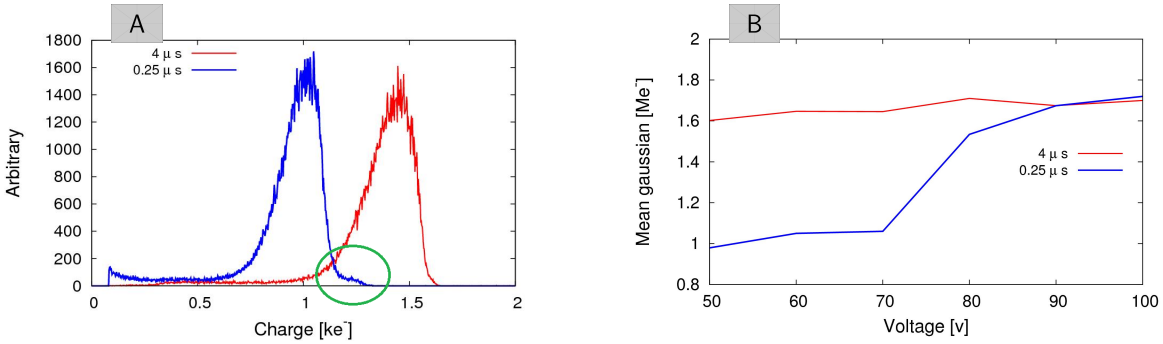

Figure 4.27: A) α spectra for different shaping times at relatively low voltages (60V) B) Collected charge as a function of bias voltage for different shaping times[27]

The low tail at high charge present in the spectrum acquired at 250ns

shaping time (highlighted with a green circle in Fig. 4.27A) also suggests that in this case the signal speed is dependent of the particle hit position. TCAD simulations were performed in order to explain this behaviour. The simulation domain considered was the same single 3D pixel shown in section 4.1.1. Simulations were performed with reference to two possible particle hit positions: at the bottom of the cavities, i.e., close to the edge of the depletion region, and at the top of silicon regions in between the cavities. The α particle energy chosen was of 1.47 MeV that is the most probable energy for the neutron reaction with Boron. The results at different bias voltages are shown in Fig. 4.28A for particles incoming perpendicularly into the cavities (position I) and in Fig. 4.28B for particles releasing charge at the top of regions in between the cavities (position II).

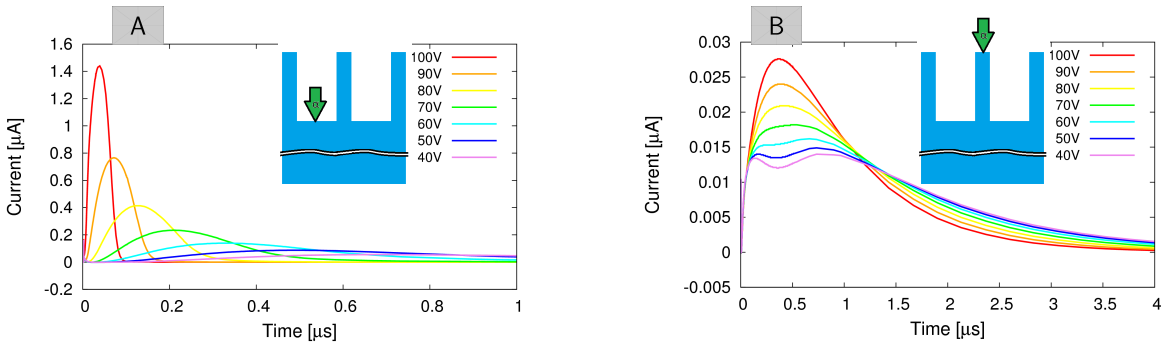

Figure 4.28: A) Output signals for particles hitting in position I (located at the bottom of the cavities), and B) in position II (at the the top of regions in between the cavities).

As expected from the electric field distributions shown in Fig. 4.11, it is expected that at 60 V the electric field is small at both considered hit positions. However, while signals from hits in position II are always slow, signals from hits in position I can become quite fast as the voltage is increased, since charge carriers have to diffuse through a portion of non depleted volume of decreasing depth. As a result, a significant change of the rise time of the signal can be observed for position I events, and this can be used to obtain discrimination of γ-rays, as explained in the following.

α and γ source measurements using γ suppression system

The possibility to modulate to some extent the timing of the signals coming form α particles by changing the reverse bias of the detector can be useful for discrimination purposes. In particular, the α-source releases the charge close the surface of the detector where it is possible to change the electric field intensity. On the contrary, the absorption of high energy γ-rays is based on the Compton effect (as described in section 1.1.3) and the release of charge is random in the entire detector volume.

For a readout based on CSA+shaper, the amplitude of the shaper output signal is proportional to the integral of the current pulse signal at a given peaking time. Additional charge due to slower signals causes a distortion of the shaper signal due to ballistic deficit.

Processing the CSA signal by two shapers with different peaking times it is possible to distinguish three different cases:

- fast signals: both shaping times are greater than or equal to the duration of the input signal of of the pre-amplifier: both shaper outputs are proportional to the total area of the input signal;
- medium speed signals: only one shaping time is longer than the duration of the input signal of the pre-amplifier: only the longer shaper output is proportional to the total area of the input signal area, while the other is affected by ballistic deficit;
- slow signals: both shaping times are shorter than the duration of the input signal of the pre-amplifier: both signals will be not correlated to the total area of the input signal, and the shaper with the longer shaping time will exhibit a higher signal at its output.

Modified alpha setup for Gamma suppression

The setup for the gamma discrimination was conceived to improve the γ

discrimination for planar detectors. It can be successfully used for Hyde 2 detectors that share most of the features of planar detectors. If the signals induced cby α particles are slow while those induced by γ-rays are fast (or vice-versa), they can be distinguished. To this purpose, the general purpose read-out chain used for the acquisition of α spectra has been modified in order to discriminate fast signals from slow ones. The schematic diagram of the system is shown in Fig. 4.29. It consists of a CSA (Amptek A250) mounted on its evaluation board Amptek PC250) connected to two home made shaper boards based on Cremat CR-200 shaper. The input of the shaper circuits has an high impedance and the output of the CSA (adapted at 50 Ω) can easily drive two shapers. The two shapers used have shaping times of 4μs and 250ns, that were chosen as a trade-off between the noise figures and the required signal discrimination properties: the longer one guarantees a full charge collection for any interaction point, whereas the shorter one allows a full charge collection only for signals induced by events occurring far from the sensor surface, i.e., those due to γ-rays. The data acquisition was done by using a digitizer CAEN (mod. DT5751) with a bandwidth of 1GHz. The α/γ discrimination based on signal shape analysis can be problematic from the computational point of view. Therefore, it was chosen to analyse only the amplitude of the shaped signal and not the entire shape of the signal, which strongly simplifies the analysis. The data saved during the acquisition are the amplitudes of both shaper outputs for each event exceeding the preset threshold. Note that the digitizer has the same time scale for both the channels: acquiring signals longer than 4 μs would reduce the acquisition speed because of the amount of data that should be transferred.

A custom software for the acquisition has been developed in Labview and it allows to save only the maximum of the shapers waveforms. The discrimination is performed totally offline using the algorithm summarized

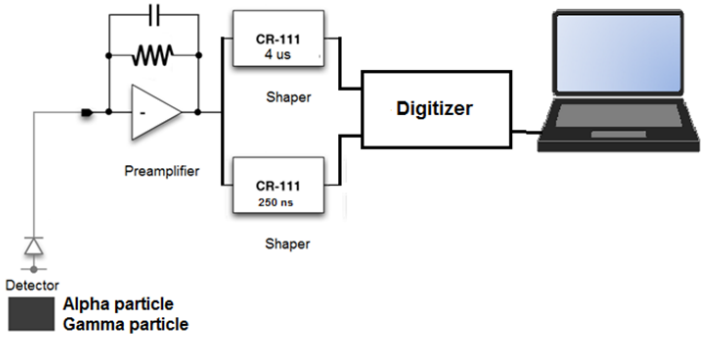

Figure 4.29: Block-diagram of the α/γ discrimination setup.[27]

in Fig. 4.30. It can be seen that the process flow also includes a calibration of the output of both shaper circuits, that is performed by using an injection capacitor integrated on the charge pre-amplifier. The data (expressed in terms of digitizer channel number) contained in the file saved during the acquisition are converted from channel number to energy using the results coming from the calibration. This allows results coming from the two different shapers to be directly compared.

In order to avoid errors coming from the calibration phases, a local threshold is defined in the comparison of the data. The threshold is necessary to define a range of values that can be accepted as correlated signals. A small error of linearization during the calibration or the noise itself can invalidate results containing useful information. The definition of the range must be varied from case to case. In fact, an error of a few hundreds of electrons can be accepted for particles with energy of a few MeV, whereas for particles of lower energies a narrower range must be defined. The threshold is dynamically calculated by defining the range of acceptance as $\mp 10\%$ of the charge value obtained at the output of the shaper with shaping time of 4μs. The algorithm compares all the data and excludes all the results that do not follow the defined rule of signal correlation. The result obtained as the output of the algorithm is the spectrum for the longer

shaping time purged by uncorrelated data.

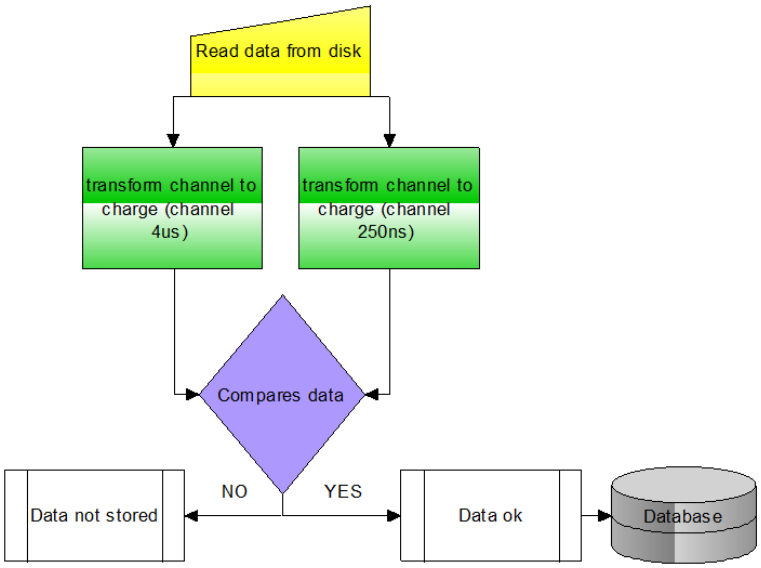

Figure 4.30: The Off line discrimination algorithm [27]

Results obtained with discrimination setup

The validation of the system had the aim to demonstrate that α particles are not discriminated, while signals induced by γ-rays are suppressed. To this purpose, in addition to the ^{241}Am source for α particles, several γ sources were used, i.e., ^{133}Ba, ^{137}Cs, and ^{60}Co.

^{133}Ba emits γ-ray at different energies in a wide spectrum from 53.16 keV to 383.85 keV. The main peaks are at 81, 303 and 356 keV and in silicon, the photons at this energy are absorbed for Compton effect with very low probability of interaction.

^{137}Cs and ^{60}Co are also a γ-ray emitter with energy that in the silicon interact for Compton effect. The main peak for ^{137}Cs 662 keV and for ^{60}Co the main peaks in the spectrum are at 1.173 1.333 MeV.

Biasing the detector at a voltage lower than 70 V, the γ-source signals are well discriminated while maintaining negligible the number of discarded events coming from the α source. Fig. 4.31A summarizes the discrimination

rate as a function of bias voltage for the different sources used.

A relative discrimination of about 90% is achieved with all the γ-rays sources. Unfortunately, it was not possible to calculate the absolute gamma discrimination of the detector because the activity of the sources is not known. Therefore, yhe reported discrimination rates are to be intended as a relative improvement (of about an order of magnitude) provided by the technique here exploited in addition to the intrinsic low detection efficiency of silicon for high-energy γ-rays.

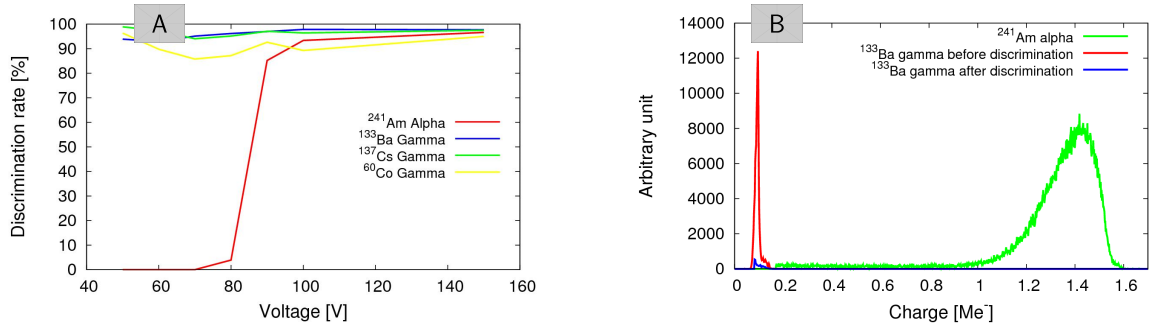

Figure 4.31: A) Discrimination rate for events from different sources. B) Example of spectra acquired at 70 V bias composed of α particle and γ-rays with and without discrimination.[27]

As a further confirmation of the effectiveness of the proposed technique, Figure 4.31B shows the spectra of γ-rays from ^{133}Ba source before and after discrimination along with the spectrum of α-particles. The graphs are referred to a bias voltage of 70 V. In case of α-particles only the spectrum before discrimination is reported because the differences after discrimination are not appreciable.

α source measurements on devices with a poor passivation

The passivation of the trench surface is a key factor to obtain good results from this technology. In the previous section 4.1.3 the electrical characteristics were shown, where at a voltage of the order of 80-100V, the current starts to increase. In the functional tests, an increase of the

current would affect the noise performance of the detector. A solution to this problem could be the reduction of the bias voltage, but the surface generation/recombination influences also the charge collection process. The life time of the radiation induced charge carriers become very short in proximity of the surfaces and this strongly decreases the signals. Figure 4.32A shows the spectra measured with the α-source at different voltages and with a shaping time of 4μs. The collected charge is significantly lower than that of sensors with a well passivated surface. In particular, it is not possible to clearly distinguish the peaks of ^{241}Am and the spectra appear shifted to lower energies and heavily distorted. The analogous spectra measured with a shaping time of 250ns, reported in Fig. 4.32B are further shifted to lower energies and have a slightly different shape. In this case, the attempt to use the discrimination setup fails because the discrimination rate for the α particles is high.

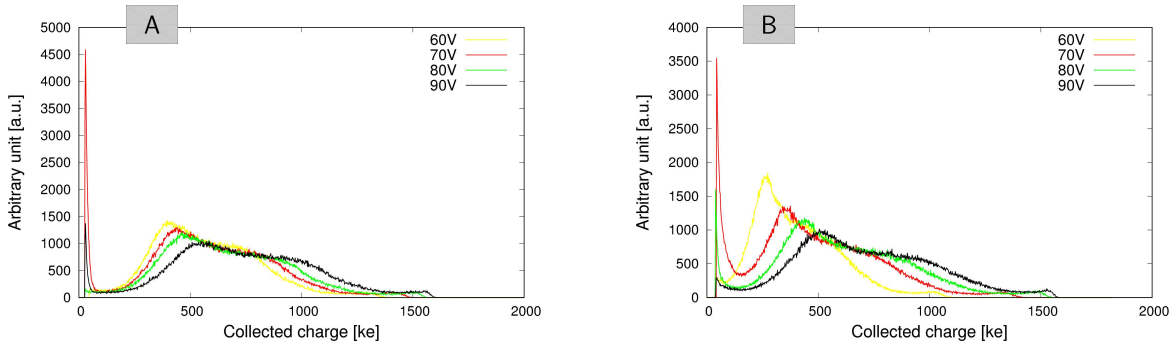

Figure 4.32: α-spectra measured on devices with poor passivation at different voltages and at two different shaping times: A) τ=4μs, and B) τ=250ns

TCAD simulations were performed on a 2D domain of a section of a portion of pixel reported in Fig. 4.33 in order to better understand this behaviour. In the simulation, five points of impact of the α particles were chosen, parallel to the surface and at different distance from it. The simulated release of charge was 0.022 pC and was spatially uniform.

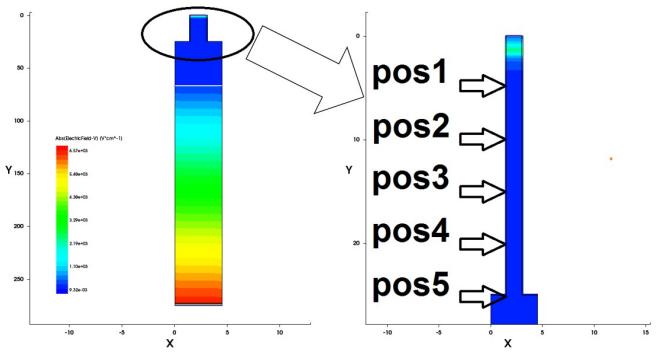

Figure 4.33: Simulation domain with impact points of the α particles.

The simulated charge collection efficiency for the different particle hot positions as a function of the surface recombination velocity is shown in Fig. 4.34A. IT can be seen that the charge collection efficiency decreases with the generation velocity, but to different extents depending on the particle hit position. This explain the reason why the spectra are very distorted: for particles that deposit their energy close the surface of the sensor the efficiency is lower as compared to particles impacting the floor of the trenches.

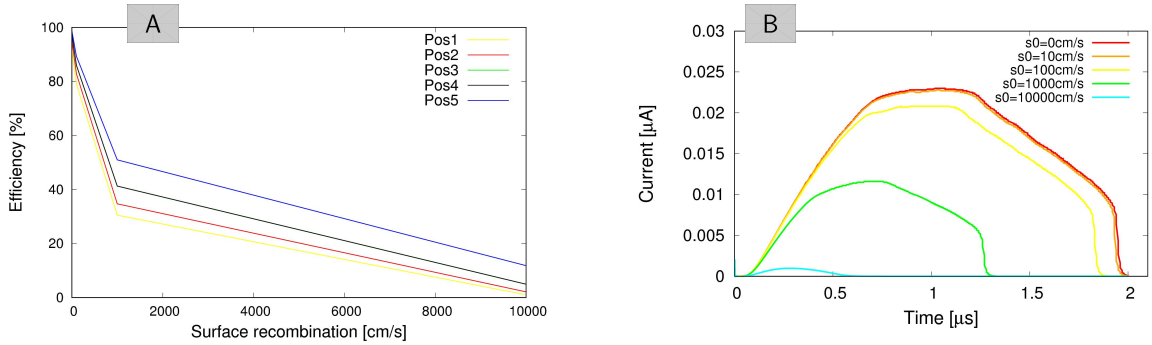

Figure 4.34: A) Charge collection efficiency as a function of the surface recombination velocity for different particle hit positions; B) Current signals at Pos1 for different s_0.

Besides the amplitude, also the signal duration is significantly affected. Fig. 4.34B shows the simulated current signal waveforms for position 1 at

different s_0. An increase of s_0 reduces the probability for the generated charge to survive long enough to leave the damaged area. This effect reduces the pulse width, and it also prevents the gamma discrimination method to operate properly.

The reduction of the collected charge involves also another problem: if the collected charge is below the threshold, it can cause a loss of counts during the exposure to neutron sources, thus affecting the overall neutron detection efficiency.

The ^{241}Am α source is not monochromatic and it is difficult to understand which is the minimum energy deposited in silicon corresponding to a readable signal. To investigate this problem, a solution was studied which consists in attenuating the α particle energy by using thin layers of Mylar (and air). In these experiments the source was placed at a distance of 13.5 mm (air) and the measurements were repeated adding layers of 5μm of Mylar. SRIM simulations were performed to estimate the mean of the Gaussian peak after the passage through the different layers. The data are summarized in Table 4.2.

Layer		Residual energy [MeV]
no layer	-	5.5
Air	13.5 mm	4.24
M	5 μm	3.55
y	10 μm	2.75
l	15 μm	1.79
a	20 μm	0.54
r	25 μm	0.09

Table 4.2: Residual energy for an alpha particle traveling through different layers of air/Mylar

The combination of air and 10 μm of Mylar gives an α particle residual energy that is the most similar to the one relevant to the neutron/boron re-

action. The spectra measured with different layers is reported in Fig. 4.35A. It can be seen that the peak in the collected charge strongly decreases as the Mylar thickness is increased.

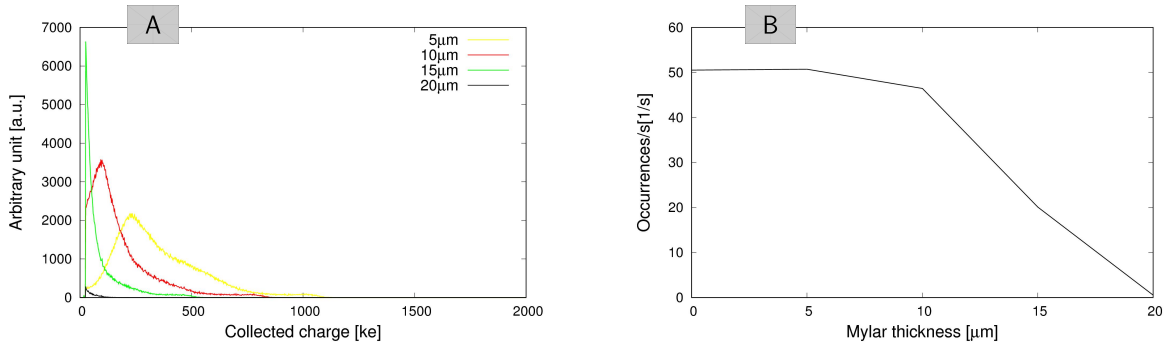

Figure 4.35: A) α particle spectra measured with different layers of air and Mylar. B) Occurrence rate as a function of the Mylar thickness.

The occurrence rate decreases when the energy absorbed by the Mylar layers becomes more relevant. This is related to two different factors: I) low α particle energy are stopped in the Mylar layers, and II) the detector is not able to collect all the charge and the signal does not reach the threshold. In conclusion, the poor passivation of the trenches is a serious problem that can significantly affect the neutron detection efficiency.

CHAPTER 5

Neutron results of neutron detectors

The hybrid neutron detectors were tested at different facilities with fast and thermal neutrons. Preliminary tests with fast neutrons were performed using the Van de Graaff "CN" accelerator at INFN-LNL laboratories (Legnaro, Italy). Protons with an energy of 4 MeV impact a LiF target that generates neutrons with energy of 2.3 MeV ($^7Li(p,n)^7Be$). The flux, at a distance of 60 cm from the detector, is about 100 neutrons cm^{-2} s^{-1}. Additional tests with fast neutrons were performed at the U-120M Isochronous Cyclotron in Rez (Czech Republic). The neutron energy spectrum, as produced in the reaction $^2H^-$ on a thick Be target, was in the wide range 4-12 MeV. In this case the flux is much higher compared to the CN accelerator and corresponds to 10^6 neutrons cm^{-2} s^{-1}. This difference in the flux is the key reason for the largely different timespan of each measurement and the accumulated statistics: one hour in the first case and only 20 minutes at the U-120M line.

Different thermal neutron sources were used for the slow neutrons tests. The first test was performed at a collimated beam of the LVC-15 research

nuclear reactor in Rez (Czech Republic) with an estimated flux of 1.5×10^7 neutrons cm^{-2} s^{-1}. A second series of measurements was performed in a beam line of the TRIGA reactor at Jožef Stefan Institute in Ljubljana (Slovenia). The flux was about 1×10^6 neutrons cm^{-2} s^{-1}. Further tests with thermal neutrons were performed at Politecnico di Milano (Italy) with a moderated neutron source yielding a thermal flux of about 400 neutrons cm^{-2} s^{-1}. In this case the gamma background is fully suppressed.

5.1 Neutron measurements on Hyde 1 devices

5.1.1 Fast neutrons

The first test with fast neutrons had the purpose to check if the reaction products of the polysiloxane converter (protons) can be detected by the silicon sensor. The measurement setup is described in section 4.2.1. During the test, performed at "CN" accelerator, a Hyde 1 geometry filled with polysiloxane was exposed to the neutron flux. The resulting spectrum is reported in Fig. 5.1 along with the spectrum obtained with a calibration source of ^{60}Co on a bare silicon detector. In fact, the γ background emitted from the source and present in the environment during the fast neutron measurement were very similar. At low energy the two spectra are indistinguishable, while from ~ 0.25 MeV they start to deviate, with the detector tested under a neutron flux showing a higher number of counts, that can therefore be attributed to scattered protons from the polysiloxane. However, the small detection volume and the non-optimized sensor geometry do not allow to obtain a statistically significant number of counts.

At a later stage, additional tests were performed at the U-120M Cyclotron in Rez, where the much higher flux allows to collect a large number of events in a relatively short time. Four different samples were tested:

- a bare silicon detector (without a converter) used as reference

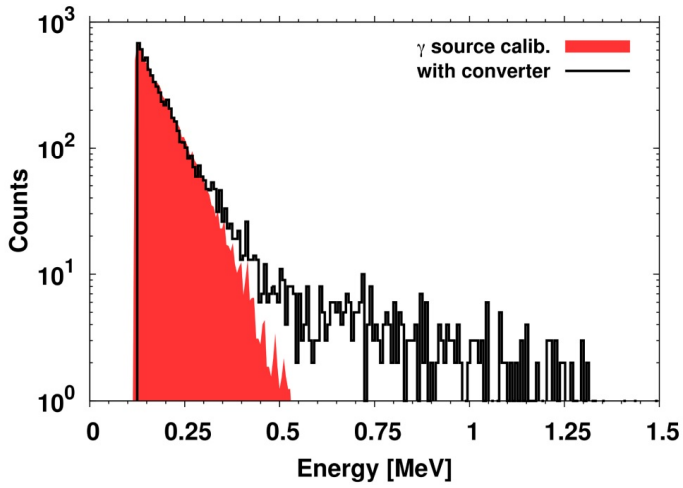

Figure 5.1: Energy spectra obtained from the first test with fast neutrons and the detector calibration with a γ-ray source of ^{60}Co.[25]

- two samples filled with polysiloxane (PDMS)
- a sample filled with PDMS mixed with a concentration of 10% of o-carborane

Figure 5.2 reports the measured spectra: the difference between the empty detector and those filled with converter materials is evident. The empty sensor is only sensitive to the γ-ray background, and the related spectrum is clearly different from the others, thus proving the effectiveness of PDMS as fast neutron converter, although with a very low efficiency due to the very small detection volumes involved. The shoulder at around 230 channels, visible in all the filled sensors, corresponds to the highest detectable energy for the recoil protons, which, according to SRIM simulations, corresponds to a value of 5.5 MeV. The reverse bias of 10 V at 4μs shaping time does not allow a complete charge collection, and this could affect the position of the spectral end point which occurs at lower energies than the expected ones. It is noteworthy that the presence of o-carborane, added with the purpose of reacting with thermal neutrons, does not affect the performance with fast neutrons.

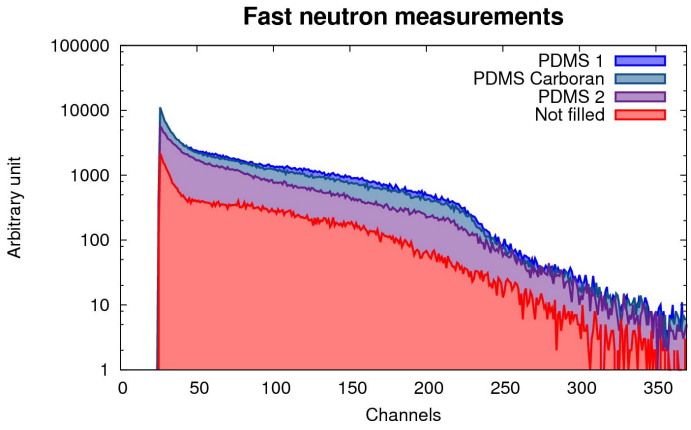

Figure 5.2: Fast neutron spectra obtained with different types of converter material [30]

5.1.2 Thermal neutrons

The first tests with thermal neutron on Hyde 1 devices were performed at LVR-15 research reactor in Rez. During the measurements the neutron flux was monitored by a monitor detector and its value was used to normalize the spectra, although, unfortunately, the reference detector gives only a relative information on the flux. The tested detectors/converter were three:

- a bare silicon detector (without a converter) used as reference
- a detector filled with PDMS with 30% weight concentration of metallic ^{10}B
- a detector filled with ^{6}LiF

The detectors was tested with the neutron flux impinging from the trench side.

Figure 5.3 shows the resulting spectra, The bias voltage was 10 V for the detector with ^{6}LiF and the bare silicon sensor. On the contrary, the bias voltage had to be fixed at only 3 V in the other detector, because the filling with PDMS enriched with ^{10}B damaged the trenches, causing a

sensible increase of the leakage current. Of course, besides the intrinsically low efficiency of the device, the very low bias voltage limits the charge collection efficiency.

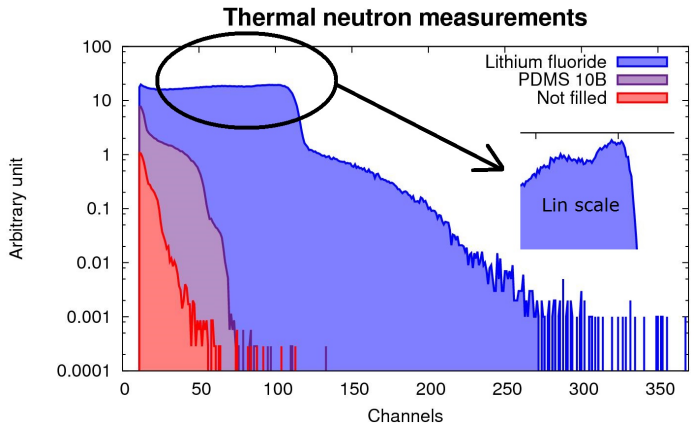

Figure 5.3: Thermal neutron spectra collected at REZ for different sensor/converter combinations [30]

However, a clear difference is visible between the empty and the filled sensors, even for the damaged one. As expected, the sensor filled with ^{6}LiF powder proved to be the most efficient one, allowing also to distinguish the alpha peak at 2.05 MeV and the tritium one at 2.73 MeV (more clearly visible in the linear scale inset of Fig. 5.3). Using these values for a rough conversion of the number of channels to energy, it was also possible to attribute the shoulder observed in the PDMS spectrum around Channel 60 to the α particles emitted by ^{10}B ($\sim$ 1.47 MeV).

Further tests under a thermal neutron flux were performed at the TRIGA reactor at Jožef Stefan Institute in Ljubljana. Four detectors were tested:

- a bare silicon detector (without a converter) used as reference
- the same detector filled with ^{6}LiF used at REZ (as a second reference)
- a detector sputtered with 500 nm ^{10}B

- a detector sputtered with 500 nm $^{10}B_4C$

The neutron flux was impinging perpendicularly to the trench side. The energy spectra measured at a reverse bias of 10 V are reported in Fig. 5.4. The two spectra of the samples with $^{10}B_4C$ and ^{10}B converter clearly show the two main energy peaks for the boron-neutron reactions (α at $1.47MeV$ and α at $1.78MeV$), and are in fact very similar to those obtained from planar detectors measured at the same facility (see section 5.2.

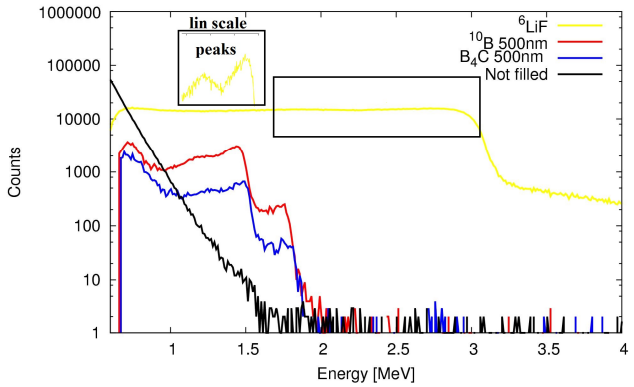

Figure 5.4: Thermal neutron spectra collected at JSI for different sensor/converter combinations [26]

Moreover, the count rates of 3D and planar detectors, after normalizing to the sensor active area, are almost the same. This suggests that the walls of the trenches in 3D sensors were not covered by the sputtered converter: as a result, the only regions contributing to neutron detection are the surface regions in between the trench openings and beneath the floors of the trenches, making 3D sensors behave very similarly to planar ones. The relative efficiency for the detector filled with ^6LiF powder converter is much larger. In this case, the shape of this distribution shown in Fig. 5.4 can be attributed to the complete filling of the cavities with the ^6LiF powder: while this ensures that the vertical walls of the cavities here contribute to the neutron absorption (hence the larger number of counts compared to

the boron based sputtered converters), it flattens the energy distribution since particles generated at different distances from the surface of the cavities release randomly very different energies within the silicon volume. Moreover, this also makes the detection efficiency lower than the maximum theoretical value of ^6LiF since most neutrons are absorbed in the converter at a distance too large from the silicon volume.

Recently, another measurement on the ^6LiF-filled Hyde 1 detector was performed at Politecnico di Milano using a moderated neutron source. In this case the gamma background is suppressed and the neutron flux is well known. The estimated efficiency with neutrons impinging from the contact side is $\sim 3.69\%$ by setting a threshold of 111.6 keV and a using a reverse bias of 10 V. This result, while being comparable to the upper limit achieved with planar detectors in the literature, is much less than the one simulated with Geant4 for the considered Hyde 1 geometry. This is due to several reasons: I) The density of ^6LiF deposited in the form of powder is much less than the one tabulated in Geant3 for the material; II) the detector charge collection process is not very efficient at 10 V, III) the simulation does not take account the dead layer present in the detector.

5.2 Neutron measurements on planar detectors

Functional tests on planar sensors were performed with thermal neutrons at the TRIGA reactor of the Jožef Stefan Institute. The test setup used has been the same as previously described for the α source. For the important role they play in absorbing part of the energy of the reaction products, the dead layers in the sensors should be mentioned. The active area of the planar sensors is covered by 600 nm of silicon oxide and 1.3 μm of aluminium. The n^+ regions were obtained by thermal diffusion, so that the junctions are relatively deep ($1.5\mu m$). SRIM simulations were performed

to estimate the energy loss through these dead layers. As an example, for the 1.47 MeV α particle resulting from the main boron-neutron reaction, the energy released in the silicon active volume is 0.62 MeV. In order to convert the measured spectra from MCA channel units to particle energy a calibration was performed by injecting known amounts of charge through a test capacitor. Owing to the good agreement between the measurements with α source and SRIM simulations, the latter have been used to further improve the calibration of the energy spectra by taking into account the energy loss in the dead layers. Note that this correction shifts all values (including the thresholds) to higher energies. The energy spectra measured at a reverse bias of 175 V are shown in figure 5.5. The two main energy peaks for the boron-neutron reactions (α at $1.47MeV$ and α at $1.78MeV$) are clearly visible from all samples having a converter. On the contrary, the reference sensor only shows the γ-ray background. For sensors with a converter the γ-ray background is high enough to completely mask the energy peaks associated to the ^7Li product of reaction and it prevents the estimation of the neutron detection efficiency.

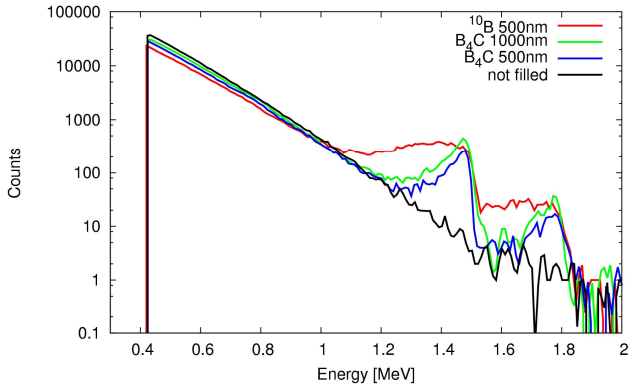

Figure 5.5: Thermal neutron energy spectra measured from planar sensors with different converters at 175 V bias voltage [26]

5.3 Neutron measurements on Hyde 2 devices

Thermal neutron test on Hyde 2 devices were performed at Politecnico di Milano by using a moderated alpha-beryllium neutron source. The thermal neutron flux, at the position where the detector was measured, was of 400 neutrons cm^{-2} s^{-1}. The gamma background was totally suppressed by lead bricks in the moderator layers. The exposure time for each detector was 60 min, with the neutron flux impinging on the detectors from the non-trenched side (junction side). The measured devices were three Hyde 2 detector with different geometries: the trench dimensions were 2.8, 3, and 4.5 μm and the separation wall dimensions were 1.1, 1.5 and 2 μm (devices ID 2.8-1.1, 3-1.5, 4.5-2). All the tested samples had a poor Al_2O_3 passivation due to the low fixed charge density, as previously described. The test setup used was the same as previously described for the gamma discrimination. However, as it was not necessary to discriminate the background gamma sources, only the output of the 4 μs shaper was considered.

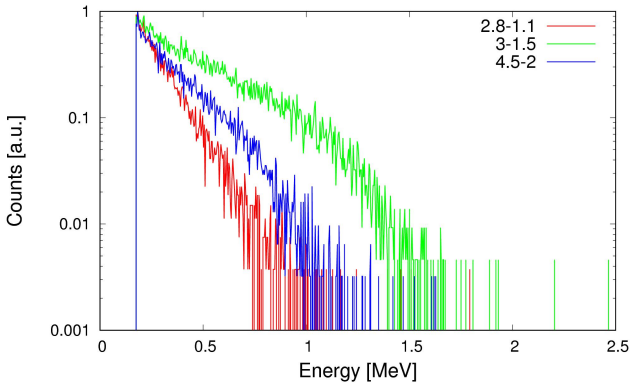

Figure 5.6: Thermal neutron energy spectra collected with Hyde 2 sensors of different geometries filled with ^{10}B

Figure 5.6 shows the energy spectra measured at a reverse bias of 70 V. This voltage value was chosen because it ensures the full charge collection

for the selected shaping time while maintaining the leakage current low. The two main peaks for the boron-neutron reaction (α at $1.48MeV$ and α at $1.78MeV$) are not distinguishable in the spectra, which drop to negligible number of counts (in particular for the sensors with geometries 2.8-1.1 and 4.5-2) at an energy lower than the first expected α energy peak. The neutron detection efficiency is strongly affected by the high surface recombination, as anticipated by the laboratory results with α particles. Depending on the hit point of the reaction products, the collected charge will be more or less curtailed, with high risk to miss the relative events. In particular, the particles at lower energies are affected by two concurrent effects: I) the lower starting energy increases the probability not to reach the threshold; II) the short particle range increases the rate of recombination by the surface defects.

Table 5.1 reports the measured neutron detection efficiency, compared to the simulated one.

Sample	Measured efficiency [%]	Simulated efficiency [%]
2.8-1.1	2.01	31.34
3-1.5	4.00	26.83
4.5-2	2.99	23.37

Table 5.1: Measured and simulated neutron detectiorn efficiency for different sensor geometries

The non homogeneous distribution of the Al_2O_3 fixed charge density is likely the reason for the more efficient behaviour of the device with geometry 3-1.5, for which, although the theoretical energy peaks are not visible, the spectrum reaches a higher energy compared to the other samples. Probably the passivation is here better and the collected charge efficiency is therefore slightly higher.

Three samples with a much better Al_2O_3 passivation were received from LLNL after boron filling. In this case the boron thickness deposition was of

$\sim$ 500 nm on devices where the trenches dimensions was 4.5 μm and the separation walls dimensions was 2.5 μm (devices ID 4.5-2.5).

All three samples had a fairly good Al_2O_3 passivation with fixed charge density able to switch off the surface effect during the IV measurements, as previously described.

During this test only the shaper of 4 μs was considered because of the low background gamma-ray despite is expected a proper operation by using the discrimination setup.

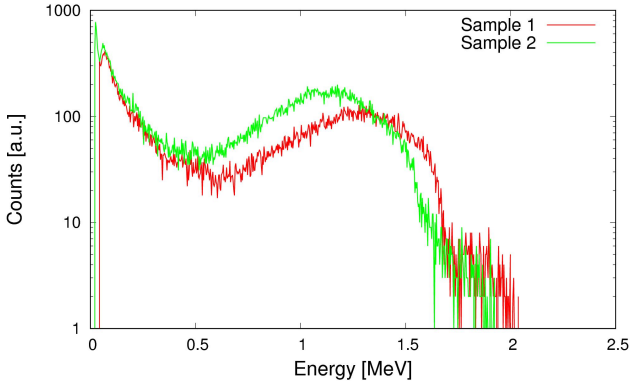

Figure 5.7: Thermal neutron energy spectra collected with Hyde 2 sensors fairly good passivated ^{10}B

Figure 5.7 shows the energy spectra measured at a reverse bias of 70 V as in the previous case.

Although also in this case the two main peaks of the boron-neutron reaction are not clearly distinguishable, there is a single peak at an energy in the range 1-1.8 MeV. The spectra obtained from the two device is slightly different. In particular the results of the sample 2 (green line in figure 5.7) is shifted at lower energy compared the spectrum obtained with the sample 1. This behaviors is given by a worse quality of the deposited alumina: the current measured in the I-V curve was slightly higher (consequently the noise is also slightly higher) and the collected charge is affected by the high

surface recombination.

CHAPTER 6

3D detector for HL-LHC phase II upgrade

Since the early 1980s, when the first planar detectors were fabricated by using the microelectronics process developed by Joseph Kemmer [128], silicon detectors have become of common use for tracking in particle physics. The standardized microelectronics processes allow to have large production volumes as required for big experiments, as, for example, the Large Hadron Collider (LHC) at CERN. The research was very active in this field, and starting from planar sensors, different geometries and new architectures were developed. Among recent developments are the Monolithic Active Pixel Sensors (MAPS) which are fabricated using standard CMOS technologies developed for microprocessors [129].

At LHC, it is foreseen to go for a Phase 2 upgrade bringing the luminosity up to $7 \times 10^{34}\ cm^{-2}s^{-1}$ with a targeted total integrated luminosity of 3000 fb^{-1} [130]. Such a scenario is extremely challenging for detectors, in particular in terms of radiation hardness. Different options, including geometrical modifications as well as materials other from silicon (e.g., diamond [131]) are currently under study.

6.1 State of the art of 3D detectors

A type of silicon sensor with high radiation hardness properties is the 3D architecture. As anticipated in 2.2.5 it was proposed in 1997 by S. Parker and his collaborators in Stanford. The geometry is shown in figure 6.1: the electrodes penetrate in the substrate perpendicularly to the surface.

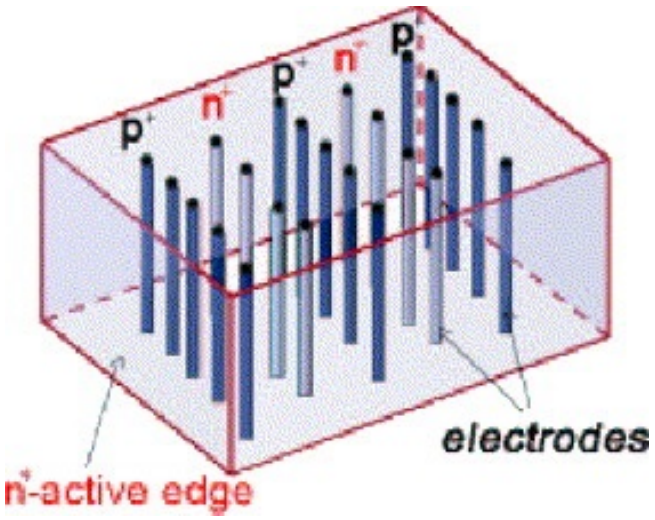

Figure 6.1: Sketch of a 3D detector: the electrodes penetrate through the entire substrate [31]

Differently from planar sensors, in 3D sensors it is possible to decouple the amount of radiation induced charge (proportional to the sensor thickness) from the charge collection path (defined by the layout and depending on the inter-electrode distance [132]). In 3D sensors, the inter-electrode distance can be made much shorter than the substrate thicness: this allows for lower depletion voltages and short charge collection time.

The main, obvious drawback for this approach is the technological complexity. It is indeed not possible to use a CMOS process because several non standard steps like DRIE are required. For this reason, 3D sensors made in Stanford could not progress beyond the level of prototypes, and the process was transferred to Sintef in order to address a possible mass

production. Starting from the early 2000's, several simplified approaches were proposed by different research groups in order to mitigate this problem. The first alternative 3D concepts were developed by FBK[133], Valtion Teknillinen Tutkimuskeskus (VTT) [134] and Brookhaven National Laboratories (BNL)[135]. In those cases "semi-3D" detectors, halfway between planar and 3D, were considered: only columns of one doping type (i.e., junction columns) were etched on one side of the sensor, whereas the bias electrode was maintained planar, on the back side for FBK and VTT, on the front side for BNL. Figure 6.2B and 6.2C sketches the two described developments known as Single Type Column (STC) technology, in comparison to the full 3D technology of 6.2A. The STC approach of course largely reduces the complexity because only a DRIE step is necessary and no support wafer is required.

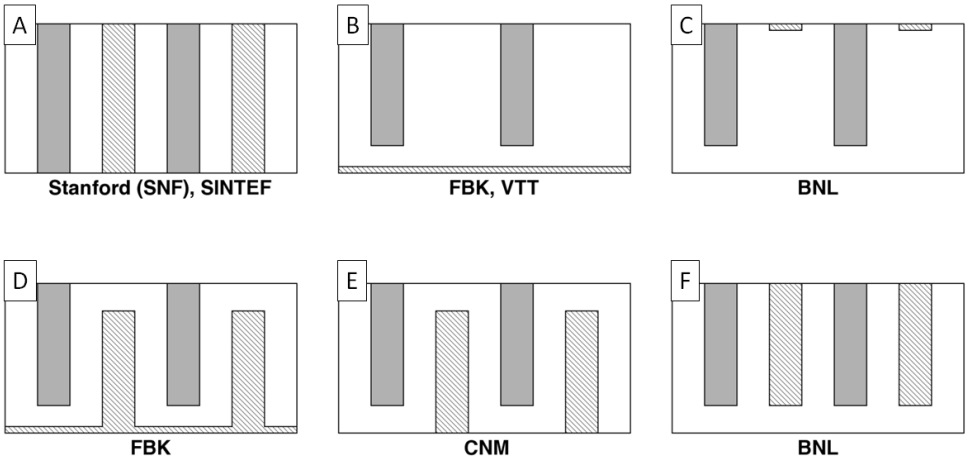

Figure 6.2: A) Original full 3D architecture, B) 3D-STC proposed by FBK and VTT, C) 3D-STC proposed by BNL, D) 3D-DDTC from FBK, 3D-DDTC from CNM, F) 3D-SDTC from BNL [32]

On the other hand, the 3D-STC structures are intrinsically not suitable to achieve a good radiation hardness, and should mainly be intended as a test vehicle to develop the critical steps in the technology [136]. The next

step was the realization of detectors with both type of columns etched in the substrate, although still without a support wafer. These 3D detectors are known as Double Side Double Type Column (3D-DDTC) and were independently developed by FBK [137] and CNM [138]. Their structures are shown in Fig. 6.2D and 6.2E. In both these 3D- DDTC geometries, the columns of different doping type are etched from a different side, and are not passing-through. The main difference between the two approaches is related to the method used for the surface isolation between n-columns (that is p-spray for FBK and p-stop for CNM), and to the column depth. It is worth noting that the alternative solution of ething both column types from the same side (see 6.2F), proposed by BNL, is not really convenient and did not lead to any result.

At FBK, initially, the uncertainty in the etching depth of columns did not allow to obtain a uniform behaviour of the sensors between different productions. In order to avoid this problem, the evolution of the process was to etch electrodes that are passing through all the substrate [139][140][33]. The cross section of the devices is shown in Fig. 6.3. This technology (3D-DDTC+) was used at FBK for the production of the 3D pixel sensors for the ATLAS Insertable B-Layer (IBL). The most important features of this technology are:

- the process is double sided: the columns are etched from both sides.
- there is no poly silicon filling of the columns after the etching
- no support wafer is required
- the p-spray layer used for the the n-type electrode isolation is present on both sides because the columns are passing through
- all n-columns are accessible from one side and all p-columns from the opposite side: this eases the connection with the front-end chip and

the application of the bias from the opposite side.

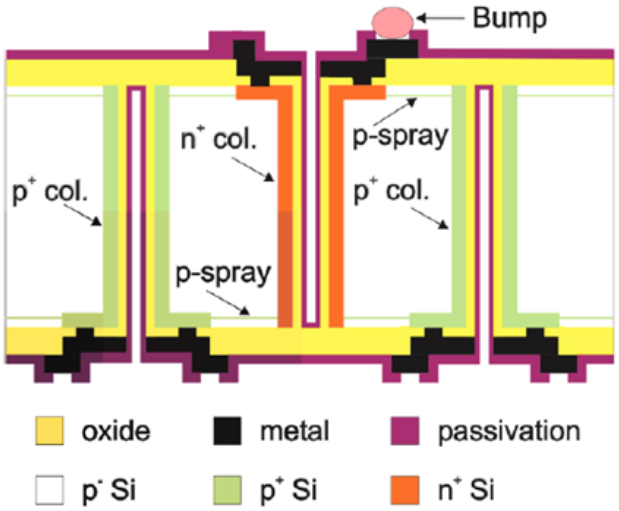

Figure 6.3: Sketch of the cross section for a 3D-DDTC with passing through columns [33]

The charge collection behaviour of these sensors was very good. After irradiation at the IBL benchmark fluence of 5×10^{15} n_{eq}/cm^2, the hit efficiency measured in beam tests at 160 V bias and 15° particle track inclination angle is larger than 98% with a power dissipation lower than 20 mW cm^{-2} at a temperature of -15C. However, the breakdown voltage of these sensors was a concern. Typical values before irradiation were in the range from 35 V to 65 V [141]. The collection of charge before irradiation was almost at 100% already at a few Volts. After irradiation there is a strong increase in the breakdown voltage, because of the higher concentration of positive oxide charge, but it is sometimes not enough to allow for optimum charge collection. Figure 6.4 shows the collected charge for different fluences. Data refer to IBL pixel sensors couple to the FEI4 read-out chip. At the highest fluence of 5×10^{15} n_{eq}/cm^2 the collected charge does not reach saturation before the onset of breakdown. Simulations, also shown in Fig. 6.4, fit very well the measurements before irradiation and at the lowest fluence of 2×10^{15} n_{eq}/cm^2, but deviate from the experimental

data at the highest fluence. This is related to the radiation damage model adopted which is not optimized for this high irradiation levels [142].

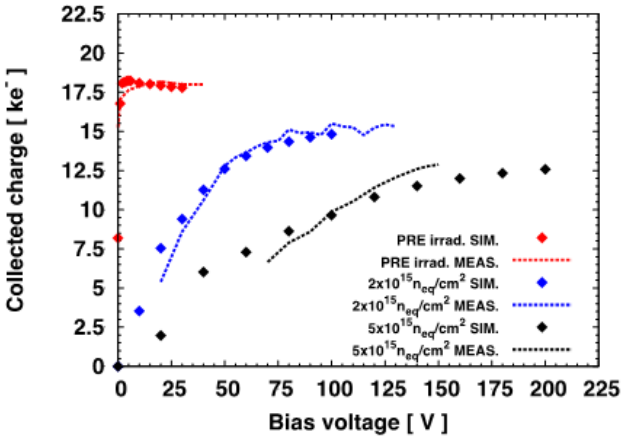

Figure 6.4: Collected charge as a function of bias voltage, measured for selected non irradiated and irradiated 3D-DDTC+ sensors exposed to a ^{90}Sr source. Simulated data are also shown.

In order to increase the breakdown voltage, after an in depth study carried out with TCAD simulations, it was decided to stop the etching of the n^+ columns at ~ 25 μm from the opposite side. This was possible thanks to the much more reproducible DRIE recipes developed at FBK meantime [143]. A considerable breakdown voltage increase was obtained before and after irradiation [141].

6.2 Latest 3D developments

In order to cope with the challenging demands from the application at the High Luminosity LHC, a new generation of 3D sensors had to be developed. The new detector features are: I) increased granularity (25×100 or 50×50 μm^2 (in the old technology the pixel size was 250×50 μm^2), II) shorted inter-electrode distance, III) reduced thickness (~ 100 μm), IV) lower material budget, and V) better geometrical efficiency. These requirements called for a new, single side technology development at FBK.

A sketch of the cross section is shown in Fig. 6.5. A first batch of these detectors was designed at the University of Trento and fabricated at FBK on Silicon–Silicon Direct Wafer Bonded (SiSi DWB) with a diameter of 6 inches. The substrate is a p- Float Zone High-Resistivity directly bonded to a p+ Low-Resistivity handle wafer of a nominal thickness of 100 or 130 μm.

The n columns are insulated by a p-spray layer and they are not etched by DRIE all the way through the substrate, but stop at 15 μm from the handle wafer. This choice is based on the previously mentioned studies aimed at an improvement of the breakdown voltage. In the fabrication process both types of columns are etched from the front side of the wafer and are partially filled with poly silicon.

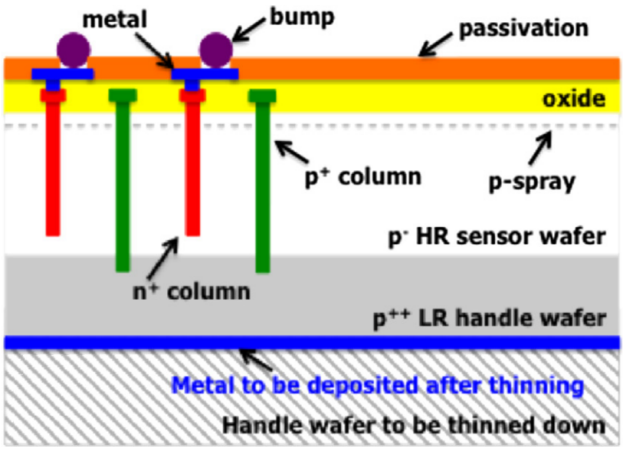

Figure 6.5: Schematic cross-section of the proposed thin 3D sensors on SiSi DWB substrate [34]

6.2.1 Electrical measurements and TCAD simulations

I-V and C-V measurements were performed and compared with TCAD simulations. 3D diodes with different geometries and layout (e.g., with and without a guard ring) were tested at room temperature using a probe station. The leakage current at full depletion, normalized to the number of

columns shorted in the diode, was very good, in the range 0.3 - 3 pA. The relatively large non uniformity was attributed to the quality of the active layer material in terms of lifetime [34]. Relatively high breakdown voltage in the range of $\sim$ 150 V was also measured. The depletion voltage, derived from the C-V curves, was of few Volts for these sensors. The capacitance, normalized to the number of columns, was in the order of $\sim$ 50 fF per column with a small difference (a few fF) for the two thicknesses.

In TCAD simulations, the minimal domain taking advantage of the geometric topology is: 1/4 for the pixel with dimension 50×50 μm^2 and 1/8 for the geometry 25×100 μm^2. The poly silicon was replaced with pure silicon with a constant doping and the metals were replaced by the contacts. Figure 6.6 shows the domain of a simulated pixel.

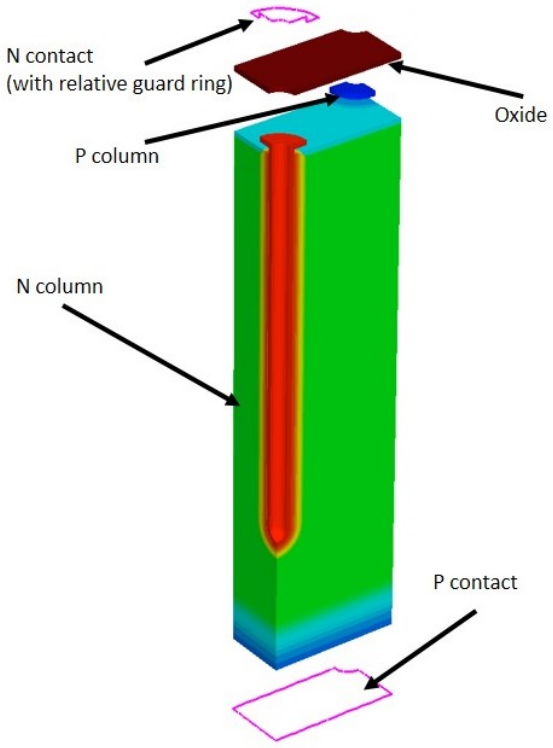

Figure 6.6: Three-dimensional simulation domain of a 3D pixel cell

The simulation results are in very good agreement with the measured

ones. In particular the C-V curves shown in Fig. 6.7A are in excellent agreement with the normalized measured values. The simulated I-V curves, shown in Fig. 6.7B, are also in good agreement compared to the normalized measured values both in terms of leakage current and of breakdown voltage. There is in fact a difference in the current slope, that depends on interface states, so far not included in the simulation model.

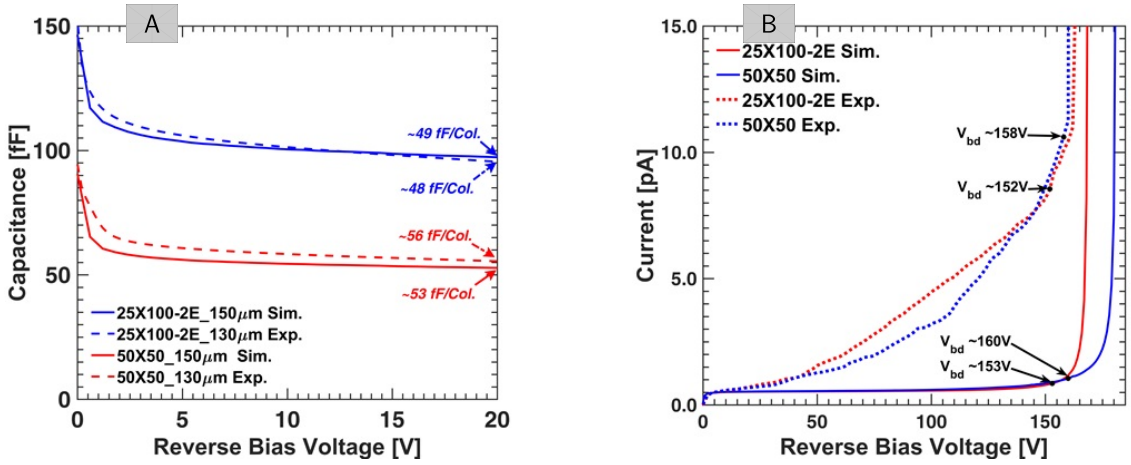

Figure 6.7: Simulated and measured A) C-V curves, and B) I-V curves[35]. All values are normalized to a single column.

6.2.2 Functional Measurements

Functional tests before and after irradiation were performed by using a laser source. The measurements were focused on the most interesting geometry ($50 \times 50\ \mu m^2$) because of the lower capacitance as compared to the $25 \times 100\ \mu m^2$ (2E).

Edge measurements

Slim edge detectors based on multiple ohmic columns were developed for IBL ($\sim$200 μm) [143]. Reducing the inter-electrode spacing allows to achieve even slimmer edges of the order of $\sim$100 μm. These designs were implemented in all 3D diodes. Figure 6.8(1) shows a detail of the diode

layout corresponding to the region scanned with the laser (wavelength λ=1064 nm), having an area of ~200×200 μm^2. The measured signal is shown in Fig. 6.8(3) and compared to the simulated map of the electric field shown in Fig. 6.8(2). A high signal indicates that a non negligible electric field is present, so it can be used to estimate the extension of the depleted volume, that is less than 100 μm at 70 V bias. A very good agreement if found between the simulation and the measurements.

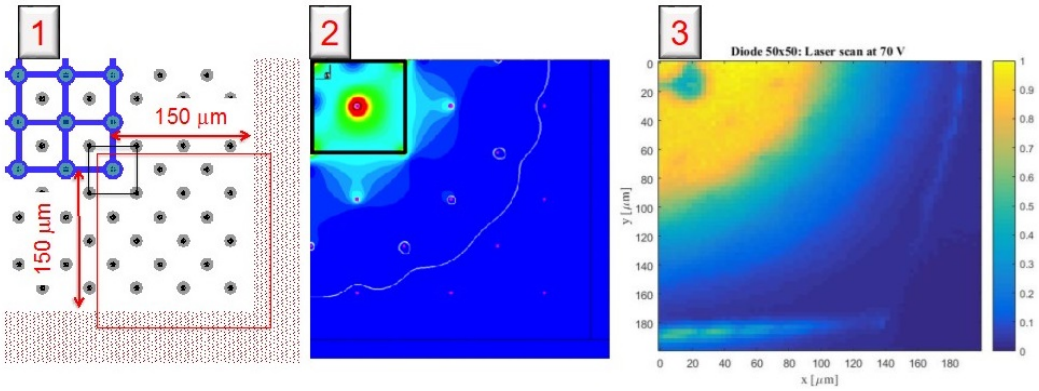

Figure 6.8: 1) Layout of the scanned area, 2) Electrical field simulation, 3) Laser scan at 70 V

Laser scan on irradiated sample

After irradiation the measurements are more difficult for several reasons: the leakage current increase introduces more noise, and the signal becomes smaller. Low temperature operation and storing is necessary to avoiding reverse annealing effects as well as to reduce the current. The measurements were again focused on the geometry 50 × 50 μm^2 after irradiation with neutrons at JSI Lubiana [144] at a fluence of 5×10^{15} n_{eq}/cm^2.

In order to estimate the efficiency the measurement was performed also in a non irradiated sample, in order to have a reference to calculate the charge collection efficiency of the irradiated sample. Keeping the setup and the laser power unchanged, the measurement was repeated for irradiated

sample. The setup was not stable, with temperature oscillations between -10 and -15C, and high umidity. After several tests and handlings, the sample had a breakdown voltage of only 62 V. The temperature was not very stable and oscillated between -10 and -15 C.

Figure 6.9 shows the layout of the region of interest, and the relative efficiency for the laser scan performed at 25, 50 and 60 V. At the maximum possible voltage, the efficiency is quite uniform in the diode volume with a value of about 45%.

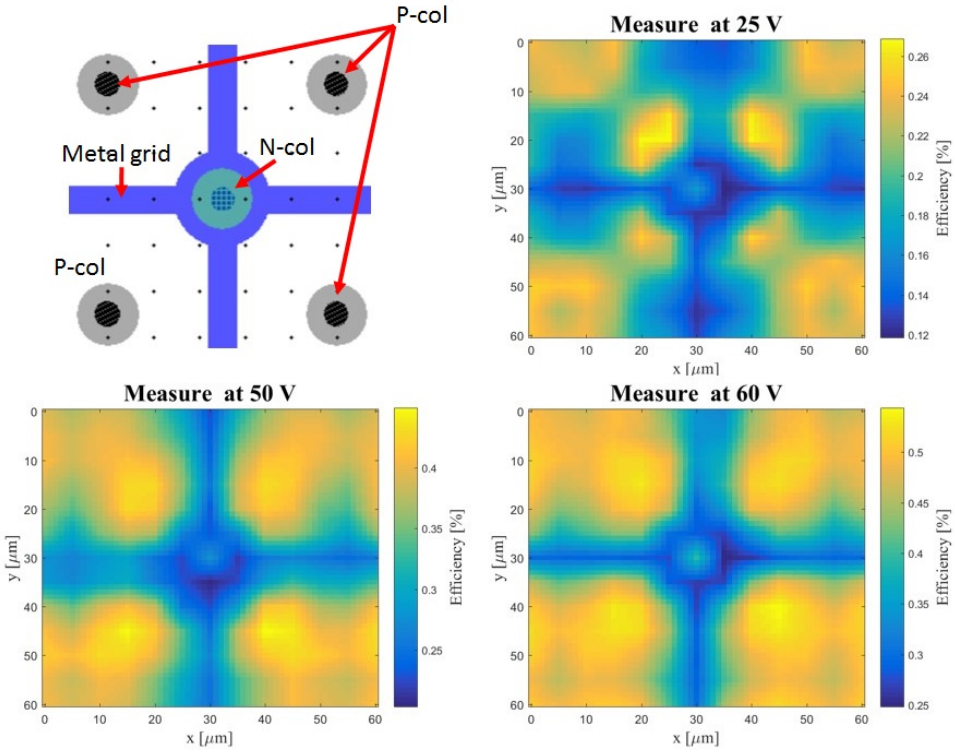

Figure 6.9: Diode layout and laser scan results at different voltages on a sample irradiated at 5×10^{15} n_{eq}/cm^2.

6.2.3 Functional TCAD simulations

TCAD simulations were performed in order to predict the charge collection efficiency after irradiation for the new, small pitch pixel geometries. The first

radiation damage model considered, usually referred as “Perugia” model, is a three-level trap model [2]. It is a recent evolution from a previous model that was limited to a maximum fluence of 1×10^{15} n_{eq}/cm^2 [145]. In Table 6.1 and 6.2 the details of the trap levels in the model are summarized.

Type	Energy [eV]	σ_e cm^{-2}	σ_h cm^{-2}	η cm^{-1}
Acceptor	E_c-0.42	1×10^{-15}	1×10^{-14}	1.613 × F
Acceptor	E_c-0.46	7×10^{-15}	7×10^{-14}	0.9 × F
Donor	E_v+0.36	3.23×10^{-13}	3.23×10^{-14}	0.9 × F

Table 6.1: P-type radiation model up to 7×10^{15} n_{eq}/cm^{-2} [2]

Type	Energy [eV]	σ_e cm^{-2}	σ_h cm^{-2}	η cm^{-1}
Acceptor	E_c-0.42	1×10^{-15}	1×10^{-14}	1.613 × F
Acceptor	E_c-0.46	3×10^{-15}	3×10^{-14}	0.9 × F
Donor	E_v+0.36	3.23×10^{-13}	3.23×10^{-14}	0.9 × F

Table 6.2: P-type radiation model from 7×10^{15} n_{eq}/cm^{-2} to 1.5×10^{16} n_{eq}/cm^{-2} [2]

The first set of simulations was performed at room temperature (T=300 K) for both the 25×100 and the 50×50 μm^2 geometries. The simulation domain was a two dimensional slice of the pixel. TCAD Monte Carlo simulations are not feasible because of the huge computational time. Thus, simulations considered the hit of a minimum ionizing particle at different points uniformly distributed within the 3D pixel cells. The simulation domain and hits points are shown in Fig. 6.10A for the 50×50 μm^2 pixel and in Fig. 6.10A for the 25×100 μm^2 pixel. On the background of both figures is shown the weighting field.

The averaged signal efficiency at different fluences, calculated as the ratio of charge released in silicon and the related collected charge, is shown in Fig. 6.11A for the geometry 50×50 and in Fig. 6.11A for the geometry 25×100. The smaller electrode inter-distance in the latter makes the

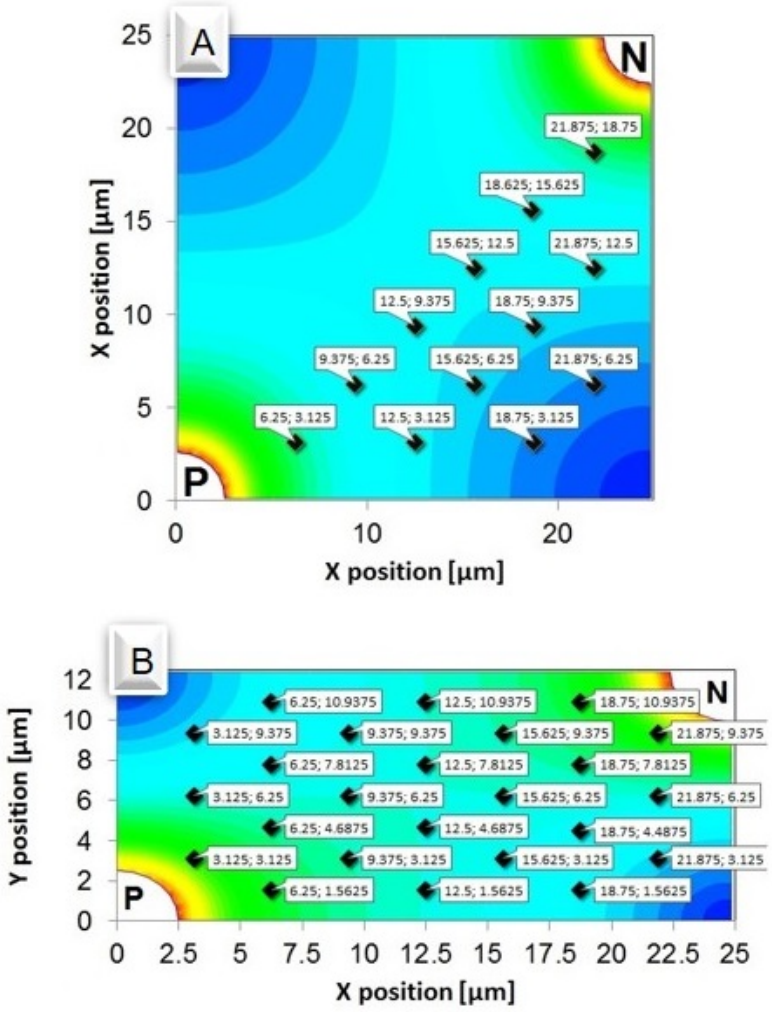

Figure 6.10: 2D simulation domain and m.i.p hit points for the a) 50×50 and B 50×50 pixels. The weighting field is shown on the background.

signal efficiency higher for this geometry. In any case, it is possible to note that the efficiency is very good in absolute terms in both geometries and at about 100 V saturation is reached also at very high fluences in most cases. Only in the 50×50 pixel at the largest fluence of 2×10^{16} n_{eq}/cm^{-2} there is a saturation at higher voltage (around 200 V). Before irradiation, as previously shown, the breakdown is in the range of 160 V and, from simulation and preliminary results, the breakdown votage of irradiated device will exceed these values.

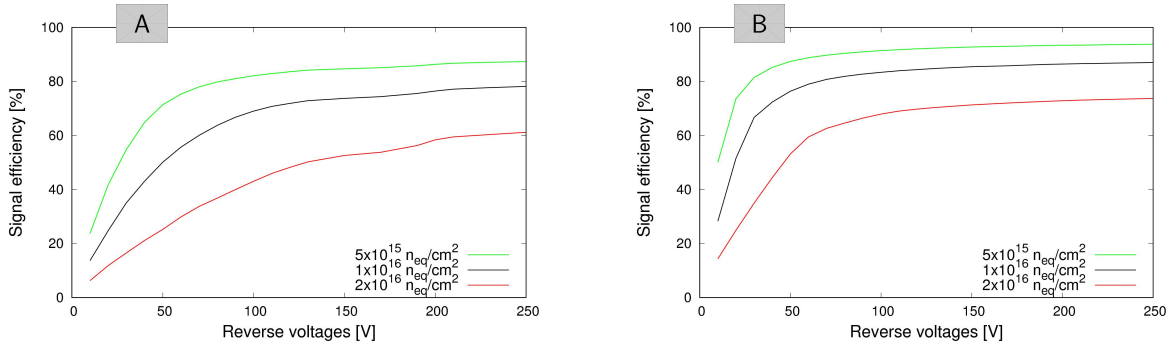

Figure 6.11: Simulated average charge collection efficiency for A) 50×50 geometry and B) 25×100 geometry at different fluences.

Considering the signal efficiency at each particle hit point it is possible to observe that there are points with a particular behaviour: the efficiency is very low at low voltage, and then it suddenly increases with a "threshold" behaviour, finally reaching values much higher than the average. These points are all placed close to the p-column. An example of this behaviour is shown in Fig. 6.12 which is referred to the geometry 50×50 at a fluence of 2×10^{16} n_{eq}/cm^{-2}: the line in the graph labelled as "pos1" corresponds to the hit point closest tothe p-column. The same effect can be observed also for the other geometry and increases with the fluence.

An increase of the charge collection efficiency is in fact expected for the region close to the p-column when, at large voltage, it starts to be depleted, but it is difficult to understand why it reaches so high values. In order to investigate in detail this behaviour, a software model implementing the Ramo's theorem was developed. From TCAD simulations it is possible to extract the data for:

- electric field: is is used to calculate the path of the moving charge (it follows the electric field streamlines)

- the vector of velocity for electrons and holes

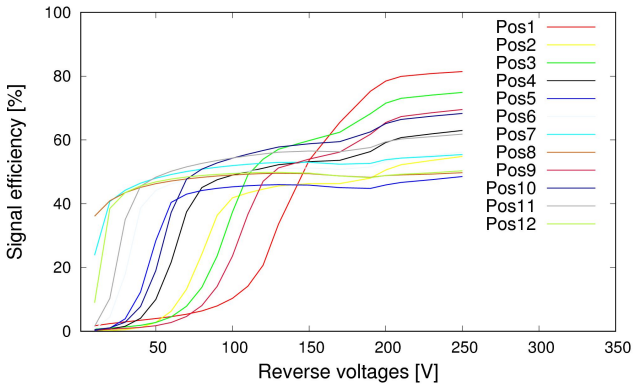

Figure 6.12: Signal efficiency for different hit points in the geometry 50×50 at a fluence of 2×10^{-16} n_{eq}/cm^{-2}

- the weighting field: it is obtained by replacing the silicon substrate with a dielectric (SiO_2) and applying a voltage of 1 V to the read-out electrode (n+)

The first operation, implemented with a Matlab code, is to interpolate the simulated data from the TCAD irregular grid to a regular grid of fixed pitches. From the streamlines it is possible to find the particle velocity along its path. Knowing the path and velocity it is possible to calculate the timing of the charge carriers. The amplitude of the signal can be extracted directly from the Ramo's theorem. Due to this information it is possible to find the induced current versus the time. Charge trapping is considered by using a high recombination rate, as expressed by the formula 6.1:

$$Q(t) = Q_0 e^{-\frac{t}{\tau}} \tag{6.1}$$

where τ is the trapping time that can be extracted from the simulation model.

In particular τ was calculated by using the equation 6.2 [146].

$$\frac{1}{\tau_{e,h}} = \sum_t N_t(1 - P_t^{e,h})\sigma_{e,h}v_{th_{e,h}} \tag{6.2}$$

where N_t is the concentration of the traps, $P_t^{e,h}$ is the trap occupancy probability, that can be calculated using the Fermi distribution, $\sigma_{e,h}$ are the capture cross-sections of the traps for electrons and holes, and $v_{th_{e,h}}$ are the thermal velocities for electrons and holes. Using these parameters it was possible to extract the trapping times for electrons and holes that, for a fluence of 2×10^{16} n_{eq}/cm^{-2} at 300 K, are equal to τ_e=1.23 $\times$ 10^{-9} s and τ_h=1.54 $\times$ 10^{-10} s, respectively. A cross check between the charge collection efficiency calculated by applying the Ramo's theorem algorithm and the TCAD simulation was performed, finding a very good agreement. As an example, two different simulated hitting points are shown: i) in the pixel middle fig. 6.13A and II) close the n column.

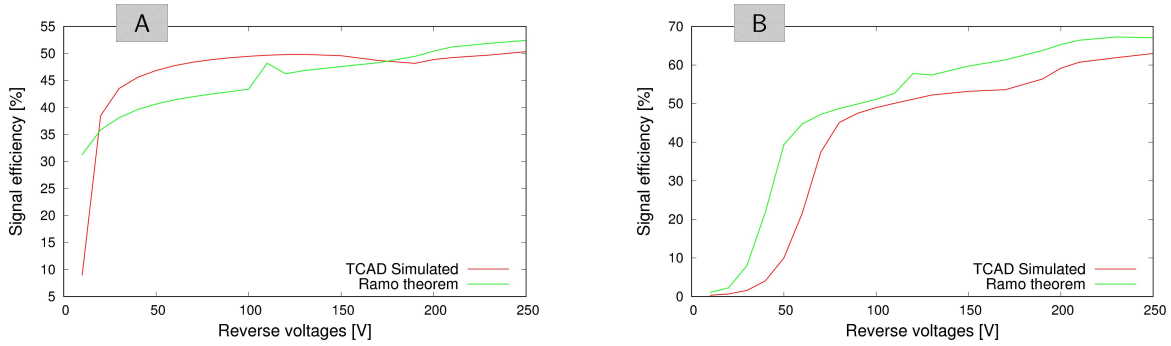

Figure 6.13: Charge collection efficiency comparison between TCAD and Ramo Theory simulation for A)in the pixel middle B) close the n column.

The explanation of the different charge collection trends with voltage is the following: for hit points close to the read-out electrode, signals increase already at low voltage since the weighting field is high, depletion is obtained soon, and trapping of electrons is very small. Therefore, the electron contribution to the signal is achieved soon with minor losses, whereas no contribution from holes is possible due to trapping. Conversely, for hit

points close to the ohmic electrode, like for point "pos 1", signals increase only at the larger voltages necessary for the depletion region to reach these points far from the readout electrode, and can reach higher values because of a concurrent hole-electron contribution. In between these extreme cases lie all the other hit points where different balances between electron and hole contributions to the signal are reached.

The simulation with the Ramo's based software are very fast if compared with the TCAD simulations and for this reason it is possible to have a full map of the pixel. In order to compare the data with laser scans performed in our laboratory on irradiated samples, it was decided to focus on the 5×10^{15} n_{eq}/cm^{-2} fluence, that was the only one available experimentally. In this case the simulation domain was extended to 9 pixels for two reason: I) it is possible simulate points close the edge of the pixels II) it is possible consider the charge sharing with the neighbour pixel. In this case the simulation temperature was of 253 K. The calculated trapping times for this fluence and temperature were, according to the correction of the thermal velocity made by the simulator and the changed Fermi statistics, $\tau_e = 1.55 \times 10^{-9}$s for electrons and $\tau_h = 6.27 \times 10^{-10}$ s for holes. The effects on the signal deriving from the diode configuration, where different read-out electrodes involved are shorted, can be taken into account by calculating the corresponding weighting field distribution.

Figure 6.14 shows the charge collection efficiency maps for four different voltages: 10, 20, 50 and 60 V. Comparing the measured and the simulated plots it is possible to see an important difference. The simulation overestimates the efficiency and anticipates the volume full depletion. The charge collection trend simulated at 10 V is similar to the one measured at 25 V. Further measurements must be performed in order to better understand if the model works correctly at higher fluences and for irradiations with different particles (e.g., protons).

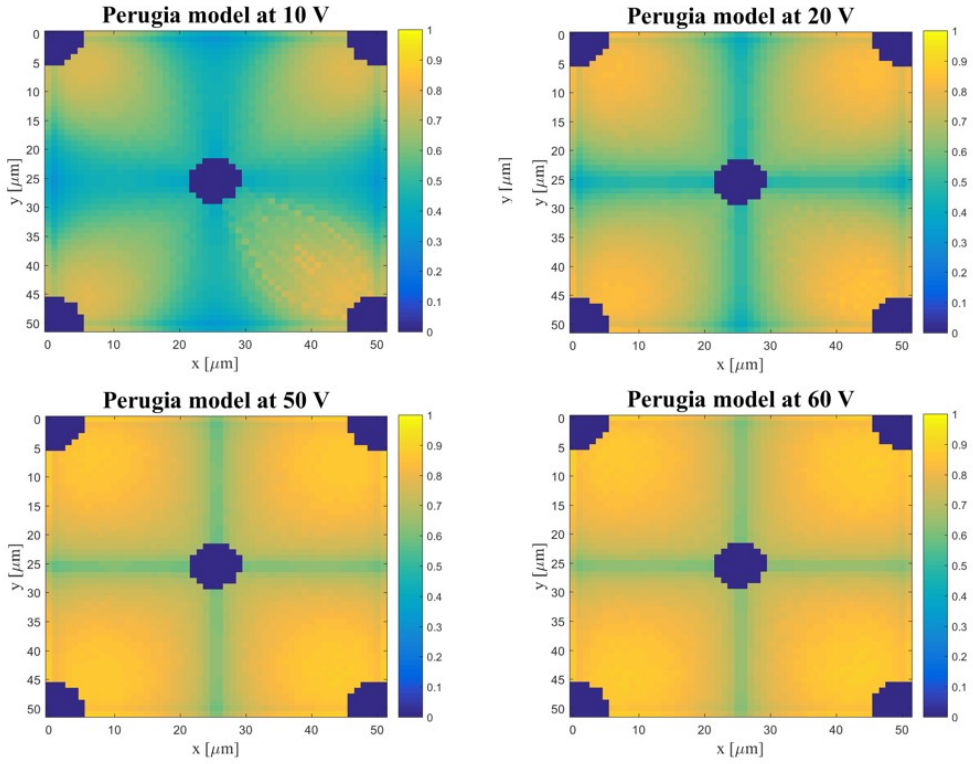

Figure 6.14: Simulated maps of charge collection efficiency for a detector of geometry 50×50 irradiated at a fluence of 5×10^{15} n_{eq}/cm^{-2} and at different voltages.

Comparing the trapping times calculated from the model with the ones extracted from existing measurements reported in literature (which, however, are limited to a maximum fluence of 3×10^{15} cm^{-2}) there is a discrepancy on the values. The effective trapping probabilities can be calculated as $1/\tau_{eff_{e,h}}$ $=\beta_{e,h}(t,T) \cdot \Phi_{eq}$ where $\beta_{e,h}$ depends on the time elapsed after irradiation and the measurement temperature.

Table 6.3 reports the values of effective trapping times damage constants from [3].

The effective trapping times calculated from Table 6.3 are almost the same for electrons and holes: $\tau_e = 0.571 \times 10^{-9}$ s for the electrons and $\tau_h = 0.426 \times 10^{-9}$ s for the holes. This suggests the radiation damage model should be modified to improve the agreement with the measurements.

$t_{min}, T = -10C$	β_h [10^{-16} cm^{-2}/ns]	β_n [10^{-16} cm^{-2}/ns]
Reactor neutrons	4.7±1	3.5±0.6
fast charged hadrons	6.6±1	5.3±0.5

Table 6.3: Trapping time damage constants for silicon detectors irradiated with neutrons and fast charged hadrons [3]

CHAPTER 7

Conclusions and Future Perspectives

This work described the development and characterization of 3D hybrid detectors for thermal and fast neutrons. This activity was carried out within a collaboration of the University of Trento with the INFN Laboratori Nazionali di Legnaro (LNL , in the framework of the HYDE project (HYbrid DEtectors for neutrons), funded by the CSN5 of INFN. The technological partner in this project was Fondazione Bruno Kessler (FBK) owing to the expertise and manufacturing skills acquired in the fabrication of 3D detectors for the ATLAS IBL project.

Two batches of neutron detectors with different geometries were fabricated at FBK between 2012 and 2016. Peculiar to the fabrication approach, from the beginning, was the choice to have sensors fully compatible with pixelated read-out chips, in order to address neutron imaging applications. The quality of the fabrication process was evaluated by the electrical characterization of the devices as well as from the measurements of test structures, from which the main technological parameters were extracted. In both batches the electrical characteristics were investigated in depth with the

aid of numerical simulations with reference to 3D diodes. Besides yielding a good agreement with experimental results, TCAD simulations allowed to understand some non idealities observed in functional testing performed in the laboratory with laser and radioactive sources.

The first production of neutron detectors (Hyde 1) was based on a modified 3D-STC sensor structure aimed at easing the deposition of different converter materials for fast and thermal neutron detection. The feasibility of fast neutron detection was proved by coupling the sensors with a polysiloxane converter, although with a very low efficiency due to the small detection volume involved. For fast neutron detection, having 3D structures is in fact not significant, so the attention was later focused only on thermal neutron detection. Hyde 1 sensors, although not optimized in terms of geometries of the trenches and of the silicon regions in between them, allowed for several tests with thermal neutrons in the presence of different converter materials. As expected, the efficiency recorded was not very high, but Hyde 1 was an important test vehicle providing useful hints for the design of an improved sensor aiming at high performance, namely Hyde 2.

These detectors cannot be considered a direct evolution from Hyde 1 though: a full 3D structure was indeed initially considered, that would increase the charge collection efficiency and speed and make the device more radiation tolerant. However, it also has some drawbacks: a minimum distance is required between columnar electrodes of different doping type, so that the fill factor for the converter material would be low. Moreover, the columnar electrodes are doped by thermal diffusion and the resulting doping profiles are quite deep. Since the reaction products have a short range in silicon, these highly doped regions would compromise the detection efficiency.

Thus, it was deemed more appropriate to design the Hyde 2 detectors with a hybrid structure trying to take advantage of the features of 3D

detectors while maintaining a relatively low process complexity, typical of planar detectors. The fabrication process of Hyde 2 is in fact a planar detector process with the addition of a last step whereby DRIE is used for obtain high aspect ratio trenches with small size and high density on the ohmic side. The trenches are not doped, but rather a thin layer of alumina is deposited by ALD at low temperature (compatible with the aluminium layer used as a metal mask for DRIE) to passivate them before the boron converter filling. Good passivation properties were expected from alumina because of its feature of having a negative fixed charge density. The fabrication process is relatively simple as compared to a 3D process, and it would be suitable for volume productions at relatively low cost. However, the small size of the silicon regions in between the trenches, combined with the effect of the alumina passivation, makes the electric field very small inside them, so that the charge generated by reaction products has to diffuse out of the pillars and reach the depletion region before inducing a signal. While this make the detector slower and less radiation hard, it also provides an effective mean to discriminate neutrons from gamma rays, based on a read-out chain with two filters of different shaping times, without the need to minimize the subtrate thickness. Such a method was successfully demonstrated in this thesis, leading to a 10× suppression of gamma-ray detection as compared to standard read-out. Moreover, the simulated neutron detection efficiency is pretty high, of the order of 30%, and pixel detectors are readily obtained (the fabricated sensors are compatible with the read-out chips of the Medipix/Timepix family), making the considered approch appealing for neutron imaging applications.

Preliminary results under a thermal neutron flux are quite encouraging: despite the poor quality of the Al_2O_3 passivation (the fixed charge density was too low), and the small thickness of the deposited boron converter layer, the measured neutron detection efficiency (∼4%) is comparable to

the maximum value theoretically achievable with a planar detector. Further tests on other samples having an alumina layer with a larger fixed charge density have been planned to check the related improvement in the detection efficiency.

In order for this technology to be reliably used for thermal neutron detectors, the alumina deposition process should be optimized at FBK for making it more reproducible. Another major step should follow, i.e. the pixelated sensors should be filled with enriched boron and coupled with Medipix read-out chip for neutron imaging tests.

BIBLIOGRAPHY

B

[1] David L Price and Kurt Skold. 1. introduction to neutron scattering. *Methods in Experimental Physics*, 23:1–97, 1986.

[2] F Moscatelli, D Passeri, A Morozzi, Roberto Mendicino, G-F Dalla Betta, and GM Bilei. Combined bulk and surface radiation damage effects at very high fluences in silicon detectors: Measurements and tcad simulations. *IEEE Transactions on Nuclear Science*, 63(5):2716–2723, 2016.

[3] Juan Pablo Balbuena, Alexandre Chilingarov, Andrea Candelori, Grant James, Miguel Ullán, Craig Buttar, Giorgio Umberto Pignatel, Alison G Bates, Chris Parkes, Abraham Seiden, et al. Rd50 status report 2008-radiation hard semiconductor devices for very high luminosity colliders. Technical report, 2010.

[4] James F Ziegler, Matthias D Ziegler, and Jochen P Biersack. Srim–the stopping and range of ions in matter (2010). *Nuclear Instruments and Methods in Physics Research Section B: Beam Interactions with Materials and Atoms*, 268(11):1818–1823, 2010.

[5] C Patrignani, Particle Data Group, et al. Review of particle physics. *Chinese physics C*, 40(10):100001, 2016.

[6] DJ Skyrme. The passage of charged particles through silicon. *Nuclear Instruments and Methods*, 57:61–73, 1967.

[7] Helmuth Spieler. *Semiconductor detector systems*, volume 12. Oxford university press, 2005.

[8] Gerhard Lutz et al. *Semiconductor radiation detectors*, volume 40. Springer, 1999.

[9] Stefaan Tavernier. *Experimental techniques in nuclear and particle physics*. Springer Science & Business Media, 2010.

[10] Dorothea Pfeiffer, Filippo Resnati, Jens Birch, Maddi Etxegarai, Richard Hall-Wilton, Carina Höglund, Lars Hultman, Isabel Llamas-Jansa, Eraldo Oliveri, Esko Oksanen, et al. New high-resolution gadolinium-gem neutron detectors for the nmx instrument at ess. *arXiv preprint arXiv:1510.02365*, 2015.

[11] Robert K Smither. Capture-gamma-ray spectrum of cd 113 (n, γ) cd 114 and the associated energy levels in cd 114. *Physical Review*, 124(1):183, 1961.

[12] Douglas S McGregor, MD Hammig, Y-H Yang, HK Gersch, and RT Klann. Design considerations for thin film coated semiconductor thermal neutron detectors—i: basics regarding alpha particle emitting neutron reactive films. *Nuclear Instruments and Methods in Physics Research Section A: Accelerators, Spectrometers, Detectors and Associated Equipment*, 500(1):272–308, 2003.

[13] DS McGregor, WJ McNeil, SL Bellinger, TC Unruh, and JK Shultis. Microstructured semiconductor neutron detectors. *Nuclear Instruments and Methods in Physics Research Section A: Accelerators,*

Spectrometers, Detectors and Associated Equipment, 608(1):125–131, 2009.

[14] SL Bellinger, WJ McNeil, TC Unruh, and DS McGregor. Characteristics of 3d micro-structured semiconductor high efficiency neutron detectors. *IEEE Transactions on Nuclear Science*, 56(3):742–746, 2009.

[15] Ryan G Fronk, Steven L Bellinger, Luke C Henson, Taylor R Ochs, Colten T Smith, J Kenneth Shultis, and Douglas S McGregor. Dual-sided microstructured semiconductor neutron detectors (dsmsnds). *Nuclear Instruments and Methods in Physics Research Section A: Accelerators, Spectrometers, Detectors and Associated Equipment*, 804:201–206, 2015.

[16] RJ Nikolic, Chin Li Cheung, CE Reinhardt, and TF Wang. Roadmap for high efficiency solid-state neutron detectors. In *Optics East 2005*, pages 601305–601305. International Society for Optics and Photonics, 2005.

[17] N Deo, JR Brewer, CE Reinhardt, RJ Nikolić, and CL Cheung. Conformal filling of silicon micropillar platform with b 10 oron. *Journal of Vacuum Science & Technology B: Microelectronics and Nanometer Structures Processing, Measurement, and Phenomena*, 26(4):1309–1314, 2008.

[18] R Dahal, KC Huang, J Clinton, N LiCausi, J-Q Lu, Y Danon, and I Bhat. Self-powered micro-structured solid state neutron detector with very low leakage current and high efficiency. *Applied Physics Letters*, 100(24):243507, 2012.

[19] Kuan-Chih Huang, Rajendra Dahal, James J-Q Lu, Adam Weltz, Yaron Danon, and Ishwara B Bhat. Scalable large-area solid-state

neutron detector with continuous p–n junction and extremely low leakage current. *Nuclear Instruments and Methods in Physics Research Section A: Accelerators, Spectrometers, Detectors and Associated Equipment*, 763:260–265, 2014.

[20] Consuelo Guardiola, Celeste Fleta, Giulio Pellegrini, Francisco García, David Quirion, Joaquin Rodríguez, and Manuel Lozano. Ultra-thin 3d silicon sensors for neutron detection. *Journal of Instrumentation*, 7(03):P03006, 2012.

[21] R Satija, David L Jacobson, Muhammad Arif, and SA Werner. In situ neutron imaging technique for evaluation of water management systems in operating pem fuel cells. *Journal of Power Sources*, 129(2):238–245, 2004.

[22] K Ryzewski, S Herringer, H Bilheux, L Walker, B Sheldon, S Voisin, J-C Bilheux, and V Finocchiaro. Neutron imaging of archaeological bronzes at the oak ridge national laboratory. *Physics Procedia*, 43:343–351, 2013.

[23] Jagjit Nanda, Hassina Bilheux, Sophie Voisin, Gabriel M Veith, Richard Archibald, Lakeisha Walker, Srikanth Allu, Nancy J Dudney, and Sreekanth Pannala. Anomalous discharge product distribution in lithium-air cathodes. *The Journal of Physical Chemistry C*, 116(15):8401–8408, 2012.

[24] R Mendicino, M Boscardin, S Carturan, M Cinausero, G Collazuol, G-F Dalla Betta, M Dalla Palma, F Gramegna, T Marchi, E Perillo, et al. Novel 3d silicon sensors for neutron detection. *Journal of Instrumentation*, 9(05):C05001, 2014.

[25] Matteo Dalla Palma, Gian-Franco Dalla Betta, Gianmaria Collazuol, Tommaso Marchi, Marco Povoli, Roberto Mendicino, Maurizio

Boscardin, Sabina Ronchin, Nicola Zorzi, Gabriele Giacomini, et al. Hybrid detectors for neutrons combining phenyl-polysiloxanes with 3d silicon detectors. In *Advancements in Nuclear Instrumentation Measurement Methods and their Applications (ANIMMA), 2013 3rd International Conference on*, pages 1–9. IEEE, 2013.

[26] R Mendicino, M Boscardin, S Carturan, G-F Dalla Betta, M Dalla Palma, G Maggioni, A Quaranta, and S Ronchin. Characterization of 3d and planar si diodes with different neutron converter materials. *Nuclear Instruments and Methods in Physics Research Section A: Accelerators, Spectrometers, Detectors and Associated Equipment*, 796:23–28, 2015.

[27] R Mendicino, A Bagolini, M Boscardin, G-F Dalla Betta, and N Laidani. Initial results from new 3d neutron detectors. *Journal of Instrumentation*, 11(11):C11002, 2016.

[28] R Mendicino, A Bagolini, M Boscardin, G-F Dalla Betta, M Dalla Palma, and A Quaranta. A new geometry for hybrid detectors of neutrons based on microstructured silicon sensors filled with 10 b 4 c. In *Nuclear Science Symposium and Medical Imaging Conference (NSS/MIC), 2015 IEEE*, pages 1–3. IEEE, 2015.

[29] A Bagolini, M Boscardin, P Conci, M Crivellari, G Giacomini, F Mattedi, C Piemonte, S Ronchin, N Zorzi, MA Benkechkache, et al. Micromachined silicon radiation sensors-part 1: Design and experimental characterization. In *AISEM Annual Conference, 2015 XVIII*, pages 1–4. IEEE, 2015.

[30] Gian-Franco Dalla Betta, Maurizio Boscardin, Sara Carturan, Marco Cinausero, Gianmaria Collazuol, Matteo Dalla Palma, Gabriele Giacomini, Fabiana Gramegna, Carlos Granja, Tommaso Marchi, et al.

Hybrid detectors of neutrons based on 3d silicon sensors with polysiloxane converter. In *Nuclear Science Symposium and Medical Imaging Conference (NSS/MIC), 2013 IEEE*, pages 1–6. IEEE, 2013.

[31] A Kok, G Anelli, C DaVia, J Hasi, P Jarron, C Kenney, J Morse, Sherwood Parker, J Segal, S Watts, et al. 3d detectors—state of the art. *Nuclear Instruments and Methods in Physics Research Section A: Accelerators, Spectrometers, Detectors and Associated Equipment*, 560(1):127–130, 2006.

[32] Marco Povoli. *Development of enhanced double-sided 3D radiation sensors for pixel detector upgrades at HL-LHC*. PhD thesis, University of Trento, 2013.

[33] Gabriele Giacomini, Alvise Bagolini, Maurizio Boscardin, Gian-Franco Dalla Betta, Francesca Mattedi, Marco Povoli, Elisa Vianello, and Nicola Zorzi. Development of double-sided full-passing-column 3d sensors at fbk. *IEEE Transactions on Nuclear Science*, 60(3):2357–2366, 2013.

[34] G-F Dalla Betta, Maurizio Boscardin, Giovanni Darbo, Roberto Mendicino, Marco Meschini, Alberto Messineo, Sabina Ronchin, DMS Sultan, and Nicola Zorzi. Development of a new generation of 3d pixel sensors for hl-lhc. *Nuclear Instruments and Methods in Physics Research Section A: Accelerators, Spectrometers, Detectors and Associated Equipment*, 824:386–387, 2016.

[35] DMS Sultan, G-F Dalla Betta, Roberto Mendicino, Maurizio Boscardin, Sabina Ronchin, and Nicola Zorzi. First production of new thin 3d sensors for hl-lhc at fbk. *Journal of Instrumentation*, 12(01):C01022, 2017.

[36] Glenn F Knoll. *Radiation detection and measurement*. John Wiley & Sons, 2010.

[37] Ch Tschalär. Straggling distributions of large energy losses. *Nuclear Instruments and Methods*, 61(2):141–156, 1968.

[38] William Shockley. Electrons and holes in semiconductors. *&*, 471:237, 1950.

[39] Chih-Tang Sah, Robert N Noyce, and William Shockley. Carrier generation and recombination in pn junctions and pn junction characteristics. *Proceedings of the IRE*, 45(9):1228–1243, 1957.

[40] Simon Ramo. Currents induced by electron motion. *Proceedings of the IRE*, 27(9):584–585, 1939.

[41] F Perotti and C Fiorini. Observed energy dependence of fano factor in silicon at hard x-ray energies. *Nuclear Instruments and Methods in Physics Research Section A: Accelerators, Spectrometers, Detectors and Associated Equipment*, 423(2):356–363, 1999.

[42] C Cottini, E Gatti, G Giannelli, and G Rozzi. Minimum noise preamplifier for fast ionization chambers. *Il Nuovo Cimento (1955-1965)*, 3(2):473–483, 1956.

[43] Michael Moll. Radiation damage in silicon detectors. *Deutsches Elektron-Synchrotron (DESY)*, 1999.

[44] Victor AJ Van Lint, TM Flanagan, RE Leadon, James A Naber, and VC Rogers. Mechanisms of radiation effects in electronic materials. volume 1. *NASA STI/Recon Technical Report A*, 81, 1980.

[45] G Kramberger, V Cindro, I Mandić, M Mikuž, and M Zavrtanik. Determination of effective trapping times for electrons and holes

in irradiated silicon. *Nuclear Instruments and Methods in Physics Research Section A: Accelerators, Spectrometers, Detectors and Associated Equipment*, 476(3):645–651, 2002.

[46] Gijs Dingemans and WMM Kessels. Status and prospects of al2o3-based surface passivation schemes for silicon solar cells. *Journal of Vacuum Science & Technology A: Vacuum, Surfaces, and Films*, 30(4):040802, 2012.

[47] Richard T Kouzes. The 3he supply problem. Technical report, Pacific Northwest National Laboratory (PNNL), Richland, WA (US), 2009.

[48] NIST's Systems Integration for Manufacturing Applications (SIMA) Program. Nist standard reference database 144. `http://physics.nist.gov/cgi-bin/Compositions/stand_alone.pl`. [Online; accessed 2017-01-02].

[49] Richard T Kouzes, Azaree T Lintereur, and Edward R Siciliano. Progress in alternative neutron detection to address the helium-3 shortage. *Nuclear Instruments and Methods in Physics Research Section A: Accelerators, Spectrometers, Detectors and Associated Equipment*, 784:172–175, 2015.

[50] Richard T Kouzes, James H Ely, Luke E Erikson, Warnick J Kernan, Azaree T Lintereur, Edward R Siciliano, Daniel L Stephens, David C Stromswold, Renee M Van Ginhoven, and Mitchell L Woodring. Neutron detection alternatives to 3 he for national security applications. *Nuclear Instruments and Methods in Physics Research Section A: Accelerators, Spectrometers, Detectors and Associated Equipment*, 623(3):1035–1045, 2010.

[51] PM Dighe and D Das. Performance studies of boron lined proportional counters for reactor applications. *Nuclear Instruments and Methods*

in Physics Research Section A: Accelerators, Spectrometers, Detectors and Associated Equipment, 770:29–35, 2015.

[52] José Patrício Náhuel Cárdenas, Tufic Madi Filho, Anna R Petri, Robinson A dos Santos, João FT Martins, Diego VS Carvalho, T Alvarenga, M Bellezzo, G Laranjo, M Lima, et al. Experimental and mcnp studies of paraffin and polyethylene in neutron moderation and bf 3 detector efficiency. In *Advancements in Nuclear Instrumentation Measurement Methods and their Applications (ANIMMA), 2013 3rd International Conference on*, pages 1–5. IEEE, 2013.

[53] Natalia Zaitsev'a, Andrew Glenn, H Paul Martinez, Leslie Carman, Iwona Pawełczak, Michelle Faust, and Stephen Payne. Pulse shape discrimination with lithium-containing organic scintillators. *Nuclear Instruments and Methods in Physics Research Section A: Accelerators, Spectrometers, Detectors and Associated Equipment*, 729:747–754, 2013.

[54] David Emin and TL Aselage. A proposed boron-carbide-based solid-state neutron detector. *Journal of applied physics*, 97(1):013529, 2005.

[55] Kawser Ahmed, Rajendra Dahal, Adam Weltz, James J-Q Lu, Yaron Danon, and Ishwara B Bhat. Solid-state neutron detectors based on thickness scalable hexagonal boron nitride. *Applied Physics Letters*, 110(2):023503, 2017.

[56] E Tupitsyn, P Bhattacharya, E Rowe, L Matei, M Groza, B Wiggins, A Burger, and A Stowe. Single crystal of liinse2 semiconductor for neutron detector. *Applied Physics Letters*, 101(20):202101, 2012.

[57] Alireza Kargar, Joshua Tower, Huicong Hong, Leonard Cirignano, William Higgins, and Kanai Shah. Lithium and boron based semicon-

ductors for thermal neutron counting. In *SPIE Optical Engineering+ Applications*, pages 81421P–81421P. International Society for Optics and Photonics, 2011.

[58] J Kopecky et al. Atlas of neutron capture cross sections. *International Nuclear Data Committee*, 1997.

[59] United States. Department of Energy and DW Jeppson. *Lithium literature review: lithium's properties and interactions.* Department of Energy, 1978.

[60] A Rose. Sputtered boron films on silicon surface barrier detectors. *Nuclear Instruments and Methods*, 52(1):166–170, 1967.

[61] Stanislav Pospisil, Bruno Sopko, Eva Havrankova, Zdenek Janout, Jan Konicek, Ivan Macha, and Jaroslav Pavlu. Si diode as a small detector of slow neutrons. *Radiation Protection Dosimetry*, 46(2):115–118, 1993.

[62] DS McGregor, SM Vernon, HK Gersch, SM Markham, SJ Wojtczuk, and DK Wehe. Self-biased boron-10 coated high-purity epitaxial gaas thermal neutron detectors. *IEEE Transactions on Nuclear Science*, 47(4):1364–1370, 2000.

[63] M Campbell, EHM Heijne, J Kubašta, P Middelkamp, S Pospíšil, P Šícho, W Snoeys, and V Vrba. Silicon pixel devices as a slow neutron precise position detector. *Nuclear Instruments and Methods in Physics Research Section A: Accelerators, Spectrometers, Detectors and Associated Equipment*, 395(3):457–458, 1997.

[64] J Schelten, M Balzhäuser, F Höngesberg, R Engels, and R Reinartz. A new neutron detector development based on silicon semiconductor

and 6lif converter. *Physica B: Condensed Matter*, 234:1084–1086, 1997.

[65] Massimo Barbagallo, Luigi Cosentino, Vittorio Forcina, Carmelo Marchetta, Alfio Pappalardo, Paolo Peerani, Carlotta Scirè, Sergio Scirè, Maria Schillaci, Stefano Vaccaro, et al. Thermal neutron detection using a silicon pad detector and 6lif removable converters. *Review of Scientific Instruments*, 84(3):033503, 2013.

[66] Douglas S McGregor, Raymond T Klann, Jeffrey D Sanders, John T Lindsay, Kurt J Linden, Holly K Gersch, PM De Lurgio, Charles L Fink, and Elsa Ariesanti. Recent results from thin-film-coated semiconductor neutron detectors. In *International Symposium on Optical Science and Technology*, pages 164–182. International Society for Optics and Photonics, 2003.

[67] RA Muminov and LD Tsvang. High-efficiency semiconductor theramal-neutron detectors. *Soviet Atomic Energy*, 62(4):316–319, 1987.

[68] Cédric Paul Allier. *Micromachined Si-well scintillator pixel detectors*. PhD thesis, TU Delft, Delft University of Technology, 2001.

[69] Douglas S McGregor, Raymond T Klann, Holly K Gersch, Elsa Ariesanti, Jeffrey D Sanders, and Brian VanDerElzen. New surface morphology for low stress thin-film-coated thermal neutron detectors. *IEEE Transactions on Nuclear Science*, 49(4):1999–2004, 2002.

[70] J Kenneth Shultis and Douglas S McGregor. Efficiencies of coated and perforated semiconductor neutron detectors. In *Nuclear Science Symposium Conference Record, 2004 IEEE*, volume 7, pages 4569–4574. IEEE, 2004.

[71] J Kenneth Shultis and Douglas S McGregor. Efficiencies of coated and perforated semiconductor neutron detectors. *IEEE TRANSACTIONS ON NUCLEAR SCIENCE*, 53(3):1659, 2006.

[72] CJ Solomon, JK Shultis, WJ McNeil, TC Unruh, BB Rice, and DS McGregor. A hybrid method for coupled neutron–ion transport calculations for 10 b and 6 lif coated and perforated detector efficiencies. *Nuclear Instruments and Methods in Physics Research Section A: Accelerators, Spectrometers, Detectors and Associated Equipment*, 580(1):326–330, 2007.

[73] CJ Solomon, JK Shultis, and DS McGregor. Reduced efficiency variation in perforated neutron detectors with sinusoidal trench design. *Nuclear Instruments and Methods in Physics Research Section A: Accelerators, Spectrometers, Detectors and Associated Equipment*, 618(1):260–265, 2010.

[74] DS McGregor, SL Bellinger, D Bruno, WL Dunn, WJ McNeil, E Patterson, BB Rice, JK Shultis, and T Unruh. Perforated diode neutron detector modules fabricated from high-purity silicon. *Radiation Physics and Chemistry*, 78(10):874–881, 2009.

[75] JK Shultis and DS McGregor. Design and performance considerations for perforated semiconductor thermal-neutron detectors. *Nuclear Instruments and Methods in Physics Research Section A: Accelerators, Spectrometers, Detectors and Associated Equipment*, 606(3):608–636, 2009.

[76] SL Bellinger, WJ McNeil, and DS McGregor. Variant designs and characteristics of improved microstructured solid-state neutron detectors. In *Nuclear Science Symposium Conference Record (NSS/MIC), 2009 IEEE*, pages 986–989. IEEE, 2009.

[77] Walter J McNeil, Steven L Bellinger, Troy C Unruh, Chris M Henderson, Phil Ugorowski, Bryce Morris-Lee, Russell D Taylor, and Douglas S McGregor. 1-d array of perforated diode neutron detectors. *Nuclear Instruments and Methods in Physics Research Section A: Accelerators, Spectrometers, Detectors and Associated Equipment*, 604(1):127–129, 2009.

[78] SL Bellinger, RG Fronk, WJ McNeil, TJ Sobering, and DS McGregor. High efficiency dual-integrated stacked microstructured solid-state neutron detectors. In *Nuclear Science Symposium Conference Record (NSS/MIC), 2010 IEEE*, pages 2008–2012. IEEE, 2010.

[79] SL Bellinger, RG Fronk, WJ McNeil, TJ Sobering, and DS McGregor. Improved high efficiency stacked microstructured neutron detectors backfilled with nanoparticle ^{6} lif. *IEEE Transactions on Nuclear Science*, 59(1):167–173, 2012.

[80] Steven L Bellinger, Ryan G Fronk, Douglas S McGregor, and Timothy J Sobering. Arrayed high efficiency dual-integrated microstructured semiconductor neutron detectors. In *Nuclear Science Symposium and Medical Imaging Conference (NSS/MIC), 2011 IEEE*, pages 1281–1284. IEEE, 2011.

[81] SL Bellinger, RG Fronk, WJ McNeil, TJ Sobering, and DS McGregor. Enhanced variant designs and characteristics of the microstructured solid-state neutron detector. *Nuclear Instruments and Methods in Physics Research Section A: Accelerators, Spectrometers, Detectors and Associated Equipment*, 652(1):387–391, 2011.

[82] Ryan G Fronk, Steven L Bellinger, Luke C Henson, DE Huddleston, TR Ochs, TJ Sobering, and Douglas S McGregor. High-efficiency

microstructured semiconductor neutron detectors for direct 3 he replacement. *Nuclear Instruments and Methods in Physics Research Section A: Accelerators, Spectrometers, Detectors and Associated Equipment*, 779:25–32, 2015.

[83] Taylor R Ochs, Steven L Bellinger, Ryan G Fronk, Luke C Henson, David E Huddleston, Zoairia I Lyric, John Kenneth Shultis, Colten T Smith, Timothy J Sobering, and Douglas S McGregor. Present status of the microstructured semiconductor neutron detector (msnd)-based direct helium-3 replacement (herep). *IEEE Transactions on Nuclear Science*, 2017.

[84] Q Shao, LF Voss, AM Conway, RJ Nikolic, MA Dar, and CL Cheung. High aspect ratio composite structures with 48.5% thermal neutron detection efficiency. *Applied Physics Letters*, 102(6):063505, 2013.

[85] Rebecca J Nikolic, Adam M Conway, Catherine E Reinhardt, Robert T Graff, Tzu Fang Wang, Nirmalendu Deo, and Chin Li Cheung. Fabrication of pillar-structured thermal neutron detectors. In *Nuclear Science Symposium Conference Record, 2007. NSS'07. IEEE*, volume 2, pages 1577–1580. IEEE, 2007.

[86] Rebecca J Nikolic, Adam M Conway, Catherine E Reinhardt, Robert T Graff, Tzu-Fang Wang, Nirmalendu Deo, and Chin Li Cheung. Pillar structured thermal neutron detector. In *Solid-State and Integrated-Circuit Technology, 2008. ICSICT 2008. 9th International Conference on*, pages 2361–2364. IEEE, 2008.

[87] EK Broadbent and CL Ramiller. Selective low pressure chemical vapor deposition of tungsten. *Journal of The Electrochemical Society*, 131(6):1427–1433, 1984.

[88] DP Adams, TM Mayer, and BS Swartzentruber. Selective area growth of metal nanostructures. *Applied physics letters*, 68(16):2210–2212, 1996.

[89] LF Voss, Q Shao, CE Reinhardt, RT Graff, AM Conway, RJ Nikolić, Nirmalendu Deo, and Chin Li Cheung. Planarization of high aspect ratio p-i-n diode pillar arrays for blanket electrical contacts. *Journal of Vacuum Science & Technology B, Nanotechnology and Microelectronics: Materials, Processing, Measurement, and Phenomena*, 28(5):916–920, 2010.

[90] LF Voss, CE Reinhardt, RT Graff, AM Conway, RJ Nikolić, N Deo, and CL Cheung. Etching of 10 boron with sf 6-based electron cyclotron resonance plasmas for pillar-structured thermal neutron detectors. *Journal of electronic materials*, 39(3):263–267, 2010.

[91] Lars F Voss, Cathy E Reinhardt, Robert T Graff, Adam M Conway, Qinghui Shao, Rebecca J Nikolic, Mushtaq A Dar, and Chin L Cheung. Analysis of strain in dielectric coated three dimensional si micropillar arrays. *Journal of Vacuum Science & Technology B, Nanotechnology and Microelectronics: Materials, Processing, Measurement, and Phenomena*, 31(6):060602, 2013.

[92] RJ Nikolić, AM Conway, CE Reinhardt, RT Graff, TF Wang, N Deo, and CL Cheung. 6: 1 aspect ratio silicon pillar based thermal neutron detector filled with b 10. *Applied Physics Letters*, 93(13):133502, 2008.

[93] Qinghui Shao, Adam M Conway, Lars F Voss, Radoslav P Radev, Rebecca J Nikolić, Mushtaq A Dar, and Chin L Cheung. Experimental determination of gamma-ray discrimination in pillar-structured thermal neutron detectors under high gamma-ray flux. *Nuclear Instruments and Methods in Physics Research Section A: Accelerators,*

Spectrometers, Detectors and Associated Equipment, 799:203–206, 2015.

[94] Yaron Danon, Justin Clinton, Kuan-Chih Huang, Nicholas LiCausi, Rajendra Dahal, JJQ Lu, and Ishwara Bhat. Towards high efficiency solid-state thermal and fast neutron detectors. *Journal of Instrumentation*, 7(03):C03014, 2012.

[95] Kuan-Chih Huang, Rajendra Dahal, Nicolas LiCausi, James J-Q Lu, Yaron Danon, and Ishwara B Bhat. Boron filling of high aspect ratio holes by chemical vapor deposition for solid-state neutron detector applications. *Journal of Vacuum Science & Technology B, Nanotechnology and Microelectronics: Materials, Processing, Measurement, and Phenomena*, 30(5):051204, 2012.

[96] Kuan-Chih Huang, Rajendra Dahal, James J-Q Lu, Yaron Danon, and Ishwara B Bhat. High detection efficiency micro-structured solid-state neutron detector with extremely low leakage current fabricated with continuous pn junction. *Applied Physics Letters*, 102(15):152107, 2013.

[97] J Húlka, Z Hrdlickka, Z Janout, S Pospisil, and Z Prouza. Measurement using semiconductor silicon detector with 6 li convertor of thermal neutron flux density distribution in object modelling human body. *Jaderna Energie*, 31(10):376–380, 1985.

[98] J Jakubek, T Holy, E Lehmann, S Pospisil, J Uher, J Vacik, and D Vavrik. Spatial resolution of medipix-2 device as neutron pixel detector. *Nuclear Instruments and Methods in Physics Research Section A: Accelerators, Spectrometers, Detectors and Associated Equipment*, 546(1):164–169, 2005.

[99] Medipix collaboration. http://medipix.web.-cern.ch/MEDIPIX/. [Online; accessed 2017-02-02].

[100] Stanislav Pospisil, Carlos Granja, Carlos Granja, and Claude Leroy. Neutrons and their detection with silicon diodes. *AIP Conference Proceedings*, 1204(1):12–16, 2010.

[101] Josef Uher. 3d neutron detectors. *Dotoral Thesis, Czech Technical University*, 2007.

[102] J Uher, Christer Fröjdh, J Jakubek, C Kenney, Z Kohout, V Linhart, S Parker, Sture Petersson, S Pospíšil, and Göran Thungström. Characterization of 3d thermal neutron semiconductor detectors. *Nuclear Instruments and Methods in Physics Research Section A: Accelerators, Spectrometers, Detectors and Associated Equipment*, 576(1):32–37, 2007.

[103] A Kok, Z Kohout, T-E Hansen, Sture Petersson, S Pospisil, J Rokne, T Slavicek, S Soligard, G Thungstrom, and Z Vykydal. Silicon sensors with pyramidal structures for neutron imaging. *Journal of Instrumentation*, 9(04):C04011, 2014.

[104] S Esteban, C Fleta, C Guardiola, C Jumilla, G Pellegrini, D Quirion, J Rodriguez, and M Lozano. Microstructured silicon neutron detectors for security applications. *Journal of Instrumentation*, 9(12):C12006, 2014.

[105] Sherwood I Parker, Christopher J Kenney, and Julie Segal. 3d—a proposed new architecture for solid-state radiation detectors. *Nuclear Instruments and Methods in Physics Research Section A: Accelerators, Spectrometers, Detectors and Associated Equipment*, 395(3):328–343, 1997.

[106] Hassina Z Bilheux, Jean-Ch Bilheux, W Barton Bailey, W Scott Keener, Larry E Davis, Ken W Herwig, and Maria Cekanova. Neutron imaging at the oak ridge national laboratory: Application to biological research. In *Biomedical Science and Engineering Center Conference (BSEC), 2014 Annual Oak Ridge National Laboratory*, pages 1–4. IEEE, 2014.

[107] Axel Griesche, Eitan Dabah, Thomas Kannengiesser, Nikolay Kardjilov, André Hilger, and Ingo Manke. Three-dimensional imaging of hydrogen blister in iron with neutron tomography. *Acta Materialia*, 78:14–22, 2014.

[108] Thomas Watkins, Hassina Bilheux, Ke An, Andrew Payzant, Ryan Dehoff, Chad Duty, William Peter, Craig Blue, and Craig A Brice. Neutron characterization for additive manufacturing. 2013.

[109] Claudio Piemonte, Maurizio Boscardin, Gian-Franco Dalla Betta, Sabina Ronchin, and Nicola Zorzi. Development of 3d detectors featuring columnar electrodes of the same doping type. *Nuclear Instruments and Methods in Physics Research Section A: Accelerators, Spectrometers, Detectors and Associated Equipment*, 541(1):441–448, 2005.

[110] Ulisse Bravar, Paul J Bruillard, Erwin O Flckiger, John R Macri, Mark L McConnell, Michael R Moser, James M Ryan, and Richard S Woolf. Design and testing of a position-sensitive plastic scintillator detector for fast neutron imaging. *IEEE transactions on nuclear science*, 53(6):3894–3903, 2006.

[111] A Quaranta, S Carturan, T Marchi, M Cinausero, C Scian, VL Kravchuk, M Degerlier, F Gramegna, M Poggi, and G Mag-

gioni. Doping of polysiloxane rubbers for the production of organic scintillators. *Optical Materials*, 32(10):1317–1320, 2010.

[112] Alberto Quaranta, Sara Maria Carturan, Tommaso Marchi, Vladimir L Kravchuk, Fabiana Gramegna, Gianluigi Maggioni, and Meltem Degerlier. Optical and scintillation properties of polydimethyldiphenylsiloxane based organic scintillators. *IEEE Transactions on Nuclear Science*, 57(2):891–900, 2010.

[113] Matteo Dalla Palma. *Polysiloxane based neutron detectors*. PhD thesis, University of Trento, 2016.

[114] A Quaranta, S Carturan, M Cinausero, Tommaso Marchi, F Gramegna, M Degerlier, A Cemmi, and S Baccaro. Characterization of polysiloxane organic scintillators produced with different phenyl containing blends. *Materials Chemistry and Physics*, 137(3):951–958, 2013.

[115] Margaret Bowen, Stan Majewski, David Pettey, James Walker, Randolph Wojcik, and Carl Zorn. A new radiation-resistant plastic scintillator. *IEEE Transactions on Nuclear Science*, 36(1):562–566, 1989.

[116] G Verzellesi, GF Dalla Betta, L Bosisio, M Boscardin, GU Pignatel, and G Soncini. On the accuracy of generation lifetime measurement in high-resistivity silicon using pn gated diodes. *IEEE Transactions on Electron Devices*, 46(4):817–820, 1999.

[117] R Hezel and K Jaeger. Low-temperature surface passivation of silicon for solar cells. *Journal of the Electrochemical Society*, 136(2):518–523, 1989.

[118] G Agostinelli, A Delabie, P Vitanov, Z Alexieva, HFW Dekkers, S De Wolf, and G Beaucarne. Very low surface recombination velocities on p-type silicon wafers passivated with a dielectric with fixed negative charge. *Solar Energy Materials and Solar Cells*, 90(18):3438–3443, 2006.

[119] V Fadeyev, HF-W Sadrozinski, S Ely, JG Wright, M Christophersen, BF Phlips, G Pellegrini, S Grinstein, G-F Dalla Betta, M Boscardin, et al. Scribe–cleave–passivate (scp) slim edge technology for silicon sensors. *Nuclear Instruments and Methods in Physics Research Section A: Accelerators, Spectrometers, Detectors and Associated Equipment*, 731:260–265, 2013.

[120] Yigang Yang, Chenguang Li, Cai Chen, Xuewu Wang, and Yuanjing Li. Research of boron lined honey-neutron detector realized with atomic layer deposition. In *Nuclear Science Symposium and Medical Imaging Conference (NSS/MIC), 2013 IEEE*, pages 1–3. IEEE, 2013.

[121] TCAD Synopsys. software tools online documentation, access at the address: http://www. synopsys. com/tools.

[122] Sea Agostinelli, John Allison, K al Amako, J Apostolakis, H Araujo, P Arce, M Asai, D Axen, S Banerjee, G Barrand, et al. Geant4—a simulation toolkit. *Nuclear instruments and methods in physics research section A: Accelerators, Spectrometers, Detectors and Associated Equipment*, 506(3):250–303, 2003.

[123] John Allison, K Amako, J e a1 Apostolakis, HAAH Araujo, P Arce Dubois, MAAM Asai, GABG Barrand, RACR Capra, SACS Chauvie, RACR Chytracek, et al. Geant4 developments and applications. *IEEE Transactions on Nuclear Science*, 53(1):270–278, 2006.

[124] Christopher M Poole, Iwan Cornelius, Jamie V Trapp, and Christian M Langton. A cad interface for geant4. *Australasian physical & engineering sciences in medicine*, 35(3):329–334, 2012.

[125] Billy W Loo, Fred S Goulding, and Dexi Gao. Ballistic deficits in pulse shaping amplifiers. *IEEE Transactions on Nuclear Science*, 35(1):114–118, 1988.

[126] Lucio Pancheri and David Stoppa. A low-cost picosecond laser module for time-resolved optical sensing applications. *IEEE Sensors Journal*, 11(6):1380–1381, 2011.

[127] Andrea Zoboli, Maurizio Boscardin, Luciano Bosisio, Gian-Franco Dalla Betta, Claudio Piemonte, Alberto Pozza, Sabina Ronchin, and Nicola Zorzi. Electro-optical measurements of 3d-stc detectors fabricated at itc-irst. *Nuclear Instruments and Methods in Physics Research Section A: Accelerators, Spectrometers, Detectors and Associated Equipment*, 583(1):149–152, 2007.

[128] Josef Kemmer. Fabrication of low noise silicon radiation detectors by the planar process. *Nuclear Instruments and Methods*, 169(3):499–502, 1980.

[129] P Yang, G Aglieri, C Cavicchioli, PL Chalmet, N Chanlek, A Collu, C Gao, H Hillemanns, G Huang, A Junique, et al. Maps development for the alice its upgrade. *Journal of Instrumentation*, 10(03):C03030, 2015.

[130] Fabiola Gianotti, Michelangelo L Mangano, T Virdee, S Abdullin, G Azuelos, A Ball, D Barberis, A Belyaev, P Bloch, M Bosman, et al. Physics potential and experimental challenges of the lhc luminosity upgrade. *The European Physical Journal C-Particles and Fields*, 39(3):293–333, 2005.

[131] N Venturi. Diamond pixel detectors and 3d diamond devices. *Journal of Instrumentation*, 11(12):C12062, 2016.

[132] C DaVia and SJ Watts. The geometrical dependence of radiation hardness in planar and 3d silicon detectors. *Nuclear Instruments and Methods in Physics Research Section A: Accelerators, Spectrometers, Detectors and Associated Equipment*, 603(3):319–324, 2009.

[133] Sabina Ronchin, Maurizio Boscardin, Claudio Piemonte, Alberto Pozza, Nicola Zorzi, Gian-Franco Dalla Betta, Luciano Bosisio, and Giulio Pellegrini. Fabrication of 3d detectors with columnar electrodes of the same doping type. *Nuclear Instruments and Methods in Physics Research Section A: Accelerators, Spectrometers, Detectors and Associated Equipment*, 573(1):224–227, 2007.

[134] S Eranen, T Virolainen, I Luusua, J Kalliopuska, K Kurvinen, M Eraluoto, J Harkonen, K Leinonen, M Palviainen, and M Koski. Silicon semi 3d radiation detectors. In *Nuclear Science Symposium Conference Record, 2004 IEEE*, volume 2, pages 1231–1235. IEEE, 2004.

[135] Tanja Grönlund, Zheng Li, Gabriella Carini, and Michael Li. Full 3d simulations of bnl one-sided silicon 3d detectors and comparisons with other types of 3d detectors. *Nuclear Instruments and Methods in Physics Research Section A: Accelerators, Spectrometers, Detectors and Associated Equipment*, 586(2):180–189, 2008.

[136] Andrea Zoboli, Maurizio Boscardin, Luciano Bosisio, Gian-Franco Dalla Betta, Simon Eckert, Susanne Kuhn, Claudio Piemonte, Ulrich Parzefall, Sabina Ronchin, and Nicola Zorzi. Functional characterization of 3d-ddtc detectors fabricated at fbk-irst. In *Nuclear Science Symposium Conference Record, 2008. NSS'08. IEEE*, pages 2721–2726. IEEE, 2008.

[137] Andrea Zoboli, Maurizio Boscardin, Luciano Bosisio, Gian-Franco Dalla Betta, Claudio Piemonte, Sabina Ronchin, and Nicola Zorzi. Double-sided, double-type-column 3-d detectors: Design, fabrication, and technology evaluation. *IEEE Transactions on Nuclear Science*, 55(5):2775–2784, 2008.

[138] G Pellegrini, M Lozano, M Ullan, R Bates, C Fleta, and D Pennicard. First double-sided 3-d detectors fabricated at cnm-imb. *Nuclear Instruments and Methods in Physics Research Section A: Accelerators, Spectrometers, Detectors and Associated Equipment*, 592(1):38–43, 2008.

[139] Elisa Vianello, Alvise Bagolini, Pierluigi Bellutti, Maurizio Boscardin, Gian-Franco Dalla Betta, Gabriele Giacomini, Claudio Piemonte, Marco Povoli, and Nicola Zorzi. Optimization of double-side 3d detector technology for first productions at fbk. In *Nuclear Science Symposium and Medical Imaging Conference (NSS/MIC), 2011 IEEE*, pages 523–528. IEEE, 2011.

[140] Gian-Franco Dalla Betta, Alvise Bagolini, Maurizio Boscardin, Luciano Bosisio, Paolo Gabos, Gabriele Giacomini, Claudio Piemonte, Marco Povoli, Elisa Vianello, and Nicola Zorzi. Development of modified 3d detectors at fbk. In *Nuclear Science Symposium Conference Record (NSS/MIC), 2010 IEEE*, pages 382–387. IEEE, 2010.

[141] G-F Dalla Betta, N Ayllon, M Boscardin, M Hoeferkamp, S Mattiazzo, H McDuff, R Mendicino, M Povoli, S Seidel, DMS Sultan, et al. Investigation of leakage current and breakdown voltage in irradiated double-sided 3d silicon sensors. *Journal of Instrumentation*, 11(09):P09006, 2016.

[142] D Pennicard, G Pellegrini, C Fleta, R Bates, V O'Shea, C Parkes,

and N Tartoni. Simulations of radiation-damaged 3d detectors for the super-lhc. *Nuclear Instruments and Methods in Physics Research Section A: Accelerators, Spectrometers, Detectors and Associated Equipment*, 592(1):16–25, 2008.

[143] M Povoli, A Bagolini, M Boscardin, G-F Dalla Betta, G Giacomini, E Vianello, and N Zorzi. Slim edges in double-sided silicon 3d detectors. *Journal of Instrumentation*, 7(01):C01015, 2012.

[144] Triga mark ii reactor. `www.rcp.ijs.si/ric/description-a.html`. [Online; accessed 2017-02-02].

[145] M Petasecca, F Moscatelli, D Passeri, and GU Pignatel. Numerical simulation of radiation damage effects in p-type and n-type fz silicon detectors. *IEEE transactions on nuclear science*, 53(5):2971–2976, 2006.

[146] G Kramberger, V Cindro, I Mandić, M Mikuž, and M Zavrtanik. Effective trapping time of electrons and holes in different silicon materials irradiated with neutrons, protons and pions. *Nuclear Instruments and Methods in Physics Research Section A: Accelerators, Spectrometers, Detectors and Associated Equipment*, 481(1):297–305, 2002.